UNIVERSITY OF CALIFORNIA

Los Angeles

Multi-scale vegetation-aeolian transport interaction in drylands: remote sensing and modeling

A dissertation submitted in partial satisfaction of the requirement for the degree Doctor of

Philosophy in Geography

by

Junzhe Zhang

2019

ABSTRACT OF THE DISSERTATION

Multi-scale vegetation-aeolian transport interaction in drylands: remote sensing and modeling

by

Junzhe Zhang

Doctor of Philosophy in Geography

University of California, Los Angeles, 2019

Professor Gregory Okin, Chair

Vegetation-aeolian transport interaction strongly affects ecosystem function, landform, and dust emission in drylands. Vegetation strongly modulates the pattern of wind-driven transport in drylands; however, the interaction between vegetation and aeolian transport is complex and vary across the different spatial scales. Moreover, this interaction also results in the strengthening of soil erosions and the loss of nutrients by blowing and flushing away soil particles, which have been recognized as the primary components of desertification. Recent studies indicate that climate change has been taking place and is predicted to become more common in arid and semiarid regions, amplifying aeolian processes and changing vegetation pattern. Therefore, measurement, monitoring, and assessment of vegetation-aeolian transport interaction became important. Previous studies have only focused on the interaction at a single spatial scale. The overall goal of

my dissertation is to provide a comprehensive investigation of the vegetation-aeolian transport interaction from a multi-scale perspective.

In this study, a drone-based remote sensing method was created to characterize biophysical indicators in a grass-shrub ecosystem at a landscape scale. This drone-based remote sensing method was proved to be an efficient, high accuracy, and low-cost method that serves as an alternative to field measurements to provide tempo-spatial continuous observation of vegetation pattern and landform change. A machine learn-based data assimilation method was developed to predict the biophysical indicators in the arid and semiarid rangelands of Western U.S. This machine learning-based data assimilation method was applied on the arid and semiarid rangelands of Western U.S. to build the first-ever distribution maps of several biophysical indicators. Based on the prediction of these biophysical indicators, a semi-physical model was designed to estimate the vertical dust flux in the Western U.S. and the results were validated by satellite remote sensing product. Last, an ecological model was developed to simulate the impact of aeolian transport on vegetation pattern and landform at a landscape scale. This model successfully imitated the impact of aeolian transport on vegetation community. The study of this dissertation improved the understanding of vegetation-aeolian transport interaction.

This dissertation of Junzhe Zhang is approved.

YONGKANG XUE

THOMAS WELCH GILLESPIE

JASPER F. KOK

GREGORY STEWART OKIN, Committee Chair

University of California, Los Angeles

2019

Dedications

To my dear family . . .

for the endless love and support

Table of Contents

List of Figures

Chapter 1

Chapter 3

Chapter 4

List of Tables

Chapter 1

Chapter 2

Acknowledgments

Earning a Ph.D. is very hard and not an individual achievement. First, I am deeply grateful for my parents, for believing in me and supporting me physically and mentally. Second, I have to thank my girlfriend, supporting me through the ups and downs of completing my dissertation and many other things. Third, I have a great appreciation for Prof. Okin's patience and dedication to being my adviser.

I would like to dedicate this to all my committee members: Yongkang Xue, Thomas Gillespie, and Jasper Kok. I want to thank many people: Jason Karl, Debra P.C. Peters, Haitao Huang, Abinash Bhattachan, Chunyu Dong, Huilin Huang, Ye Liu, Matt Zebrowski, and Bo Zhou.

<p style="text-align: center;">**Curriculum Vitae**</p>

Education

University of California, Los Angeles	Los Angeles, USA
Master of Science, Atmospheric Science	December 2015
Beijing Normal University	Beijing, China
Master of Science, Geographic Information System and Cartography	June 2013
Beijing Normal University	Beijing, China
Bachelor of Engineering, Physics (Optical and Electrical Engineering)	June 2010

Honors & Awards

UCLA Dissertation Year Fellowship ($35,000)	2018
Jornada Basin LTER Graduate Research Fellowship ($24,000)	2017
Jornada Basin LTER Graduate Research Fellowship ($22,000)	2016
Chinese National Scholarship for Graduate Student ($5,000)	2012
Beijing Normal University Outstanding Graduate Student ($3,000)	2012

Publications

Okin, Gregory; Sala, Osvaldo; Vivoni, Enrique; and **Zhang, Junzhe**. "The interactive role of wind and water in dryland function: what does the future hold?". BioScience (2018).

Zhang, Junzhe; et al. "A spectral similarity measure cased on Changing-Weight Combination Method". *Acta Geodaetica et Cartographica Sinica* 42.3 (2013).

Zhang, Junzhe; et al. "Comparative study on similarity measure of hyperspectral remote sensing data". *Science of Surveying and Mapping* 38.6 (2013).

Liu, Jianhong; Zhu, Wenquan; **Zhang, Junzhe**; and Jiang, Nan. "Endmember abundance calibration method for paddy rice area extraction from MODIS data based on independent component analysis". *Transactions of the Chinese Society of Agricultural Engineering* 28.9 (2012).

Du, Hongyue; **Zhang, Junzhe**; and Gong, Huili. "Research of DEM quality-precision analysis and system implementation". *Science of Surveying and Mapping*. 34.5 (2009).

Zhang, Junzhe; et al. "Quantifying vegetation structure and distribution in drylands using high resolution drone-based structure from motion photogrammetry". *Ecosphere*. (in review)

Zhang, Junzhe; et al. "Assimilating satellite remote sensing images and field data to predict vegetation indicators of arid and semiarid rangeland in the Western U.S.". *Remote Sensing of Environment*. (in review)

Bhattachan, Abinash; **Zhang, Junzhe**; and Okin, Gregory. "Evaluation of the different multiple endmember spectral mixture analyses using MODIS in the arid rangeland of Australia for retrieval of green vegetation, nonphotosynthetic vegetation, and soil fractional cover". *Remote Sensing of Environment.* (in review)

Bhattachan, Abinash; **Zhang, Junzhe**; Okin, Gregory; and Lettenmaier, Dennis. "An evaluation of the impact of dust storms on the local traffic accidents in California". *Geophysical Research Letters.* (in review)

Nadoum, Shereen; Okin, Gregory; and **Zhang, Junzhe**. "Leveraging satellite remote sensing to estimate the net primary production by using multiple endmember spectral mixture analysis in arid and semiarid rangeland". *Ecosphere.* (in review)

Presentations

Oral Presentation
2018 American Association of Geographers (AAG) Annual Meeting   New Orleans, U.S.
"Evaluation of multiple endmember spectral mixture analysis in Qinghai Lake Basin"
2012 IEEE Geoscience and Remote Sensing Society Symposium   Munich, Germany
(IGARSS)
"A phenology-preserving filtering method to reduce noise in NDVI time series"
Poster Presentation
2018 American Geophysical Union (AGU) Annual Meeting   D.C., U.S.
"Integrating ecotone and wemo models to simulate the evolution of vegetation pattern impacted by sediment movement"
2017 American Geophysical Union (AGU) Annual Meeting   New Orleans, U.S.
"Quantifying vegetation structure in drylands using drone-based structure-from-motion photogrammetry"
2016 American Geophysical Union (AGU) Annual Meeting   San Francisco, U.S.
"Integrating satellite remote sensing and field data to predict rangeland structural indicators"
2012 IEEE Geoscience and Remote Sensing Society Symposium   Munich, Germany
(IGARSS)
"Evaluation of similarity measure methods for hyperspectral remote sensing data"

Reviewer

Aeolian Research   2017-2018

Science of the Total Environment   2017-2018

Ecological Engineering   2018-2019

Environmental Earth Sciences   2018-2019

Introduction

Drylands cover above 40% of the Earth's surface and are habitat to over two billion people (MEA 2005). Land degradation in these regions is clearly occurring and becomes one of the severest environmental crises of the 21st century since it significantly influences food safety and environmental quality (Bestelmeyer et al. 2015; Reynolds et al. 2007). Moreover, soil degradation and vegetation reduction cause considerable decreases in ecosystem services and functions (Hutchinson 1996; Thomas 1997; Veron et al. 2006). Recent studies indicate that climate change has been taking place and is predicted to become more common in arid and semiarid regions, amplifying aeolian transport and changing vegetation pattern (Burke et al. 2006; Held et al. 2005; Seager et al. 2007). Although the role of aeolian transport in accelerating desertification is well recognized (Nicholson et al. 1998; Okin et al. 2009; Schlesinger et al. 1990; Van Auken 2000), the understanding of how the interaction between aeolian transport and vegetation contributes to desertification is still uncertain.

Vegetation-aeolian transport interaction strongly affects ecosystem function, landform, and dust emission in drylands (Okin et al. 2006). Vegetation strongly modulates patterns of wind-driven transport in drylands; however, the interaction between vegetation and aeolian transport is complex and vary across the different spatial scales (Alvarez et al. 2011; Ravi et al. 2010; Shao et al. 2015). Previous studies have only focused on the interaction at a single spatial scale (D'Odorico et al. 2007; Prospero et al. 2002; Ravi et al. 2006; Tegen et al. 2004). The overall goal of my dissertation

is to provide a comprehensive investigation of the vegetation-aeolian transport interaction from a multi-scale perspective.

Research regarding the interaction between vegetation and aeolian transport have traditionally relied on the key biophysical indicators (Baddock et al. 2011; Johnson and Osborne 2011), such as plant height, gap length, and vegetation cover, from field observation, which is often laborious, time-consuming, and susceptible to under-sampling in both space and time (Pellant et al. 1999; West 1999). Moreover, based on the field data, the study of vegetation-aeolian transport interaction cannot be conducted at a continental scale. In order to solve these two problems, the first two chapters of my dissertation introduce that a drone-based remote sensing method has been developed to obtain the key biophysical indicators at the landscape scale and a machine learning algorithm (random forest regression) has been created to assimilate field data and satellite remote sensing data to predict spatial distributions of those biophysical indicators at a continental scale. The estimates of biophysical variables obtained by the drone-based remote sensing method show excellent agreements with *in situ* measurements, indicating that it can serve as a good alternative to field data collection at a landscape scale. The machine learning-based data assimilation method estimates exhibited good correlations with the independent field samples, therefore, the utility of this method is clearly a means to estimate multiple biophysical indicators based on remotely sensed data and predict the distribution of those indicators at a continental scale.

Dust emission reflects the condition of aeolian transport at a certain location for a certain time period. Several studies have been proposed to model horizontal dust flux at a landscape scale (Gillette and Pitchford 2004; Kok 2011; Shao 2001). At a continental scale, although remotely sensed data was used to retrieve the atmospheric dust content (Ginoux et al. 2012; Sayer et al.

2014), the study of developing a physical model to estimate dust emission near surface is less well established. In this study, a new semi-physical model was created to estimate vertical dust flux at a continental scale. This model contains two parts: 1. A machine learning based data assimilation method to spatially predict erodible land surface based on remote sensing data at a continental scale, 2. A process-based physical wind erosion model, which considers vegetation as the non-erodible factor at the land surface, to estimate the vertical dust flux. The vertical dust flux estimate based on the new model exhibited temporally and spatially good correlations with dust optical depth (DOD) derived from Moderate Resolution Imaging Spectroradiometer (MODIS) Deep Blue product.

Although some geomorphic and ecological models have been made to study how vegetation pattern impacts the horizontal dust flux and how aeolian transport influences the landform at a landscape scale (Mayaud et al. 2017; Stewart et al. 2014), few studies have been proposed to model the impact of aeolian transport on vegetation change. A new ecological model (ECO-WEMO) that contains an aeolian transport component was created to simulate how aeolian transport impacts vegetation pattern and causes the state change. The results of model simulation confirm the important role that aeolian transport can play in state change in deserts.

References

Alvarez, L.J., Epstein, H.E., Li, J., & Okin, G.S. (2011). Spatial patterns of grasses and shrubs in an arid grassland environment. *Ecosphere, 2*, 589

Baddock, M.C., Gill, T.E., Bullard, J.E., Acosta, M.D., & Rivera Rivera, N.I. (2011). Geomorphology of the Chihuahuan Desert based on potential dust emissions. *Journal of Maps, 7*, 249-259

Bestelmeyer, B.T., Okin, G.S., Duniway, M.C., Archer, S.R., Sayre, N.F., Williamson, J.C., & Herrick, J.E. (2015). Desertification, land use, and the transformation of global drylands. *Frontiers in Ecology and the Environment, 13*, 28-36

Burke, E.J., Brown, S.J., & Christidis, N. (2006). Modeling the recent evolution of global drought and projections for the twenty-first century with the hadley centre climate model. *Journal of Hydrometeorology, 7*, 1113-1125

D'Odorico, P., Caylor, K., Okin, G.S., & Scanlon, T.M. (2007). On soil moisture–vegetation feedbacks and their possible effects on the dynamics of dryland ecosystems. *Journal of Geophysical Research: Biogeosciences, 112*

Gillette, D.A., & Pitchford, A.M. (2004). Sand flux in the northern Chihuahuan Desert, New Mexico, USA, and the influence of mesquite-dominated landscapes. *Journal of Geophysical Research: Earth Surface, 109*

Ginoux, P., Prospero, J.M., Gill, T.E., Hsu, N.C., & Zhao, M. (2012). Global-Scale Attribution of Anthropogenic and Natural Dust Sources and Their Emission Rates Based on Modis Deep Blue Aerosol Products. *Reviews of Geophysics, 50*

Held, I.M., Delworth, T.L., Lu, J., Findell, K.L., & Knutson, T.R. (2005). Simulation of Sahel drought in the 20th and 21st centuries. *Proceedings of the National Academy of Sciences of the*

United States of America, 102, 17891-17896

Hutchinson, C.F. (1996). The Sahelian desertification debate: A view from the American south-west. *Journal of Arid Environments, 33*, 519-524

Johnson, B.T., & Osborne, S.R. (2011). Physical and optical properties of mineral dust aerosol measured by aircraft during the GERBILS campaign. *Quarterly Journal of the Royal Meteorological Society, 137*, 1117-1130

Kok, J.F. (2011). A scaling theory for the size distribution of emitted dust aerosols suggests climate models underestimate the size of the global dust cycle. *Proceedings of the National Academy of Sciences of the United States of America, 108*, 1016-1021

Mayaud, J.R., Bailey, R.M., & Wiggs, G.F. (2017). A coupled vegetation/sediment transport model for dryland environments. *Journal of Geophysical Research: Earth Surface, 122*, 875-900

MEA (2005). *Ecosystems and human well-being: desertification synthesis*. World Resources Institute

Nicholson, S.E., Tucker, C.J., & Ba, M.B. (1998). Desertification, drought, and surface vegetation: An example from the West African Sahel. *Bulletin of the American Meteorological Society, 79*, 815-829

Okin, G.S., D'Odorico, P., & Archer, S.R. (2009). Impact of feedbacks on Chihuahuan desert grasslands: Transience and metastability. *Journal of Geophysical Research-Biogeosciences, 114*

Okin, G.S., Gillette, D.A., & Herrick, J.E. (2006). Multi-scale controls on and consequences of aeolian processes in landscape change in arid and semi-arid environments. *Journal of Arid Environments, 65*, 253-275

Pellant, M., Shaver, P., & Spaeth, K. (1999). Field test of a prototype rangeland inventory procedure in the western USA. In, *Proceedings of the VI International Rangeland Congress,*

People and Rangelands, Building the Future (pp. 766-767)

Prospero, J.M., Ginoux, P., Torres, O., Nicholson, S.E., & Gill, T.E. (2002). Environmental characterization of global sources of atmospheric soil dust identified with the Nimbus 7 Total Ozone Mapping Spectrometer (TOMS) absorbing aerosol product. *Reviews of Geophysics, 40*, 56

Ravi, S., Breshears, D.D., Huxman, T.E., & D'Odorico, P. (2010). Land degradation in drylands: Interactions among hydrologic-aeolian erosion and vegetation dynamics. *Geomorphology, 116*, 236-245

Ravi, S., Zobeck, T.M., Over, T.M., Okin, G.S., & D'Odorico, P. (2006). On the effect of moisture bonding forces in air-dry soils on threshold friction velocity of wind erosion. *Sedimentology, 53*, 597-609

Reynolds, J.F., Stafford Smith, D.M., Lambin, E.F., Turner, B.L., Mortimore, M., Batterbury, S.P.J., Downing, T.E., Dowlatabadi, H., Fernandez, R.J., Herrick, J.E., Huber-Sannwald, E., Jiang, H., Leemans, R., Lynam, T., Maestre, F.T., Ayarza, M., & Walker, B. (2007). Global desertification: Building a science for dryland development. *Science, 316*, 847-851

Sayer, A., Munchak, L., Hsu, N., Levy, R., Bettenhausen, C., & Jeong, M.J. (2014). MODIS Collection 6 aerosol products: Comparison between Aqua's e-Deep Blue, Dark Target, and "merged" data sets, and usage recommendations. *Journal of Geophysical Research: Atmospheres, 119*, 13,965-913,989

Schlesinger, W.H., Reynolds, J.F., Cunningham, G.L., Huenneke, L.F., Jarrell, W.M., Virginia, R.A., & Whitford, W.G. (1990). Biological Feedbacks in Global Desertification. *Science, 247*, 1043-1048

Seager, R., Ting, M.F., Held, I., Kushnir, Y., Lu, J., Vecchi, G., Huang, H.P., Harnik, N.,

Leetmaa, A., Lau, N.C., Li, C.H., Velez, J., & Naik, N. (2007). Model projections of an imminent transition to a more arid climate in southwestern North America. *Science, 316*, 1181-1184

Shao, Y. (2001). A model for mineral dust emission. *Journal of Geophysical Research-Atmospheres, 106*, 20239-20254

Shao, Y.P., Nickling, W., Bergametti, G., Butler, H., Chappell, A., Findlater, P., Gillies, J., Ishizuka, M., Klose, M., Kok, J.F., Leys, J., Lu, H., Marticorena, B., McTainsh, G., McKenna-Neuman, C., Okin, G.S., Strong, C., & Webb, N. (2015). A tribute to Michael R. Raupach for contributions to aeolian fluid dynamics. *Aeolian Research, 19*, 37-54

Stewart, J., Parsons, A.J., Wainwright, J., Okin, G.S., Bestelmeyer, B.T., Fredrickson, E.L., & Schlesinger, W.H. (2014). Modeling emergent patterns of dynamic desert ecosystems. *Ecological Monographs, 84*, 373-410

Tegen, I., Werner, M., Harrison, S.P., & Kohfeld, K.E. (2004). Relative importance of climate and land use in determining present and future global soil dust emission. *Geophysical Research Letters, 31*

Thomas, D.S.G. (1997). Science and the desertification debate. *Journal of Arid Environments, 37*, 599-608

Van Auken, O.W. (2000). Shrub invasions of North American semiarid grasslands. *Annual Review of Ecology and Systematics, 31*, 197-215

Veron, S.R., Paruelo, J.M., & Oesterheld, M. (2006). Assessing desertification. *Journal of Arid Environments, 66*, 751-763

West, N. (1999). Accounting for rangeland resources over entire landscapes. In, *Proceedings of the VI International Rangeland Congress. Aitkenvale, Queensland* (pp. 726-736)

Chapter 1 Quantifying structural rangeland indicators from drone-based remote sensing image: testing and applications

Abstract: Rangeland indicators such as bare soil gap size and plant height are some of the most important driving factors of ecosystem services and functions in drylands. In this study, a drone-based remote sensing method was developed to characterize rangeland indicators in a grass-shrub ecosystem based on transect lines using structure from motion (SfM) photogrammetry and validated against field measurements. The ability of the drone-based reconstructions to retrieve six rangeland indicators (canopy size, bare soil gap size, plant height, scaled height, vegetation cover, and bare soil cover) were investigated. The drone-based estimates indicated strong agreements with *in situ* measurements in cases where deciduous vegetation (mesquite) had leaves. Performance during leaf-off periods was degraded for mesquite. Based on these results, we find that drone-based remote sensing proved to be an efficient, high accuracy, and low-cost method that serves as an alternative to field measurements for certain rangeland indicators. Upon verification that field-based and drone-based methods agree, we provide examples of how raster imagery from drone-based remote sensing can be used in ways that have distinct advantages over traditional transect measurements. Three advantages identified for verified raster products include 1) the possibility of studies with massive sample size, 2) the possibility of testing for assumptions of stationarity, and 3) the possibility for detection of spatial phenomena, such as anisotropy.

1 Introduction

Drylands cover more than 40% of the Earth's surface and provide habitat for over two billion people (MEA 2005). The functioning of drylands, and therefore the ecosystem services they

provide, depend upon the spatial distribution of plants and soil (Burke et al. 2006; Held et al. 2005; Seager et al. 2008). Discontinuous vegetation, for instance, controls the distribution of solar energy and rain infiltration that impacts the spatial variation of moisture and sensible heat in ecosystems (Albertson et al. 2001; D'Odorico et al. 2007). Likewise, vegetation structure influences both airflow and boundary layer resistance above the land surface (Brokaw and Lent 1999; Okin 2008). Structural elements also impact wind erosion, water erosion, and wildfire. For example, the invasion of shrubs into perennial grasslands results in an increase in the continuity of bare soil (bare soil gaps), which leads to a higher probability of soil loss caused by wind and water erosion; the invasion of exotic grasses into desert shrubland results in a decrease in the continuity of bare soil gaps, which leads to more frequent wildfires (D'Antonio and Vitousek 1992; D'Antonio 2000; Okin et al. 2009). Recent studies have indicated that the occurrence of drought is increasing and is predicted to become more common in arid and semiarid regions, amplifying the need for of rangeland indicators that can indicate declines in ecosystem services and functioning (Hutchinson 1996; Thomas 1997; Wessels et al. 2004).

In situ observations utilize different methods to measure rangeland condition, but these methods are laborious, time-consuming, and susceptible to under-sampling in both space and time (Pellant et al. 1999; West 1999). Multispectral remote sensing has been widely used to monitor vegetation cover and its change (White et al. 2009). For example, Landsat has been applied to extract the densities and patterns of the plant (Franklin and Strahler 1988; Strahler et al. 1999); however, it cannot detect some structural components, such as bare soil gap size and plant height (Liang et al. 2012). Light detection and ranging (LiDAR) is a technique that is commonly used to monitor rangeland condition (Rango et al. 2000; Vierling et al. 2008); however, the cost can be prohibitive.

RADAR (RAdio Detection And Ranging) may also be used to measure some structural and surface components in forests (Israelsson et al. 2000); however, the sparse canopy and low-density vegetation cover of drylands limit the capability of RADAR in arid and semiarid regions (Henderson and Lewis 2008).

In contrast, structural measurements from drone-based photography may provide rapid, inexpensive, and accurate methods for measuring the structure and cover components of dryland systems. For example, drylands are often sparsely covered by short-stature plants, allowing a drone to fly at low heights to obtain ultra-high-resolution orthomosaics (i.e., mm-scale). Moreover, the potentially rapid change in surface and structural indicators due to wildfire or high rainfall, for example, and the ability of drone operators to respond to such rapid changes may make the use of drone-based remote sensing transformative in understanding a variety of rapid ecological processes in drylands.

Structure from motion (SfM) is a photogrammetric technique that builds three-dimensional (3D) models from sequences of two-dimensional (2D) images (Koenderink and Van Doorn 1991). Drone-derived images, together with SfM, can provide both structural and surface information about ecosystems (Turner et al. 2012). The simplicity of drone operation can allow a single investigator to image a relatively large area, with the main limitation being battery power. A drone can be a low-cost mapping tool: a commonly used consumer drone that includes a high-quality camera often costs less than $1,500.

Several studies have employed drone-based remote sensing or aerial photography to survey rangeland indicators based on transect line at a landscape scale (Duniway et al. 2012; Gillan et al. 2016; Gillan et al. 2014; Karl et al. 2012; Karl et al. 2014), but few studies have focused on measuring rangeland indicators on continuous raster imagery, rather than transect line. In this study, drone-based remote sensing was conducted in a well-characterized site in the Jornada Basin, New Mexico during the spring and summer of 2017. For this study, six critical rangeland indicators were chosen (canopy size, bare soil gap size, plant height, scaled height, vegetation cover, and bare soil cover) that are related to some of the most important dryland processes, such as wind erosion (e.g., Okin et al, 2008.), water erosion (e.g., Mueller et al, 2007), fire (e.g., D'Antonio and Vitousek, 1992), and wildlife habitat dynamics (e.g., Laudré et al. 2014). These indicators were measured both *in situ* and from SfM products (i.e., orthomosaics and digital surface models, DSMs) to ensure that the SfM products could reproduce values observed in the field. Four indicators (vegetation cover, bare soil cover, canopy size, and bare soil gap size) were then remeasured on the continuous raster imagery, with the objective of determining whether time-consuming and undersampled field measurements could be replaced or supplemented by drone-derived data and to determine the difference between distributions extracted from continuous drone-based imagery compared with those measured along transect lines. Other potential advantages of verified drone-derived images are discussed, with examples of how they can be incorporated into the study of rangelands.

2 Methods

2.1 Study area

The study area is within the Nutrient Effects of Aeolian Transport (NEAT) experiment at the Jornada Experimental Range (JER), New Mexico (Li et al. 2007). The site has a semiarid climate (Buffington and Herbel 1965). Based on recent 5-year U.S. climate data (www.usclimatedata.com), mean annual precipitation is 250 mm with more than 60% of the rainfall occurring from June to October as a result of the North American Monsoon (Adams and Comrie 1997). The mean direction of the wind is southwest, with wind erosion events happening mainly in the spring (Breed and Reheis 1999). The dominant shrub is honey mesquite (*Prosopis glandulosa*) and the dominant grasses are dropseed (*Sporobolus spp*) and black grama (*Bouteloua eriopoda*) (Li et al. 2007). The NEAT experiment has three blocks, with each including five treatments (25 × 100 m) aligned parallel to the prevailing wind (Figure 1). There is a 25 m buffer between treatments to minimize the interference between them. The treatments are divided into 25 × 50 m upwind areas and 25 × 50 m downwind areas. In the upwind areas, grasses were manually removed (from 100% [Treatment 4] to 0% [Treatment Control] of its original cover) in 2004 and have been maintained at similar levels since. Six permanent 50-m transect lines (three upwind and three downwind) are marked by evenly distributed rebar rods on each of the treatments.
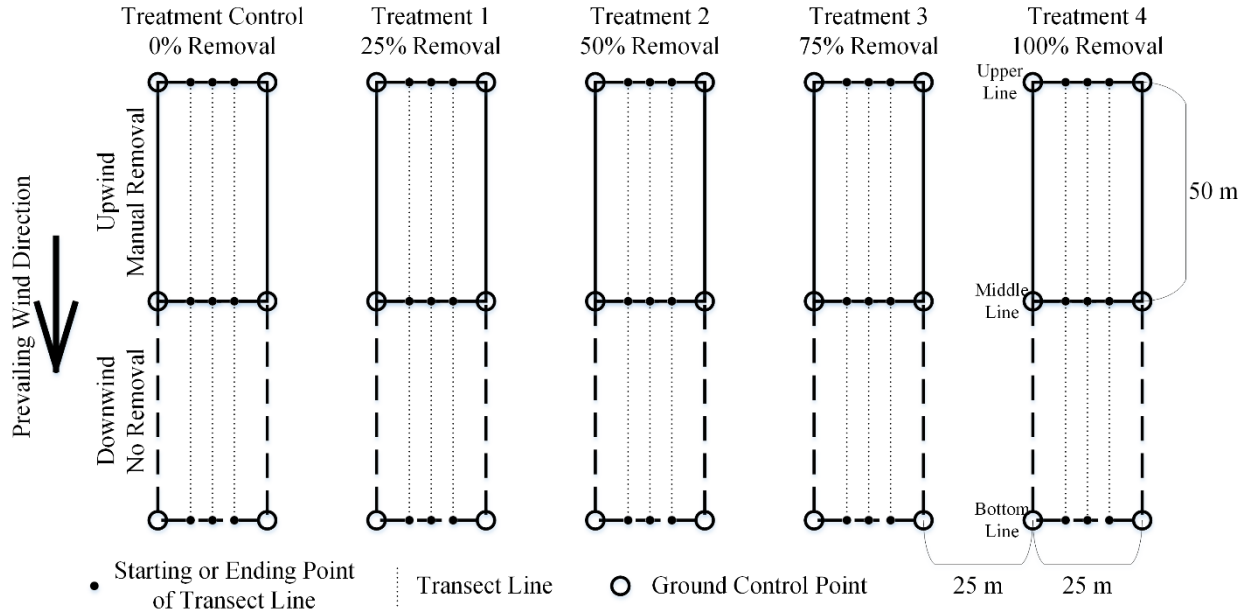
Figure 1 The layout of one block of the NEAT experiment (after Li et al., 2007).

2.2 Data acquisition and processing

2.2.1 Field data acquisition

Five rangeland indicators (canopy size, bare soil gap size, plant height, vegetation cover, and bare cover) were measured *in situ* on the NEAT transect lines in the spring (from February 27th to March 5th) and summer (from July 14th to July 16th) of 2017. The sixth rangeland indicator (scaled height) is a derived indicator calculated as bare-soil gap size (x) divided by the height of the upwind plant (h), which is given by:

$$\text{Scaled hight} = \frac{x}{h}, \tag{1}$$

and is a critical indicator of aeolian transport (Okin 2008).

We employed methods developed by Herrick et al. (2017) for these measurements. The gap intercept method was used to measure canopy size and bare soil gap size (Figure 2). The threshold for the smallest measured gap or plant was changed from 20 cm in Herrick et al. (2017) to 25 cm based on the Assessment, Inventory, and Monitoring (AIM) data protocol (MacKinnon et al. 2011). The drop disk method was used to measure plant height (Figure 2). For plant height, a meter stick was placed in the center of the chord produced by the transect tape overlapping a plant canopy. A drop disk (weight: 175 g; diameter: 25 cm) with a hole in the center for the meter stick was then dropped from approximately 10 cm from the tallest part of the plant, and the height was measured where the at-rest drop disk's center intersected the meter stick (Crofts and Jefferson 1999). Line-point intercept (LPI) method was used to measure the first-hit land cover class (Figure 2). LPI method estimates land covers by calculating the proportion of times one type of land cover is intercepted by a thin rod (Herrick et al. 2017; Karl et al. 2017). In this study, four first-hit land cover classes were recorded (i.e., shrub, grass, litter, and bare soil). Shrub and grass were recognized as vegetation cover and bare soil was recognized as bare soil cover in the following sections.

We measured these six rangeland indicators on 30 transect lines (three transect lines in each upwind and downwind area of one treatment) in each of the three blocks. In order to measure these six rangeland indicators on the same transect lines on drone-based images, the high-accuracy Global Positioning System (GPS) location of the starting and ending point of each transect line and additional ground control points (GCPs) on the corners of the treatments were recorded. To easily recognize these points in drone images, a 25-cm diameter target was attached to permanent rebar markers. The locations of the centers of the targets were measured with <10 cm accuracy

using a Trimble Geo XH 6000 Series GPS (Trimble, Sunnyvale, CA). The main sources of measurement error were distance and angle between GPS receiver and the center of the target, so each target was measured 20 times and the average value was used to minimize the manual measurement error. These points were all in the WGS 84 geographic coordinate system.
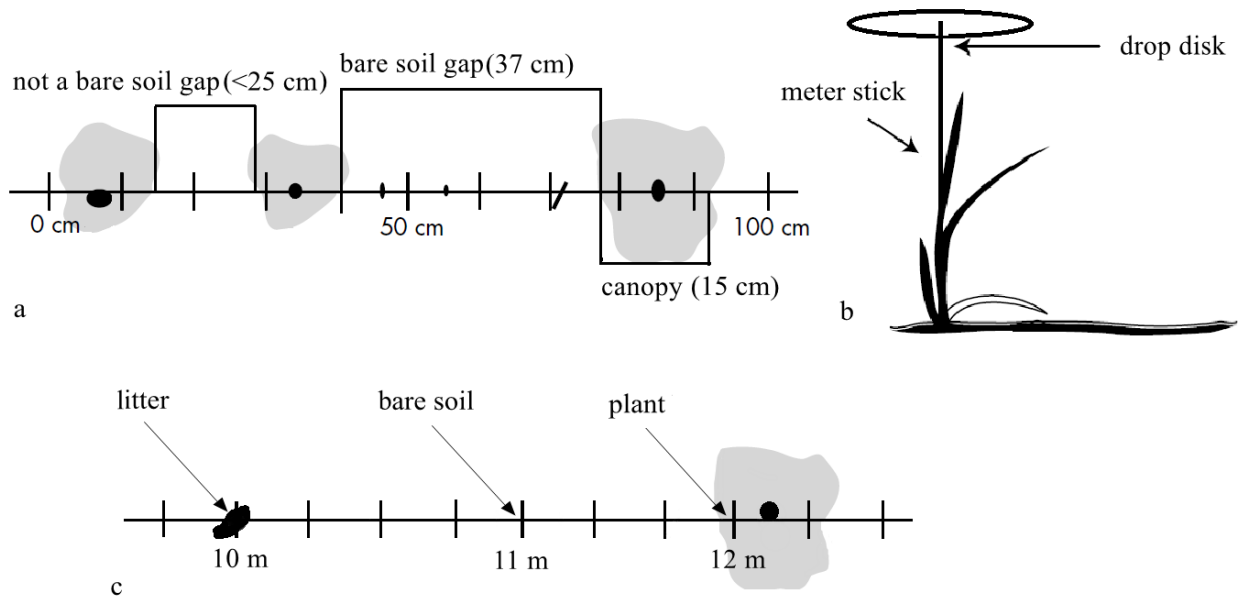
Figure 2 Gap intercept, drop disk and LPI methods to measure canopy size, bare soil gap size, plant height, and land covers: (a) canopy size and bare soil gap size, (b) plant height, and (c) land covers (after Herrick et al., 2017).

2.2.2 Drone-based measurements

A Image acquisition

Images were obtained using a drone on the same day as field measurements. We employed a 3D Robotics Solo quadcopter (3D Robotics Inc., Berkeley, CA) equipped with a GoPro Hero4 camera (GoPro Inc., San Mateo, CA) to survey the three blocks at the NEAT site in the spring and summer

of 2017. A DJI Phantom 4 equipped with its own 4K camera (Dà-Jiāng Innovations Science and Technology Co., Shenzhen, China) was additionally used to obtain images in the summer of 2017. Details about these two flights are given in Table 1. Tower V4 (3D Robotics Inc.) and Map Pilot V2.6.4 (Drones Made Easy, San Diego, CA) were used to initially set up (e.g., flight height and speed) and control 3DR Solo and DJI Phantom 4 drones, respectively. Both camera triggering was controlled by the flight control applications. The sidelaps of GoPro and DJI 4K image were set to 80% and 70%, respectively, which are sufficient to build SfM models of vegetation and landscape (Cunliffe et al. 2016; Daftry et al. 2015). All images were obtained between 11 a.m. to 1 p.m. (local time) to minimize the amount of shadow. The drone was flown twice for each block in different orientations (i.e., north-south and east-west) following a "lawnmower" moving pattern to acquire structural information from different aspects (Figure 3). These two flights on each block were finished within 30 minutes, resulting in negligible changes of solar azimuth and elevation angles during the acquisition period. Every point in the orthomosaic was covered 20 times in GoPro images and 9 times in DJI 4K images (Figure 3). The orthomosaic resolution was mainly determined by focal length and field of view (FOV) of the camera, and flying height, but lens distortion also impacts image resolution. DSM cell size was determined by average point density of dense point cloud, which is impacted by lens distortion (e.g., fisheye).

Table 1 The specifications of the drones and the cameras.

Aircraft	3DR Solo	DJI Phantom 4
Sensor	GoPro Hero4	DJI 4K camera
Image size	4000×3000	4000×3000
Camera type	Fisheye	Frame
Flying height (m)	12	20
Time of shot (s)	0.33	1
Image sidelap (%)	80	70

FOV (degree)	122	94
Image count	~800	~300
Average point density (points/m^2)	806	1220
Orthomosaic resolution (mm)	9	7
DSM cell size (cm)	3.6	2.8
GPS information	No	Yes
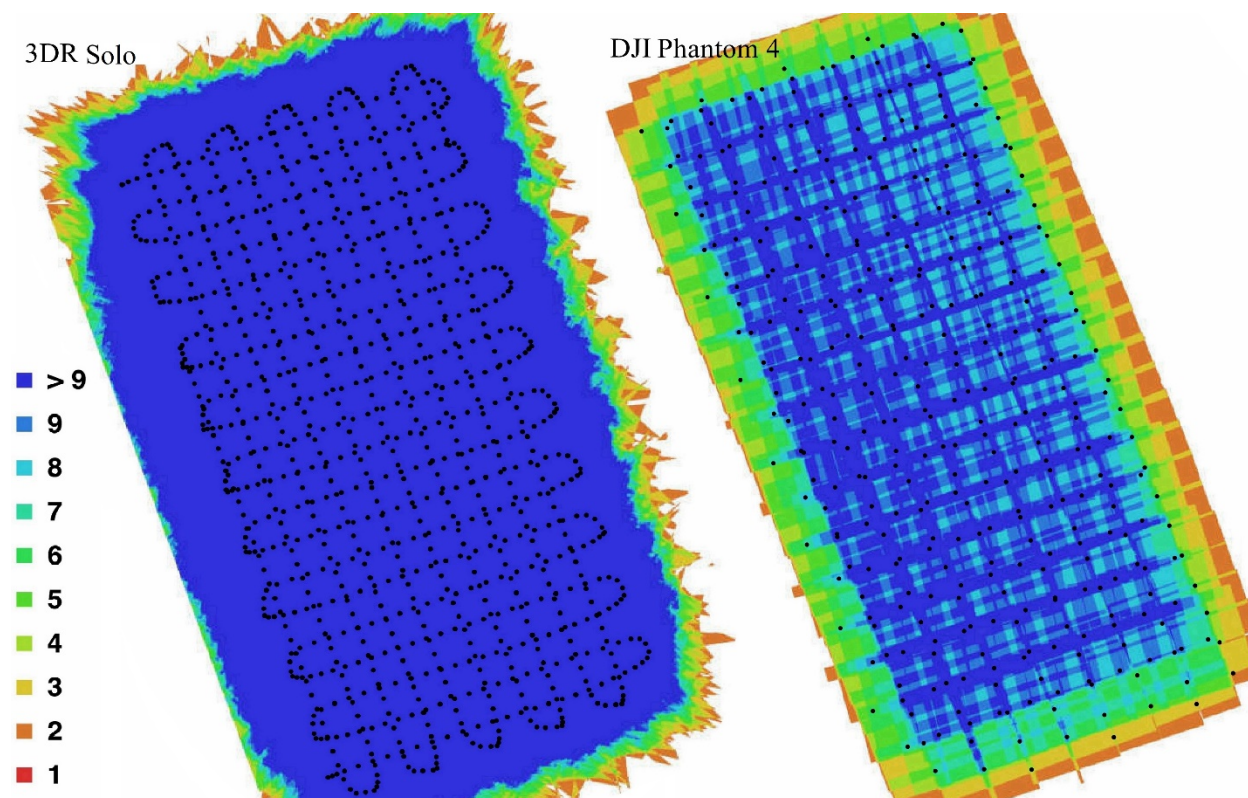
Figure 3 The repeated cover of one frame view and the location of photos taken by the cameras (using Block 3 as an example). The color represents the number of repeated observations. Black dots are the locations where the cameras took photos. The left panel shows the flying path of 3DR Solo in the spring of 2017 and the right panel shows the flying path of DJI Phantom 4 in the summer of 2017.

B Image processing

The images were processed using commercial SfM software (PhotoScan V1.2.5, Agisoft LLC, St. Petersburg, Russia). There are four general steps for SfM image processing: 1) photo alignment and sparse point cloud building, 2) GCPs identification and sparse point cloud optimization, 3) dense point cloud building, and 4) construction of orthomosaic and DSM. For GoPro images, an additional step of fisheye correction was done before photo alignment to remove lens distortions. PhotoScan has the default parameters (i.e., the focal length in pixel: fx, fy; and principal point coordinates: cx, cy) of GoPro Hero4 for camera calibration, and these default parameters were used to eliminate the fisheye effect. For the images taken by DJI 4K camera, there is little deformation effect, making this step unnecessary.

For photo alignment and sparse point cloud building, "high" accuracy and "generic" pair preselection options were chosen for both image sets. The scale invariant feature transform (SIFT) algorithm, which can automatically search and match the features in different images (Lowe 2004), is employed to align images in PhotoScan. This step creates a sparse cloud that contains the matched features with their calculated X, Y, and Z coordinates either in a relative coordinate space (GoPro) or using an approximate geographic coordinate space (WGS 84) based on GPS location information written in the image headers (DJI 4K).

To rectify the geometry for both image sets, 30 GCPs in each block were manually identified as the center pixels of the GPS targets in the images. Within the bundle georeferencing processes, the following accuracies were set up: the measurement accuracy of a GCP, 10 cm; the measurement

accuracy of a camera, 10 m; the accuracy of a marker in a sparse cloud, 0.1 pixel; and the accuracy of a tie point, 4 pixels. The latter three parameters were defaults in Photoscan.

The dense point cloud is the prototype of SfM model. In this study, "high" quality and "mild" depth filtering were selected to build a dense point cloud. The average point densities for dense cloud were 806 points/m^2 and 1220 points/m^2 for GoPro and DJI 4K cameras, respectively. Orthomosaics were produced from dense point cloud by orthographic projection. DSM was produced from triangular irregular networks (TINs) based on a linear interpolation of the dense point cloud. In the end, GoPro images resulted in 9 mm and 3.6 cm resolution for orthomosaics and DSMs, respectively. DJI 4K image resulted in 7 mm and 2.8 cm resolution for orthomosaics and DSMs, respectively.

To assess the spatial accuracy of orthomosaics and DSMs, the spatial RMSE was calculated in the SfM-derived image (Table 2). The average RMSE represents the error between the location of the GCPs and the centers of the targets in orthomosaics across the three blocks. The orthomosaics produced using images of DJI 4K camera in the summer are more accurate than those produced by GoPro camera during the summer (Table 2). Therefore, we will only discuss the results obtained using GoPro in the spring and DJI 4K camera in the summer.

Table 2 Evaluation of the accuracies of SfM models based on GoPro and DJI 4K cameras. X represents longitude, Y represents latitude and Z represents altitude.

	Time	RMSE X (cm)	RMSE Y (cm)	RMSE Z (cm)	Total XY RMSE (cm)
GoPro camera	2017 Spring	2.95	4.25	6.00	5.17
	2017 Summer	3.23	3.05	3.25	4.43
DJI 4K camera	2017 Summer	1.52	2.49	1.46	2.92

C Rangeland indicators measurement on orthomosaics and DSMs

Bare soil gap size, canopy size, vegetation cover, and bare soil cover were manually measured on the classification maps derived from the orthomosaics (Zhang et al. 2013; Zhang et al. 2012). Protocols (e.g., gap intercept and LPI method) as similar as possible to those used in the field were used to measure bare soil gap size, canopy size, vegetation cover, and bare soil cover on the classification maps. To measure the plant height, we used the classification map to mask the DSM to extract the vegetation feature, which is a digital terrain model (DTM), using the method created by Gillan et al. (2014). Plant height on a transect chord was manually measured from DTMs as the difference between the tallest on the chord and the mean value of the nearest bare soil falling on the transect line on both sides of the plant from the DSMs. This approach allows for the separation of plant height from topographical variation in the soil.

Although the measured segments and points in the classification maps and DTMs derived from the dense point clouds are not the same exact ones measured *in situ* due to the spatial error in the images and unavoidable bends in the transect tape in the field, these results represent a lower bound of the accuracy of the drone-based estimate.

2.3 Evaluation of results

Four statistics were employed to evaluate the correlation of canopy size, bare soil gap size, plant height, scaled height, vegetation cover, and bare soil cover between drone-based estimates and field measurements. The coefficient of determination (R^2) represents how well the drone-based estimates correlate with field measurements:

$$R^2 = 1 - \frac{\sum_{t=1}^{n}(x_t - \hat{x}_t)^2}{\sum_{t=1}^{n}(x_t - \bar{x}_t)^2}, \tag{2}$$

where x_t represents the value of field measurement, $\hat{x}_t$ represents the value of drone-based estimates, and $\bar{x}_t$ represents the mean value of field measurement. Mean error (ME) is given by:

$$ME = \frac{1}{n}\sum_{t=1}^{n}(\hat{x}_t - x_t), \tag{3}$$

and serves as an estimate of the bias of the drone-based estimates compared to the field measurements. The root-mean-square error (RMSE) for the drone-based estimates based on field measurements (as opposed to the spatial RMSE in the orthomosaics discussed above) is given by:

$$RMSE = \sqrt{\frac{\sum_{t=1}^{n}(\hat{x}_t - x_t)^2}{n}}, \tag{4}$$

and serves as an estimate of the total error of drone-based estimates relative to the field measurements. The root-mean-square relative error (RMS RE) represents the error of the drone-based estimates relative to the magnitude of field measurements and is useful for cases where results span a large range:

$$RMS\ RE = \sqrt{\frac{\sum_{t=1}^{n}\left(\frac{\hat{x}_t - x_t}{x_t}\right)^2}{n}}. \tag{5}$$

3 Results

One orthomosaic and one DSM were produced from drone-based remote sensing images for each

block at the NEAT site, but we present only the orthomosaic of Block 3 as an example to show the

visual results. The orthomosaic of Block 3 produced from images taken in the spring and summer

of 2017 show that in the upwind areas, there is a clear decreasing trend of grass removal from the

upwind portions of Treatment 4 (100% grass removal) to Treatment Control (no grass removal;

Figure 4). In the downwind areas where there has been no manual grass removal, the decreasing

trend of grass reduction caused by wind erosion is obvious in the upwind portions of the downwind

areas from Treatment 4 to the Treatment Control.
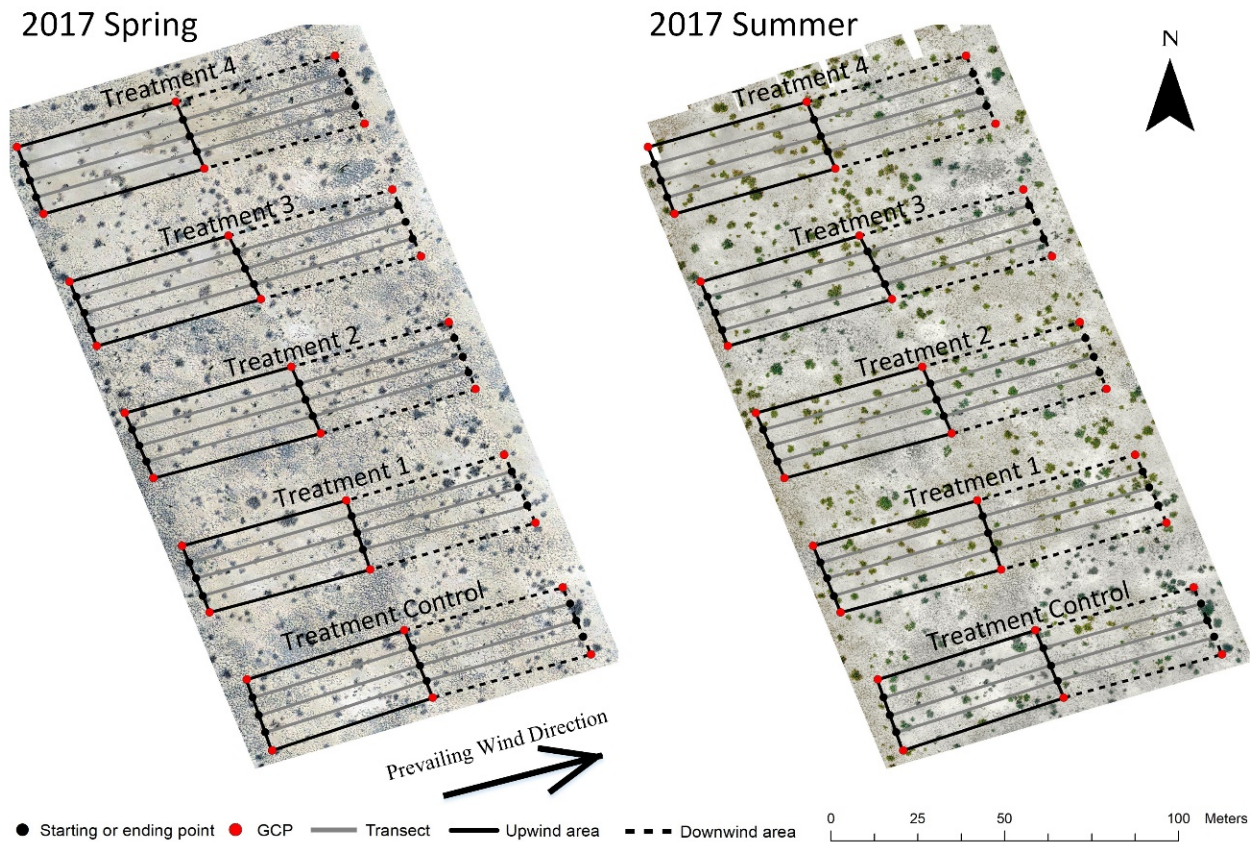
Figure 4 The orthomosaics of Block 3 based on the SfM models. The image on the left was produced using photos taken in the spring of 2017, and the image on the right was produced using photos taken in the summer of 2017. The mesquite shrubs appear greener in the summer image because they have leaves whereas in the spring image, they are dormant.

The correlation between transect-averaged drone-based estimates and transect-averaged field measurements indicate excellent agreement between the two in most cases (Figure 5). The correlations between drone-based and field-measured canopy size, bare soil gap size, bare soil cover, and vegetation cover in the spring and summer show a very strong linear relationship between drone-based estimates and field measurements. The ME, RMSE, and RMS RE of canopy size, bare soil gap size, bare soil cover, and vegetation cover in the summer are at least half of those in the spring.

The relationship between plant height measured using the drone and plant height measured in the field in the spring shows a strong linear relationship for short plants (lower than 20 cm). However, the correspondence is weak for taller plants (taller than 20 cm), leading to the lowest R^2 of only 0.76 and a high RMS RE of 0.13. As a consequence, the correlation of scaled height between drone-based estimates and field measurements in the spring had a linear relationship with a positive bias indicating that the drone-based estimates tend to be greater than the field measurements. In contrast, the correlation of plant height between drone-based estimates and field measurements in the summer shows a strong linear relationship even for tall plants, giving an R^2 of 0.97 and RMS RE of 0.04 and the correlation for scaled height between drone-based estimates and field measurements in the summer shows a strong linear relationship and no apparent bias. R^2

for scaled height in the spring was slightly smaller than it in the summer, and the ME, RMSE and RMS RE of scaled height in the summer are smaller than those in the spring.
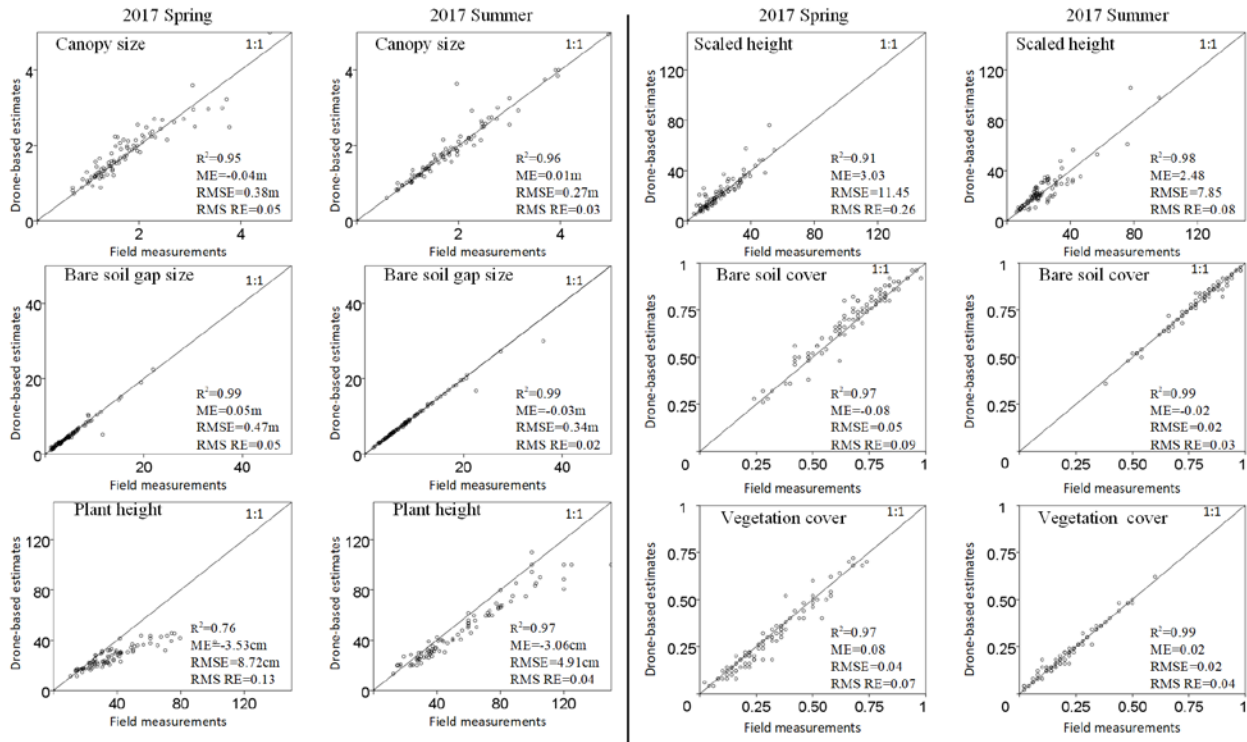
Figure 5 Relationship between drone-based estimates and field measurements for measured indicators where each point in the subplot represents the mean value of one transect of one indicator and the diagonal represents the 1:1 line.

4 Discussions

Overall, our results from the Jornada Basin indicate that drone-based estimates and field measurements of canopy size, bare soil gap size, plant height, scaled height, vegetation cover, and bare soil cover are strongly correlated, particularly when images are acquired during the summer using a camera with no fisheye effect.

4.1 Causes of error

4.1.1 Camera fisheye effect

The fisheye effect of GoPro camera is a potential source of error for the reconstruction of the landscape using SfM and the estimates of these six indicators. The GoPro camera has a very wide FOV (122°) with a strong fisheye effect, which causes severe distortion at the edges of the image. Before photo alignment, we employed four default parameters, including focal length (fx, fy) and principal point coordinates (cx, cy), to calibrate the images. However, it is impossible to eliminate all distortion at the edges of an image. The spatial accuracies of the SfM model based on GoPro and DJI 4K cameras (Table 2) show that SfM model based on DJI 4K camera without fisheye effect has lower RMSEs in the X, Y, and Z directions than those derived using the GoPro camera. The strong deformation at the image edges leads to features that cannot be recognized or may be wrongly identified by the SIFT algorithm. Therefore, the effective information of GoPro images is less than DJI 4K images (Table 1, average point density, orthomosaic resolution, and DSM cell size). Some studies have suggested employing only 60% of a GoPro image in the center to remove the fisheye effect, but the cropped image leads to information loss and impacts the quality of photo alignment (Zhang et al. 2015). Nonetheless, our results indicate that fisheye effect doesn't appear to impact the accuracies of surface indicators such as canopy size and bare soil gap size. It may impact the accuracies of plant height, though in our study these differences cannot be separated from the effect of plant phenology.

4.1.2 Seasonal differences

Canopy size, bare soil gap size, plant height, and scaled height, vegetation cover, and bare soil cover show better correspondence (higher R^2, lower RMSE, lower ME, and lower RMS RE) in the summer than in the spring.

Plant height and scaled height estimated from drone-based products have stronger correlations in the summer than in the spring (Figure 4). In the spring, our results indicate that estimated plant height is closer to the field measurements (though with a small negative bias) when the plant is shorter than 20 cm. In the study areas, most of the plants shorter than 20 cm are grass (mainly *Sporobolus spp* and *Bouteloua eriopoda*), which have a dense canopy in both the spring and summer, allowing the SfM algorithm to identify matching features in images. The plants taller than 20 cm are shrubs (mainly *Prosopis glandulosa*), which have leaves in the summer but lose them in the winter and spring. Our efforts indicate that the shrubs in the 'leaf-on' condition have denser canopies than those in the 'leaf-off' condition, allowing photos taken in the summer to provide more pixels for correspondence in images, resulting in denser point clouds around and in the shrub canopies in the summer compared to spring. This leads to greater accuracy of SfM model and SfM-derived products during the summer 'leaf-on' period. Indeed, the heights measured for the shrubs in the spring are likely closer to the height of the underlying nebkhas (or coppice dunes) than the spindly leaf-free shrubs. The positive bias of the spring scaled height is a direct result of the negative bias of the plant height during that season because the scaled height is calculated with plant height in the denominator (Equation 1), resulting in the overestimate of scaled height in cases where the height is underestimated. Therefore, the plant height and scaled height of the drone estimates in the summer are closer to field measurements.

4.2 Applications

Based on our results, drone-based estimates show strong agreements with *in situ* measurements of six key rangeland indicators, especially during the summer when the canopy of the shrub is well defined. Drone-based remote sensing methods have substantial potential to redefine fieldwork in the future due to three major advantages compared to *in situ* measurement, beyond just the time and money saved in the field. These advantages related to 1) sample size, 2) assumptions of stationarity, and 3) detection of other spatial phenomena, such as anisotropy.

First, drone-based remote sensing can provide a large number of samples compared to field observations. Although transect lines are often considered good representations of an area (Karl et al. 2017), scientists are often limited by the number of transects that can be feasibly measured. Once we have verified that drone-based, high-resolution orthomosaics and DSMs can reproduce measurements on field transect, as in this study, these data provide the opportunity to measure a very large number of possible transect lines in an area along any direction desired, and in places/directions that may have not been seen as useful in the original transect sampling scheme. This is an advantage of reducing confidence intervals, particularly for the confidence interval for the standard deviation (Lee 2014). The magnitude of the confidence interval for the standard deviation decreases more slowly with the number of degrees of freedom than that for the mean. This means that larger sample size is required for estimation of the confidence interval for the variance (as a proportion of variance) than is required for the estimation of the confidence interval of the mean (as a proportion of the mean). For instance, a sample size of 1000 drawn from a normal distribution with mean of 10 and standard deviation of 1.0 allows estimation of the mean within ±0.62% (that is, 95 % confidence interval is [9.938, 10.062]), whereas it only allows estimation of

the standard deviation within ±4.2% (that is, 95% confidence interval is [0.958, 1.046]). In this scenario, nearly 50,000 samples are required to estimate the standard deviation to within ±0.62%.

Thus, the ability to augment a small number of transect measurements made in the field with a large number of transect measurements made on high-quality SfM-derived imagery allows better estimation of both the mean and the variance of a dataset. In practice, we used Treatment 3 in Block 3 as an example: 1000 evenly distributed transect lines parallel to the 6 transect lines (that is, parallel to the main axis of the plots) were measured on our derived summer (leaf-on) orthomosaic with a 5-cm gap between transect lines. On these transects, vegetation cover (i.e., shrub and grass) were measured at 1-m intervals (as used in the field measurements). The estimated vegetation cover, calculated as the average of these 1000 transects is 20.7%. The standard deviation of these measurements is 4.6% and, in this case, represents the variability in cover at the site. With this large number of samples, the uncertainty (with 95% confidence) of the estimate of mean is just 1.9% of the value of the mean and the uncertainty in the estimate of the standard deviation is 6.5%.

Measurement of 1000 transects in the field would be, in most cases, infeasible. More likely would be an estimate based on a handful of transects. In order to evaluate the impact of a small sample size compared to the 1000 transects above, we randomly selected 6 transect lines out of the 1000 transect lines and calculated the average cover for these 6 transects. This was done 1000 times to obtain a histogram of cover estimates that would have been obtained had only 6 transects been measured (as in the field). The average estimate using only 6 transects of vegetation cover is 20.7%,

which is equal to the estimate of vegetation cover using the full sample of 1000 transects (Figure 6). This is not surprising since the average estimate using only 6 transects represents the average of 1000 draws. However, the possible variation in any one of the individual draws is quite large, ranging from 16.2% to 25.1% cover, with about an equal number of under- and over-estimations (Figure 6). In terms of confidence, the 95% confidence interval of the mean estimate from the 1000 evenly spaced transects is [0.203, 0.211], which spans 0.8% cover. In contrast, the average span of the six-transect estimate of the mean spans 15.8% percent cover. The 95% confidence interval of the standard deviation is [0.043, 0.049], which spans 0.6% cover. In contrast, the average span of the six-transect estimate of the standard deviation spans 5% cover. From this simple example, the benefits of being able to make cover estimates (in a manner comparable with field transects) from a raster image, compared to a small number of transects, is clear.
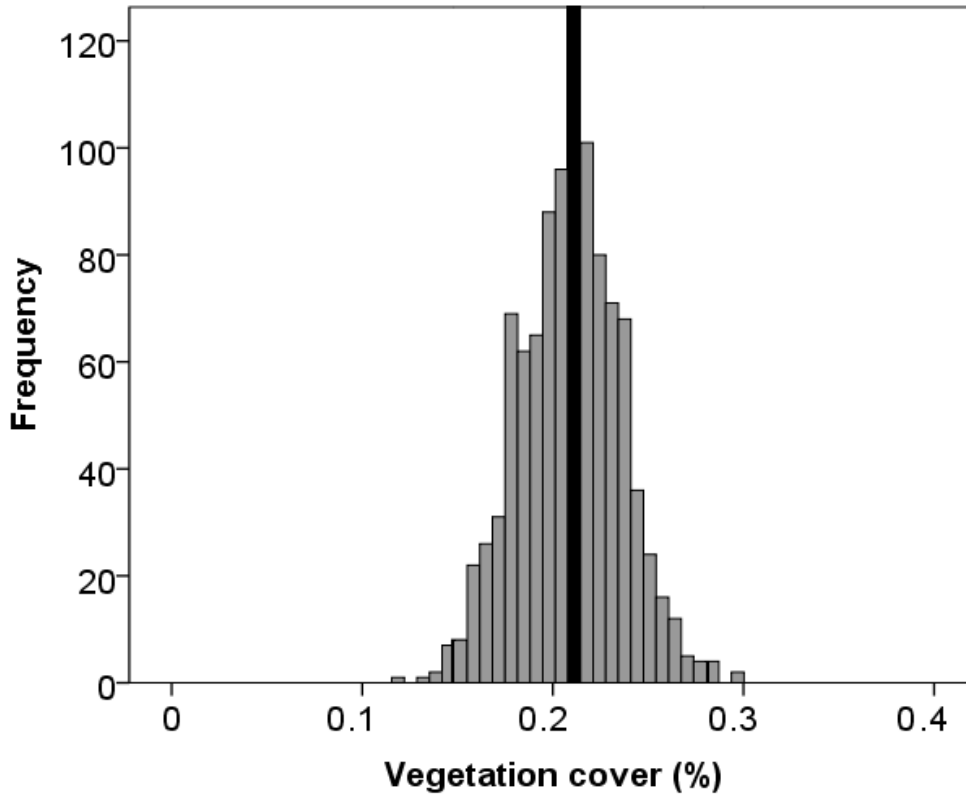
Figure 6 Histogram of mean vegetation cover estimates from 1000 randomly-selected sets of 6 transects (gray bars) and confidence interval (black bar) of mean vegetation cover estimated from 1000 evenly-spaced transects. Transects are pulled from SfM orthomosaic.

Second, transect measurements typically make assumptions about stationarity within the measurement error (that is, the expected value can be calculated only on the basis of the assumption of stationarity). Drone-based remote sensing potentially allows scientists to verify this assumption of stationarity, and if it is found to be lacking, then to design a new sampling scheme, *post hoc*, that is more appropriate. Using Treatment 4 (100% grass removal in upwind area) of Block 3 of NEAT (B3T4) as an example, we extracted 50 equally-spaced transects from classified (grass/litter, shrub, and soil) SfM orthomosaic, aligning them perpendicular to the original field-based transect lines and estimating cover of each type at 0.4-m intervals using the LPI method. The proportion

of each cover type in these transects, spaced 1 m apart, was calculated (Figure 7) Tests for significant linear trends (specifically, an F-test on the slope, Sokal and Rohlf, 1969) were conducted. We observed that the upwind areas of B3T4 exhibit no significant trends and can therefore be treated as stationary (Table 3). In contrast, the downwind areas of this treatment show significant trends for all cover types, with grass/litter and soil cover exhibiting highly significant and nearly equal but opposite trends, and shrub cover exhibiting a barely significant and much smaller slope than the other two. As a result, it might be reasonable to treat the downwind plots as non-stationary in at least some of the cover types. Whatever the application, the original sampling design could not have identified this non-stationarity, thus indicating the value of drone-based imagery for *post hoc* analysis of sampling schemes.

Table 3 p-values for significant linear trends for cover data for B3T4 shown in Figure 7. For significant trends (p <0.05), the slope is given (fraction per meter).

	Grass/Litter	Shrub	Soil
Upwind	0.0981	0.2861	0.0996
Downwind	0.0014 (1.5E-3)	0.0495 (4.9E-4)	0.0001 (-1.9E-3)
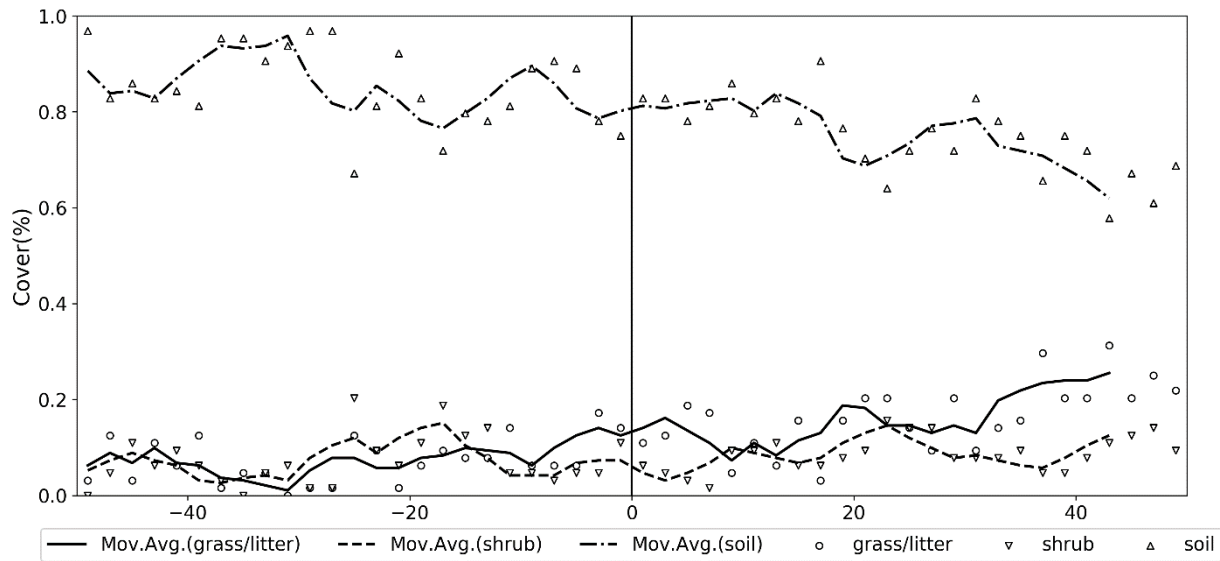
Figure 7 Estimated cover of three cover classes (i.e., grass/litter, shrub, and soil) obtained from a classified SfM orthomosaic of Block 3 of the 100% upwind removal treatment (B3T4) of the NEAT site. Negative distances represent the 'upwind' portion of the site where all grass was removed in 2004. In the 'downwind' portion of the treatments, no vegetation was removed and changes in vegetation cover result from aeolian transport (Alvarez et al. 2012).

Third, drone-based remote sensing can provide an opportunity to observe patterns in a continuous space (i.e., raster imagery), a capability that is impossible with transect sampling. Using Treatment 4 in Block 3 of the NEAT site and the method of McGlynn and Okin (2006), the average size of bare soil patches (i.e. gaps) and vegetation patches was calculated (Figure 8). This analysis shows that average gaps are larger than average plants and that both of them exhibit a marked anisotropy. The direction of the anisotropy of vegetation patches, interestingly, is aligned with the direction of the prevailing wind, suggesting a role of the wind in shaping these mostly grass patches. The shape of bare patches exhibits some complexity, perhaps due to their recent genesis. This result is different from that described by McGlynn and Okin (2006) for a nearby shrub dune land, in which the orientation of the bare soil patches is parallel to the direction of the prevailing wind. This indicates some difference in the patterning of a well-developed dune land and one in which that

process is only incipient (Alvarez et al. 2012). Without raster imagery, this analysis would have been impossible and the comparison with a nearby, different landscape would hot have been possible. However, SfM orthomosaics put these and other spatial analyses within reach in areas where another aerial imagery (or imagery at an appropriate resolution) is not available.
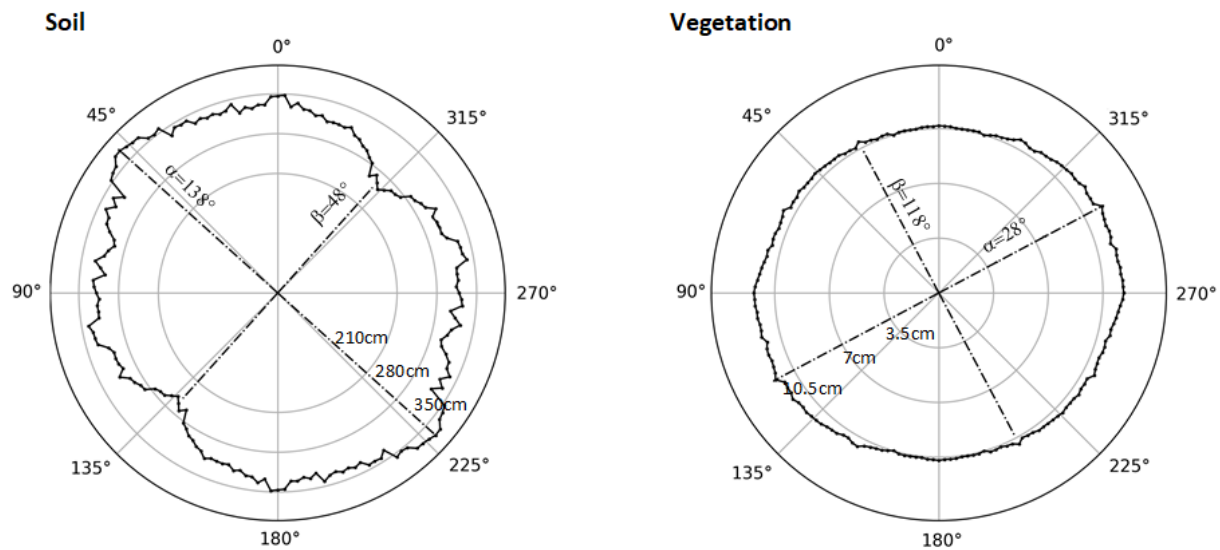
Figure 8 Polar plot of the average size of and inter-plant gaps and vegetation patches using the method of McGlynn and Okin (2006) for the upwind portion of the 100% grass removal treatment in Block 3 of the NEAT experiment (B3T4).

5 Conclusions

In this study, we employed consumer-grade drones equipped with digital cameras to survey six critical rangeland indicators (canopy size, bare soil gap size, plant height, scaled height, vegetation cover, and bare soil cover) at the Jornada Basin LTER during the spring and summer of 2017. Highly accurate SfM models were built based on the ultra-high-resolution images taken by the drones. Comparable measurements were made in the field and on SfM-derived

orthomosaics/DSMs and were found to be, for all intents and purposes, equivalent, especially in the summer when plant phenology improves discrimination of shrub canopies. This comparison can be used to justify the use of the SfM-derived products for other purposes, like reducing the confidence intervals, verifying stationarity, and other spatial applications that use the continuous raster information in the drone imagery.

Over the last few years, there have been many papers on the potential use of drone imagery for a variety of ecological (Cunliffe et al. 2016; Karl et al. 2012; Karl et al. 2017), geomorphological (Gillan et al. 2016; Gillan et al. 2017; Karl et al. 2014; Lucieer et al. 2014), hydrological (Hoffmann et al. 2016; Liu et al. 2016; Tokarczyk et al. 2015), and ecohydrological (Vivoni 2012; Vivoni et al. 2014) applications. In many cases, drone imagery has been suggested as a means to replace difficult fieldwork. However, we caution that care must be taken in ensuring that field measurements and drone-based measurements are very nearly the same, at all times of the year, for this replacement. For ecological work, given the amount of variability that exists in natural landscapes, we suggest that, as we have done here, these comparisons are made on, as nearly as possible, identical transects. As our examples above show, drone-based raster imagery can provide many more opportunities for post-processing of image and data analysis *post hoc*, but we caution that these images must be verified before they should be used in these ways.

References

Adams, D.K., & Comrie, A.C. (1997). The north American monsoon. *Bulletin of the American Meteorological Society, 78*, 2197-2213

Albertson, J.D., Katul, G.G., & Wiberg, P. (2001). Relative importance of local and regional controls on coupled water, carbon, and energy fluxes. *Advances in Water Resources, 24*, 1103-1118

Alvarez, L.J., Epstein, H.E., Li, J.R., & Okin, G.S. (2012). Aeolian process effects on vegetation communities in an arid grassland ecosystem. *Ecology and Evolution, 2*, 809-821

Breed, C.S., & Reheis, M.C. (1999). Desert winds; monitoring wind-related surface processes in Arizona, New Mexico, and California. In: USGPO

Brokaw, N., & Lent, R. (1999). Vertical structure. *Maintaining biodiversity in forest ecosystems*, 373-399

Buffington, L.C., & Herbel, C.H. (1965). Vegetational changes on a semidesert grassland range from 1858 to 1963. *Ecological Monographs, 35*, 139-164

Burke, E.J., Brown, S.J., & Christidis, N. (2006). Modeling the recent evolution of global drought and projections for the twenty-first century with the Hadley Centre climate model. *Journal of Hydrometeorology, 7*, 1113-1125

Crofts, A., & Jefferson, R. (1999). *The lowland grassland management handbook*. English Nature and Wildlife Trusts

Cunliffe, A.M., Brazier, R.E., & Anderson, K. (2016). Ultra-fine grain landscape-scale quantification of dryland vegetation structure with drone-acquired structure-from-motion photogrammetry. *Remote Sensing of Environment, 183*, 129-143

D'Antonio, C.M., & Vitousek, P.M. (1992). Biological invasions by exotic grasses, the grass/fire

cycle, and global change. *Annual review of ecology and systematics, 23*, 63-87

D'Odorico, P., Caylor, K., Okin, G.S., & Scanlon, T.M. (2007). On soil moisture–vegetation feedbacks and their possible effects on the dynamics of dryland ecosystems. *Journal of Geophysical Research: Biogeosciences, 112*

D'Antonio, C.M. (2000). Fire, plant invasions, and global changes. *Invasive species in a changing world*, 65-93

Daftry, S., Hoppe, C., & Bischof, H. (2015). Building with drones: Accurate 3d facade reconstruction using mavs. In, *Robotics and Automation (ICRA), 2015 IEEE International Conference on* (pp. 3487-3494): IEEE

Duniway, M.C., Karl, J.W., Schrader, S., Baquera, N., & Herrick, J.E. (2012). Rangeland and pasture monitoring: an approach to interpretation of high-resolution imagery focused on observer calibration for repeatability. *Environmental Monitoring and Assessment, 184*, 3789-3804

Franklin, J., & Strahler, A.H. (1988). Invertible canopy reflectance modeling of vegetation structure in semiarid woodland. *Ieee Transactions on Geoscience and Remote Sensing, 26*, 809-825

Gillan, J.K., Karl, J.W., Barger, N.N., Elaksher, A., & Duniway, M.C. (2016). Spatially explicit rangeland erosion monitoring using high-resolution digital aerial imagery. *Rangeland Ecology & Management, 69*, 95-107

Gillan, J.K., Karl, J.W., Duniway, M., & Elaksher, A. (2014). Modeling vegetation heights from high resolution stereo aerial photography: An application for broad-scale rangeland monitoring. *Journal of environmental management, 144*, 226-235

Gillan, J.K., Karl, J.W., Elaksher, A., & Duniway, M.C. (2017). Fine-Resolution Repeat Topographic Surveying of Dryland Landscapes Using UAS-Based Structure-from-Motion

Photogrammetry: Assessing Accuracy and Precision against Traditional Ground-Based Erosion Measurements. *Remote Sensing, 9*, 437

Held, I., Delworth, T., Lu, J., Findell, K.u., & Knutson, T. (2005). Simulation of Sahel drought in the 20th and 21st centuries. *Proceedings of the National Academy of Sciences of the United States of America, 102*, 17891-17896

Henderson, F.M., & Lewis, A.J. (2008). Radar detection of wetland ecosystems: a review. *International Journal of Remote Sensing, 29*, 5809-5835

Herrick, J.E., Van Zee, J.W., Havstad, K.M., Burkett, L.M., Whitford, W.G., Bestelmeyer, B.T., Melgoza, A., Pellant, M., Pyke, D.A., & Remmenga, M.D. (2017). Monitoring manual for grassland, shrubland and savanna ecosystems. Volume I: Core Methods. In: USDA ARS Las Cruces, New Mexico. The University of Arizona Press

Hoffmann, H., Nieto, H., Jensen, R., Guzinski, R., Zarco-Tejada, P., & Friborg, T. (2016). Estimating evaporation with thermal UAV data and two-source energy balance models. *Hydrology and Earth System Sciences, 20*, 697-713

Hutchinson, C.F. (1996). The Sahelian desertification debate: a view from the American south-west. *Journal of Arid Environments, 33*, 519-524

Israelsson, H., Ulander, L.M., Martin, T., & Askne, J.I. (2000). A coherent scattering model to determine forest backscattering in the VHF-band. *Ieee Transactions on Geoscience and Remote Sensing, 38*, 238-248

Karl, J.W., Duniway, M.C., & Schrader, T.S. (2012). A technique for estimating rangeland canopy-gap size distributions from high-resolution digital imagery. *Rangeland Ecology & Management, 65*, 196-207

Karl, J.W., Gillan, J.K., Barger, N.N., Herrick, J.E., & Duniway, M.C. (2014). Interpretation of

high-resolution imagery for detecting vegetation cover composition change after fuels reduction treatments in woodlands. *Ecological Indicators, 45*, 570-578

Karl, J.W., McCord, S.E., & Hadley, B.C. (2017). A comparison of cover calculation techniques for relating point-intercept vegetation sampling to remote sensing imagery. *Ecological Indicators, 73*, 156-165

Koenderink, J.J., & Van Doorn, A.J. (1991). Affine structure from motion. *Journal of the Optical Society of America, 8*, 377-385

Laundré, J.W., Hernández, L., Medina, P.L., Campanella, A., López-Portillo, J., González-Romero, A., Grajales-Tam, K.M., Burke, A.M., Gronemeyer, P., & Browning, D.M. (2014). The landscape of fear: the missing link to understand top-down and bottom-up controls of prey abundance? *Ecology, 95*, 1141-1152

Lee, H. (2014). *Foundations of applied statistical methods*. Springer

Li, J., Okin, G.S., Alvarez, L., & Epstein, H. (2007). Quantitative effects of vegetation cover on wind erosion and soil nutrient loss in a desert grassland of southern New Mexico, USA. *Biogeochemistry, 85*, 317-332

Liang, S., Li, X., & Wang, J. (2012). *Advanced remote sensing: terrestrial information extraction and applications*. Academic Press

Liu, X., Chen, Y., & Shen, C. (2016). Coupled two-dimensional surface flow and three-dimensional subsurface flow modeling for drainage of permeable road pavement. *Journal of Hydrologic Engineering, 21*, 04016051

Lowe, D.G. (2004). Distinctive image features from scale-invariant keypoints. *International journal of computer vision, 60*, 91-110

Lucieer, A., Jong, S.M.d., & Turner, D. (2014). Mapping landslide displacements using Structure

from Motion (SfM) and image correlation of multi-temporal UAV photography. *Progress in Physical Geography, 38*, 97-116

MacKinnon, W.C., Karl, J.W., Toevs, G.R., Taylor, J.J., Karl, S., Spurrier, C.S., & Herrick, J.E. (2011). *BLM core terrestrial indicators and methods*. US Department of the Interior, Bureau of Land Management, National Operations Center Denver

McGlynn, I.O., & Okin, G.S. (2006). Characterization of shrub distribution using high spatial resolution remote sensing: Ecosystem implications for a former Chihuahuan Desert grassland. *Remote Sensing of Environment, 101*, 554-566

MEA (2005). *Ecosystems and human well-being: desertification synthesis*. World Resources Institute

Mueller, E.N., Wainwright, J., & Parsons, A.J. (2007). Impact of connectivity on the modeling of overland flow within semiarid shrubland environments. *Water Resources Research, 43*

Okin, G.S. (2008). A new model of wind erosion in the presence of vegetation. *Journal of Geophysical Research-Earth Surface, 113*, 954

Okin, G.S., Parsons, A.J., Wainwright, J., Herrick, J.E., Bestelmeyer, B.T., Peters, D.C., & Fredrickson, E.L. (2009). Do Changes in Connectivity Explain Desertification? *Bioscience, 59*, 237-244

Pellant, M., Shaver, P., & Spaeth, K. (1999). Field test of a prototype rangeland inventory procedure in the western USA. In, *Proceedings of the VI International Rangeland Congress, People and Rangelands, Building the Future* (pp. 766-767)

Rango, A., Chopping, M., Ritchie, J., Havstad, K., Kustas, W., & Schmugge, T. (2000). Morphological characteristics of shrub coppice dunes in desert grasslands of southern New Mexico derived from scanning LIDAR. *Remote Sensing of Environment, 74*, 26-44

Seager, R., Kushnir, Y., Ting, M., Cane, M., Naik, N., & Miller, J. (2008). Would Advance Knowledge of 1930s SSTs Have Allowed Prediction of the Dust Bowl Drought? *Journal of Climate, 21*, 3261-3281

Sokal, R.R., & Rohlf, F.J. (1969). *The principles and practice of statistics in biological research.* WH Freeman and company San Francisco:

Strahler, A.H., Muller, J., Lucht, W., Schaaf, C., Tsang, T., Gao, F., Li, X., Lewis, P., & Barnsley, M.J. (1999). MODIS BRDF/albedo product: algorithm theoretical basis document version 5.0. In: NASA

Thomas, D.S. (1997). Science and the desertification debate. *Journal of Arid Environments, 37*, 599-608

Tokarczyk, P., Leitao, J.P., Rieckermann, J., Schindler, K., & Blumensaat, F. (2015). High-quality observation of surface imperviousness for urban runoff modelling using UAV imagery. *Hydrology and Earth System Sciences, 19*, 4215-4228

Turner, D., Lucieer, A., & Watson, C. (2012). An automated technique for generating georectified mosaics from ultra-high resolution unmanned aerial vehicle (UAV) imagery, based on structure from motion (SfM) point clouds. *Remote Sensing, 4*, 1392-1410

Vierling, K.T., Vierling, L.A., Gould, W.A., Martinuzzi, S., & Clawges, R.M. (2008). Lidar: shedding new light on habitat characterization and modeling. *Frontiers in Ecology and the Environment, 6*, 90-98

Vivoni, E.R. (2012). Spatial patterns, processes and predictions in ecohydrology: integrating technologies to meet the challenge. *Ecohydrology, 5*, 235-241

Vivoni, E.R., Rango, A., Anderson, C.A., Pierini, N.A., Schreiner-McGraw, A.P., Saripalli, S., & Laliberte, A.S. (2014). Ecohydrology with unmanned aerial vehicles. *Ecosphere, 5*, 1-14

Wessels, K., Prince, S., Frost, P., & Van Zyl, D. (2004). Assessing the effects of human-induced land degradation in the former homelands of northern South Africa with a 1 km AVHRR NDVI time-series. *Remote Sensing of Environment, 91*, 47-67

West, N. (1999). Accounting for rangeland resources over entire landscapes. In, *Proceedings of the VI International Rangeland Congress. Aitkenvale, Queensland* (pp. 726-736)

White, M.A., Beurs, D., & Kirsten, M. (2009). Intercomparison, interpretation, and assessment of spring phenology in North America estimated from remote sensing for 1982–2006. *Global Change Biology, 15*, 2335-2359

Zhang, J., Zhu, W., Dong, Y., Jiang, N., & Pan, Y. (2013). A spectral similarity measure based on Changing-Weight Combination Method. *Acta Geodaetica et Cartographica Sinica, 42*, 418-424

Zhang, J., Zhu, W., Wang, L., & Jiang, N. (2012). Evaluation of similarity measure methods for hyperspectral remote sensing data. In, *Geoscience and Remote Sensing Symposium (IGARSS), 2012 IEEE International* (pp. 4138-4141): IEEE

Zhang, T., Guo, F., Bi, N., Forutanpour, B., & Nguyen, P.H. (2015). Systems and methods for producing a combined view from fisheye cameras. In: Google Patents

Chapter 2 Assimilating optical satellite remote sensing images and field data to predict surface indicators in the Western U.S.: assessing error in satellite predictions based on large geographical datasets with the use of machine learning

Abstract: Indicators of the vegetation composition, vegetation structure, bare ground cover, and gap size potentially gives information about the condition of ecosystems, in part because they are strongly related to factors such as erosion, wildlife habitat characteristics, and the suitability for some land uses. Field data collection based on points does not produce spatially continuous information about surface indicators and cannot cover vast geographic areas. Remote sensing is possibly a labor- and time-saving method to estimate important biophysical indicators of vegetation and surface condition at both temporal and spatial scales impossible with field methods. Regression models based on machine learning algorithms, such as random forest (RF), can build relationships between field and remotely sensed data, while also providing error estimates. In this study, field data including over 15,000 points from the Assessment, Inventory, and Monitoring (AIM) and Landscape Monitoring Framework (LMF) programs on Bureau of Land Management (BLM) lands throughout the Western U.S., Moderate Resolution Imaging Spectroradiometer (MODIS) bidirectional reflectance distribution function (BRDF) parameters, MODIS nadir BRDF-adjusted reflectance (NBAR), and Landsat 8 Operational Land Imager (OLI) surface reflectance products with ancillary data were used as predictor variables in a RF modeling approach. RF regression models were built to predict fourteen indicators of vegetation cover and height, as well as bare gap parameters. The RF model estimates exhibited good correlations with independent samples, with a low bias and a low RMSE. Predicted distribution maps of the surface indicators were produced by using these relationships across the arid and semiarid Western U.S.

The bias and RMSE distribution maps show that the sample insufficiency and unevenly pattern of sample strongly impact the accuracy of the RF regression and prediction. The results from this study clearly show the utility of RF as a means to estimate multiple dryland surface indicators from remotely sensed data.

1 Introduction

The Western US is largely composed of arid and semiarid lands that provide a variety of important ecosystem goods and services, but land degradation in these areas, a critical global issue in the 21st century (Bestelmeyer et al. 2015), can be severe. In the mostly dry Western US vegetation can be sparse and composed of a mix of life forms (i.e., woody and herbaceous plants), often with a considerable amount of non-photosynthetic vegetative material. This complex vegetation structure and bare soil cover are important in regard to the functioning of these lands. For instance, large amounts of bare connected soil can make these environments susceptible to erosion by wind and water (Ludwig et al. 2007; Okin et al. 2009). As a result of the need for monitoring, specialized biophysical surface indicators of vegetation and surface condition have been developed for dryland ecosystems (e.g., Herrick et al. 2015). The large variations in bare soil cover, vegetation cover, and vegetation structure at different landscape levels are strongly related to erosion, determine wildlife habitat characteristics, and control the suitability for some land uses, making the use of multiple indicators critical in the monitoring and management of lands in the Western US and elsewhere (Herrick et al. 2010; Knippertz and Stuut 2014). As the largest manager of land in the arid and semiarid Western U.S., the Bureau of Land Management (BLM) has developed the Assessment, Inventory, and Monitoring (AIM) and Landscape Monitoring Framework (LMF)

programs to systematically collect information on lands it manages throughout the western states (MacKinnon et al. 2011).

In situ observation is a commonly used method to measure surface conditions. Field data collection based on points does not provide spatially or temporally continuous information about the surface and is susceptible to under-sampling, even in a relatively small area (Karl et al. 2014). Moreover, measuring surface indicators *in situ* is time-consuming and laborious, especially in harsh or remote areas (Elzinga et al. 1998; Holthausen et al. 2005). Remote sensing is a practical method for detecting surface indicators at different temporal and spatial scales within a short time frame (Sun et al. 2008). Several studies have shown that assimilating satellite remote sensing images and field data can generate surface indicators at relatively large landscape scales (Booth and Cox 2009; Jones et al. 2018; Karl et al. 2012; Laliberte et al. 2004; Luscier et al. 2006; McCord et al. 2017). However, remote sensing techniques may have difficulty measuring all surface indicators with the required accuracy and precision (Marsett et al. 2006). In addition, the relationship between surface reflectance and surface indicators is usually nonlinear (Duniway et al. 2012) and the spatial cover and temporal density of field data collection can be limited. The small training sample size and nonlinearity make the use of traditional regression approaches problematic for assimilating remote sensing images and field data (Duniway et al. 2012; Liang et al. 2012). Machine learning algorithms, on the other hand, which were developed first by artificial intelligence scientists, excel at solving nonlinear problems and can overcome the issue caused by small sample size (Lary et al. 2016). As examples, a Bayesian additive regression tree (BART) model has been applied to estimate six surface indicators in Northern California and Nevada based on AIM data and high spatial resolution satellite images (McCord et al. 2017); a 30-m annual vegetation map of the

Western U.S. was created based on remotely sensed and field data by using the random forest (RF) regression approach (Jones et al. 2018); and a 100-m soil property and class maps of the U.S. was generated based on land cover and gSSURGO polygon data by using a tree-based regression model (Ramcharan et al. 2018).

In our study, a RF regression model based on the Frequentist framework (Breiman 2001; Herrick et al. 2010; Jones et al. 2018; Leenaars et al. 2017; McCord et al. 2017; Ramcharan et al. 2018) was employed to derive the relationships between AIM and LMF field data and remotely sensed data, combined with ancillary data. We added bidirectional reflectance distribution function (BRDF) parameter products to our machine learning-based regression method to help retrieve the structural indicators (i.e., plant height and bare soil gap size), as BRDF is sensitive not just to surface brightness, but surface architecture as well, and therefore potentially correlates better with structural indicators (Li and Strahler 1986; Jones et al. 2018). The objectives of this study were to: (1) build RF regression models for fourteen biophysical surface indicators of vegetation and surface condition, (2) apply the resulting RF regression models to generate predicted distribution maps for these indicators across the arid and semiarid Western U.S., and (3) provide external k-fold cross-validation estimates of error and map the error distribution in the study area. The addition of external cross-validation, as opposed to the internal cross-validation that inherent to the RF approach, provides the opportunity to understand the limitations on RF predictions in conditions more closely approximating what a land manager might experience. They also provide the opportunity to produce geographical estimates of error to better represent geographical variability in the quality of estimates which may be used to better contextualize predictions or to prioritize the location of new measurements.

2 Random Forest Algorithm

2.1 Decision tree-based modeling

Decision trees are commonly used classification and regression methods in remote sensing analysis (Friedl and Brodley 1997). Decision trees create tree-like models in which each internal node represents a test on an independent variable, each branch represents a criterion of the test, and each 'leaf' represents a result of the test. The tests measure the homogeneity (i.e., Gini impurity or mean squared error, MSE) between a descendant and its parent variable. If the root (i.e., dependent variable) is categorical, this approach yields a "classification tree". If the root (i.e., dependent variable) is continuous, this approach yields a "regression tree". Because the AIM and LMF surface indicators are continuous, we only concern ourselves here with the regression tree approach. The most well-known regression tree approach is the classification and regression tree (CART) algorithm (Breiman et al. 1984; Zhang et al. 2013; Zhang et al. 2012), which is a nonparametric algorithm that recursively partitions the dataset through simple regression models into increasingly smaller subsets by the same splitting decision (i.e., core function). Each simple regression model (i.e., regression plane) only has one dependent variable and the relationship between the regression planes is nonlinear.

Although CART shows good performance in regression, another approach has been to employ an ensemble regression tree model (i.e., additive trees or 'forests'), which is an algorithm that synthesizes multiple related but different models, to improve the accuracy and precision of predictive analytics (Lary 2010). Specifically, for the regression tree model, two or more regression trees are built based on different subsets of training samples (Dietterich 2000). The final

result of the ensemble regression tree model is the weighted result based on the outcome of each tree. RF (Breiman 2001) and BART (Chipman et al. 2010) are the two most commonly used ensemble regression tree approaches.

2.2 Random forest regression model

RF has been successfully used for regression in many disciplines (Pal 2005) and is characterized by the bagging (i.e., bootstrap aggregating) approach (Breiman 1996). RF has three qualities that recommend its use here. First, RF builds multiple regression trees independently by using different bootstrapped sample subsets of training samples (Steinberg and Colla 2009). There may be some outliers in one of the bootstrapped sample subsets, but each tree relies on its own subset, so the sensitivity of RF to outliers is reduced. Second, each node of a tree is split by using a randomly chosen independent variable among the entire set of independent variable (Liaw and Wiener 2002), and RF chooses the subset of trees with the least error as the final output, making RF robust against overfitting (Rodriguez-Galiano et al. 2012). Third, in the bagging approach, RF randomly chooses sample subsets from the training samples with replacement (i.e., bootstrap), which means that even a small dataset can be sampled multiple times making RF resilient to sample insufficiency (Breiman 2001). Although RF has some advantages compared to other machine learning regression algorithms, it is difficult to use it in datasets with missing data (Pal 2005). One advantage of the AIM/LMF sampling approach is that there are very few missing data. Nonetheless, the standard approach of RF in these cases is to separate a dependent variable with missing data into two dependent variables: one continuous variable consisting of the present data and one categorical variable that labels missing data (present data are marked as 1 and missing data are marked as 0). However, adding the categorical dependent variable reduces the importance of

present data and impacts the measurement of the homogeneity (i.e., Gini impurity or MSE) of the original dependent variable (Murphy 2012).

RF has two hyperparameters (parameters that control implementation of the algorithm, in contrast to parameters that are determined through running the algorithm) to control tree growth: the maximum number of independent variables for each tree and the number of trees used to produce the forest. The maximum number of independent variables controls the depth of the tree and is tuned to generate the most efficient expression of the model. The number of trees controls the size of the forest and is tuned to find enough trees to improve the accuracy of the model without overly increasing computational costs. Here, MSE was used as the criterion to split the tree. If the MSE of the descendant node is smaller than a threshold, then the branch stops growing and the leaf of this branch is a possible outcome of the tree. If the MSE of the descendant node is greater than a threshold, then the node is the parent node for the next descendant node. Inherent to the RF approach is out-of-bag (OOB) cross-validation in which samples are divided into different training (usually 70-80%) and validation (usually 20%-30%) sets in the production of each tree, from which an overall OOB error can be estimated (Breiman 2001). In this approach, all data are eventually used to produce the final tree, and thus OOB errors tend to underestimate the true error in the predictions.

2.3 k-fold cross-validation

A complementary approach to cross-validation is external cross-validation, in which small, random samples (usually 5% - 10%) are withheld from the predictions entirely, and then error is estimated based on the final model's ability to predict these withheld points. This typically done

some number, *k*, of times (i.e., k-fold cross-validation) and can be done with- or without replacement. k-fold cross-validation is a commonly used cross-validation method for a machine learning algorithm. The aim of k-fold cross-validation is to employ unseen data to estimate the performance of an algorithm (James et al. 2013; Russell and Norvig 2011). Because the omitted data are not included in the production of the model, these external estimates of error are higher than the OOB errors, but better reflect the error that might be expected by a user of the model (Roberts et al. 2017; Segal 2004; Svetnik et al. 2003). Thus, the advantage of k-fold cross-validation is that it can utilize all samples as training and testing samples, which leads a less biased or less optimistic estimate for the performance of the machine learning algorithm (Kuhn and Johnson 2013). In addition, this approach to cross-validation means that *k* different predictions are made, allowing the production of distribution of estimates that can be used as an indicator of the precision of the estimates. In our study, because each data point is associated with a geographical location, we can make geographically explicit estimates of error which potentially has utility in prioritizing the location of new measurements or spatially contextualizing the quality of a prediction in a certain area.

3 Data and Methodology

3.1 Study area

AIM and LMF measurements taken from 2013 to 2017 in eleven states in the Western U.S. were used in this study (Figure 1). Generally, the Western U.S. has an arid and semiarid climate; however, the west coast of California has a Mediterranean climate (Westerling et al. 2006). Deserts, semiarid and arid areas, and mountains make up most of the land cover in the area. The main types of vegetation are grass and shrub with a small fraction of the forest (Loveland et al. 1991).

The study area covers about four hundred level IV ecoregions based on the National Gap Analysis Project (GAP) dataset according to McMahon et al. (2001). Within each ecoregion, the biotic (e.g., vegetation) and abiotic (e.g., climate) phenomena are similar (McMahon et al. 2001). In our study, we included every ecoregion that contains more than two AIM or LMF sites (Figure 1). The urban areas, dry lakes, and lakes in those ecoregions were removed from the study area by using the GAP dataset (McMahon et al. 2001).
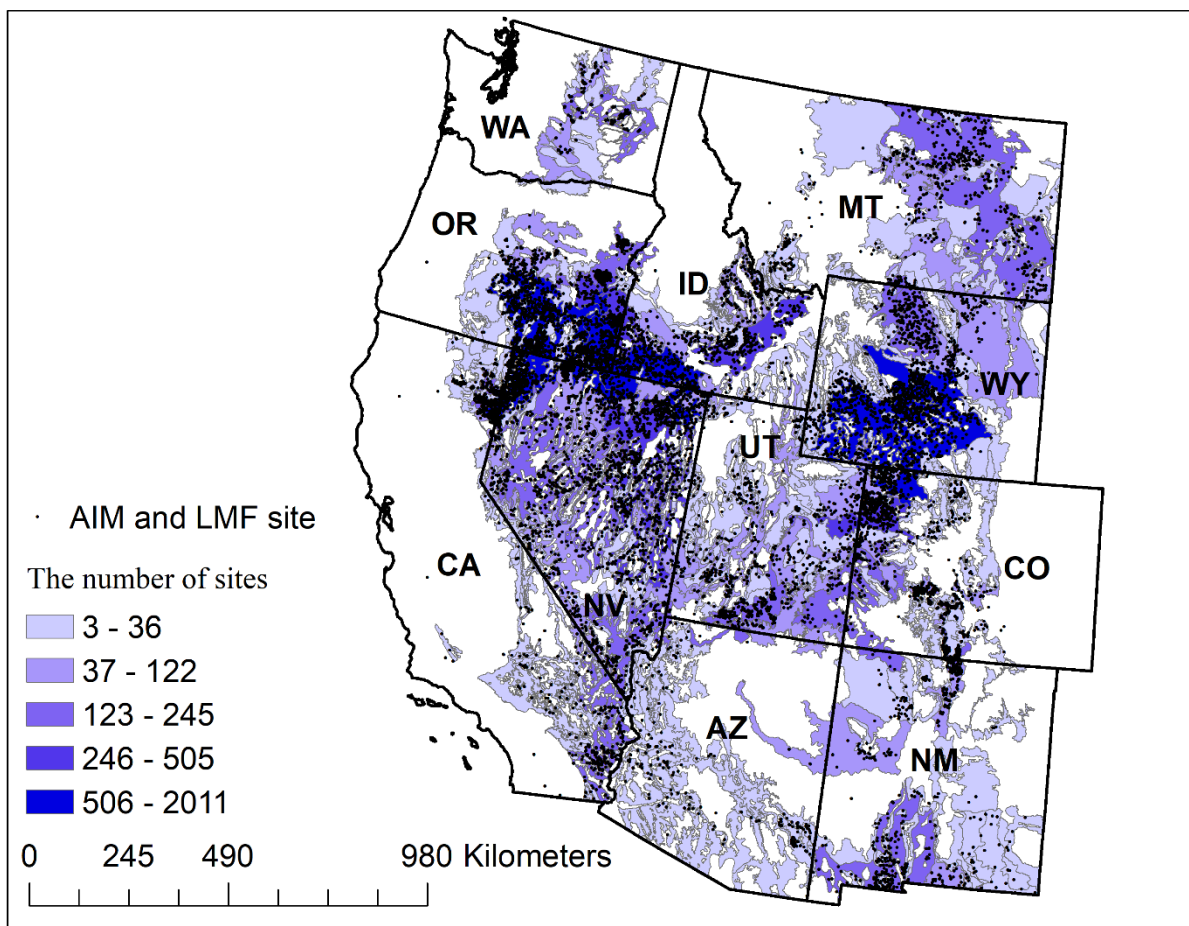
Figure 1 The pattern of Assessment, Inventory, and Monitoring (AIM) and Landscape Monitoring Framework (LMF) sites in the study area (about 400 level IV ecoregions).

50

3.2 Field data collection

The Landscape Approach Data Portal (https://landscape.blm.gov/geoportal) contains field measurements from BLM lands (MacKinnon et al. 2011). The AIM and LMF dataset has a total of 20 common surface indicators including bare ground cover, native vegetation cover, invasive vegetation cover, plant height, and soil stability, measured using consistent methods, such as line-point-intercept (LPI), gap intercept, and belt transect (Herrick et al. 2017; MacKinnon et al. 2011). AIM and LMF data were collected by different BLM surveying and mapping teams (MacKinnon et al. 2011). These teams contributed to approximately 50 projects in different states across the Western U.S. Fourteen surface indicators were selected for this study (Table 1).

Table 1 The list of all surface indicators in this study.

Surface indicators	Description
Gap 25-50	The fraction of the transect comprised of bare soil gaps between 25 cm and 50 cm.
Gap 51-100	The fraction of the transect comprised of bare soil gaps between 51 cm and 100 cm.
Gap 101-200	The fraction of the transect comprised of bare soil gaps between 101 cm and 200 cm.
Gap 201-250	The fraction of the transect comprised of bare soil gaps between 201 cm and 250 cm
Gap > 250	The fraction of the transect comprised of bare soil gaps greater than 250 cm.
Bare soil cover	The percent bare ground cover.
Total vegetation cover	The percent canopy cover of herbaceous and woody plants (both invasive and non-invasive).
Sagebrush cover	The percent canopy cover of sagebrush.
Sagebrush height	The mean value of the heights of living or dead sagebrush.
Herbaceous height	The mean value of the heights of living or dead herbaceous plants.
NInvPerennial Grass	The percent canopy cover of non-invasive perennial grasses.
NInv Shrub	The percent canopy cover of non-invasive shrubs.
NInvPerennial Forb	The percent canopy cover of non-invasive perennial forbs.
InvAnnual Grass	The percent canopy cover of invasive annual grasses.

3.3 Remote sensing products and ancillary data

Three types of remote sensing products and three types of ancillary data were used as independent variables in RF regression models (Table 2). These remote sensing products are Moderate Resolution Imaging Spectrometer (MODIS) BRDF parameters, MODIS nadir BRDF-adjusted reflectance (NBAR), and Landsat 8 Operational Land Imager (OLI) surface reflectance. MODIS data have 500-m resolution and OLI data have 30-m resolution. Ancillary data including climate variables, topographic variables, soil texture variables were also included.

The MODIS BRDF parameters product (MCD43A1) contains the model kernels for each MODIS band obtained from the Ross Thick-Li Sparse BRDF model used by MODIS to characterize the angular distribution of reflected light (Schaaf et al. 2002). For each of the seven MODIS bands (Table 2), there are three kernel weights (i.e., isotropic, geometric, and volumetric). The isotropic kernel weight (k_{iso}) represents the bidirectional reflectance of a simple, flat isotropic scatter, the geometric kernel weight (k_{geo}) represents the bidirectional reflectance of a surface containing a large number of objects (plants), and the volumetric kernel weight (k_{vol}) represents the bidirectional reflectance of a homogeneous thick medium consisting of randomly located scattering plane facets with a particular volume density (Roujean et al. 1992). The MODIS NBAR product (MCD43A4) constitutes a prediction of reflectance viewed from the nadir in each MODIS band (Strahler et al. 1999). The Landsat 8 OLI surface reflectance product contains seven bands and has a much higher spatial resolution and superior noise characteristics compared to MODIS (Roy et al. 2014). For each AIM or LMF site, the nearest neighbor, closest-in-time cloud-free MODIS (daily) and OLI (every 16 days) were extracted from images downloaded from Google Earth Engine.

In addition to the raw MODIS and OLI reflectance products, two vegetation indices were calculated to increase the sensitivity of the dataset to green and non-photosynthetic vegetation (NPV). Although technically, these indices duplicate information present in other predictors, because they are based on those predictors, spectral indices are tuned to highlight certain types of information. Because many of the indicators in this study are related specifically to vegetation and its separation from the soil background, we chose two indices used specifically to separate vegetation from the soil. The normalized difference non-photosynthetic vegetation index (NDNVI) is designed as an index of NPV, and exploits the fact that NPV reflectance decreases from the short wavelength infrared1 (SWIR1; 1400-1700 nm; MODIS Band 6, OLI Band 6) to the SWIR2 (2000-2500 nm; MODIS Band 7, OLI Band 7):

$$\text{NDNVI} = \frac{\rho_{SWIR1} - \rho_{SWIR2}}{\rho_{SWIR1} + \rho_{SWIR2}}, \tag{1}$$

where ρ_{SWIR1} represents the reflectance of the SWIR1 band and ρ_{SWIR2} represents the reflectance of the SWIR2 band (Asner 1998). The normalized difference vegetation index (NDVI) is an index of green vegetation (GV) and exploits the fact that GV absorbs strongly in the red (620-750 nm; MODIS Band 1, OLI Band 5) but reflects strongly in the near infrared (NIR; 750-1400 mm; MODIS band 2, OLI band 4):

$$\text{NDVI} = \frac{\rho_{NIR} - \rho_{red}}{\rho_{NIR} + \rho_{red}}, \tag{2}$$

where ρ_{NIR} represents the reflectance of the NIR band and ρ_{red} represents the reflectance of the red band (Huete et al. 2002).

Climate variables used in this study were monthly mean (30 days prior to the collection date of AIM or LMF samples) precipitation, monthly mean temperature, and monthly mean solar radiation. Monthly mean precipitation, temperature, and solar radiation were taken from the daily surface

weather and climatological summaries (https://daymet.ornl.gov/), which have 1000-m resolution. To keep all climate variables dimensionless, all of them were converted to normalized value (Maclaurin et al. 2016) by using the following equation:

$$\hat{x} = \frac{x - \min(X)}{\max(X) - \min(X)} \, , \tag{3}$$

where $\hat{x}$ represents the normalized value at a certain pixel, x represents the original value at a certain pixel, X represents all the values in the entire study area. The range of all three climate variables used in the RF regression is therefore [0,1], which is also the range of the remote sensing variables.

Topographic variables used in this study were elevation, slope, and aspect derived from Advanced Spaceborne Thermal Emission and Reflection Radiometer (ASTER) Global Digital Elevation Model (GDEM) data with 90-m resolution (Fujisada et al. 2005), downloaded from Natural Resources Conservation Service (NRCS, https://datagateway.nrcs.usda.gov/). To keep all topographic variables dimensionless, elevation and slope were converted to normalized value using Equation 3. Since the impact of aspect is different on the east side and west side, a *-cosθ* function was used at a pixel if the pixel had an eastern orientation (0°-179°), while a *-cos(360°-θ)* function was used if the pixel had a western orientation (180° to 359°) (Hafez et al. 2017; Smith 1977). The range of all three topographic variables used in the RF regression is therefore [0,1].

Soil texture variables used in this study were the fraction of clay, silt, and sand in the topsoil layer, which were derived from USDA's State Soil Geographic Database (STATSGO) with 1000-m resolution (Miller and White 1998), downloaded from NRCS (https://datagateway.nrcs.usda.gov/).

The fractions of clay, silt, and sand are percentages and are therefore unitless. The range of all three soil texture variables used in the RF regression is therefore [0,1].

Table 2 Spatial resolution and number of predictors for remote sensing products and ancillary data.

Variable	Original spatial resolution (m)	Number of bands
MODIS BRDF parameters	500	30
MODIS NBAR	500	7
OLI surface reflectance	30	7
Vegetation indices	500 or 30	4
Climate	1000	3
Topography	90	3
Soil texture	1000	3

3.4 Random forest implementation and mapping

In RF, the remote sensing and ancillary variables were treated as independent variables (X_1….X_n) and each surface indicator was treated as a dependent variable (Y). Fourteen RF models based on the relationships between the fourteen surface indicators and remote sensing and ancillary variables were used to generate the predicted distribution maps. Python 3.6 with Scikit-learn 0.18 package (Pedregosa et al. 2011) was used to create the RF regression models and output of the resulting of cross-validation. ArcGIS 10.4 (ESRI, 380 New York Street, Redlands, CA 92373, USA) was used to extract the pixel value of remotely sensed and ancillary data and generate the predicted distribution maps.

After extraction of the values for remotely sensed and ancillary data (as discussed above), we conducted initial testing of RF models, and finally set 8 as the maximum number of independent

variables in each tree and 100 as the number of trees to produce in the forest to provide a good

balance between error reduction and computation time (Figure 2).
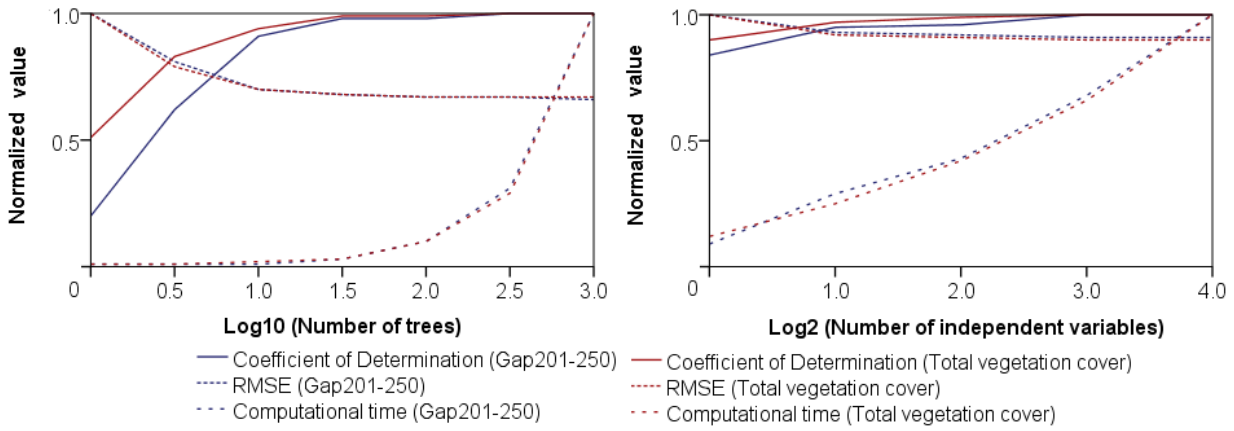
Figure 2 RF regression model performance as a function of number of trees and the maximum number of independent variables

(using the indicator of Gap 201-250 and total vegetation cover as examples). Y axis represents the value in the normalized scale,

which is the ratio of the present value to the maximum value.

In our implementation of k-fold cross-validation, we set k to 20 without replacement. In this

approach, each sample was omitted exactly one time (i.e., 5% omission each time), in random

order, and each surface indicator was predicted 20 times. This led to the production of 20 separate

RF models for each of the fourteen surface indicators. RF models were produced with an 80%-20%

split for training and validation to make out-of-bag (OOB) testing data, from which internal error

(or OOB error) for each model could be calculated. Predictions of the fully omitted 5% of samples

were then made. Thus, for each indicator, each sample point is associated with a single *in situ*

value and a single prediction derived from a model in which the sample was not included in

training data. Each sample point also has 19 (20 minus 1) predictions from models in which the

point was included as training data. And ensemble mean of these 19 points was calculated as the

average of these 19 values.

The contribution of each variable to the overall regression, as the total decrease in MSE from splitting on the variable based on the method of (Pedregosa et al. 2011). The total decrease in MSE provides estimates of the importance of the variables in the RF model results. The contributions reported here are the average of each of the 20 RF models for each indicator.

To produce continuous prediction maps of each of the indicators, 20 individual maps were produced for each indicator, and the final prediction map was calculated as the mean of these 20 maps. Because AIM and LMF data were usually collected from June to September, remote sensing images during the mid-summer were selected to predict the distribution of surface indicators. For the MODIS products, we chose MODIS BRDF parameters and NBAR products collected on July 20th, 2016 that covered the Western U.S. A sequence of images (June 13-August 6, 2016) was chosen to create a cloud-free OLI surface reflectance product to cover the Western U.S. We chose the summer of 2016 to make the prediction maps of surface indicators because this is the summer with the largest number of AIM and LMF points. To provide an idea of the range of predictions produced by the 20 different RF models for each indicator, we calculated the $90^{th} - 10^{th}$ percentile difference for each indicator map.

3.5 Error estimation and representation

Three statistics were employed to evaluate the relationship between model predictions and *in situ* measurements. The coefficient of determination (R^2) represents how well the RF model predictions correlated with *in situ* measurements:

$$R^2 = 1 - \frac{\sum_{t=1}^{n}(y_t - \hat{y}_t)^2}{\sum_{t=1}^{n}(y_t - \bar{y}_t)^2},$$

(4)

where y_t represents a value of *in situ* measurement, $\overline{y}_t$ represents the mean value of *in situ* measurements, and $\hat{y}_t$ represents a value of the RF estimate. R^2 does not, however, provide an estimate for how well the RF model predicts the correct values. For that, additional error metrics are required. Mean error (ME) provides an estimate of the bias of the RF estimates:

$$ME = \frac{1}{n}\sum_{t=1}^{n}(\hat{y}_t - y_t) . \tag{5}$$

The root-mean-square error (RMSE) provides an estimate of the overall error of the RF estimates:

$$RMSE = \sqrt{\frac{\sum_{t=1}^{n}(\hat{y}_t - y_t)^2}{n}} . \tag{6}$$

These three statistics (i.e., R^2, ME, and RMSE) were calculated using both OOB samples and external (from the 5% of samples left out of each RF model) samples to produce estimates of internal and external error, respectively.

3.6 Spatial characteristics of Error

Because each *in situ* data point was geographically located and had associated with it a prediction where it was not included in the training data, our approach allows characterization of the spatial distribution predictions errors. Error (ME and RMSE) distributions for each indicator were estimated and mapped as the mean value of all MEs or RMSEs in each ecoregion in the study area.

In addition, in order to spatially evaluate the ancillary data to the RF regression model, a principal component analysis (PCA) was applied to these ancillary data (climate, topographic and soil texture variables) to identify spatial characteristics that may relate to spatial patterns of error.

4 Results

For the purposes of discussion, we only show five surface indicators, a mixture of structural and non-structural (i.e., Gap>250, Bare soil cover, Total vegetation cover, Herbaceous height, and NInvPerennial Grass cover), representing indicators that were both well-predicted and poorly-predicted. Additional results for the other surface indicators may be found in the supplementary material.

4.1 Model evaluation

Our results indicate strong positive relationships exist between predicted values and *in situ* values, with external R^2 values ranging from 0.21 for the poorly-predicted variable to 0.70 for the well-predicted variables (Table 3 and Figure 3). All of the MEs of surface indicators are positive but with absolute values lower than 0.57 (Figure 3). Most indicators show the same pattern of over-prediction at low values and under-prediction at high values (Figure 3). MODIS BRDF parameters contribute more to the regressions than any other variables. Climate and topographic variables have the second greatest contributions to the regressions. In contrast, MODIS NBAR, OLI surface reflectance, and soil texture contribute relatively little to the regressions (Figure 3). The two vegetation indices for both satellite surface reflectance products contribute very little, so their contributions are not shown. The differences in R^2, ME, and RMSE between OOB samples and external samples are very small (Table 3). For internal predictions (i.e., predictions of points used in the training), correlations are much tighter with R^2 is considerably higher, and |ME| and RMSE considerably lower, than either external or OOB estimates (Table 3 and Figure 4). Internal RMSE for all variables is generally 2.5 times lower than the OOB or external error estimates.
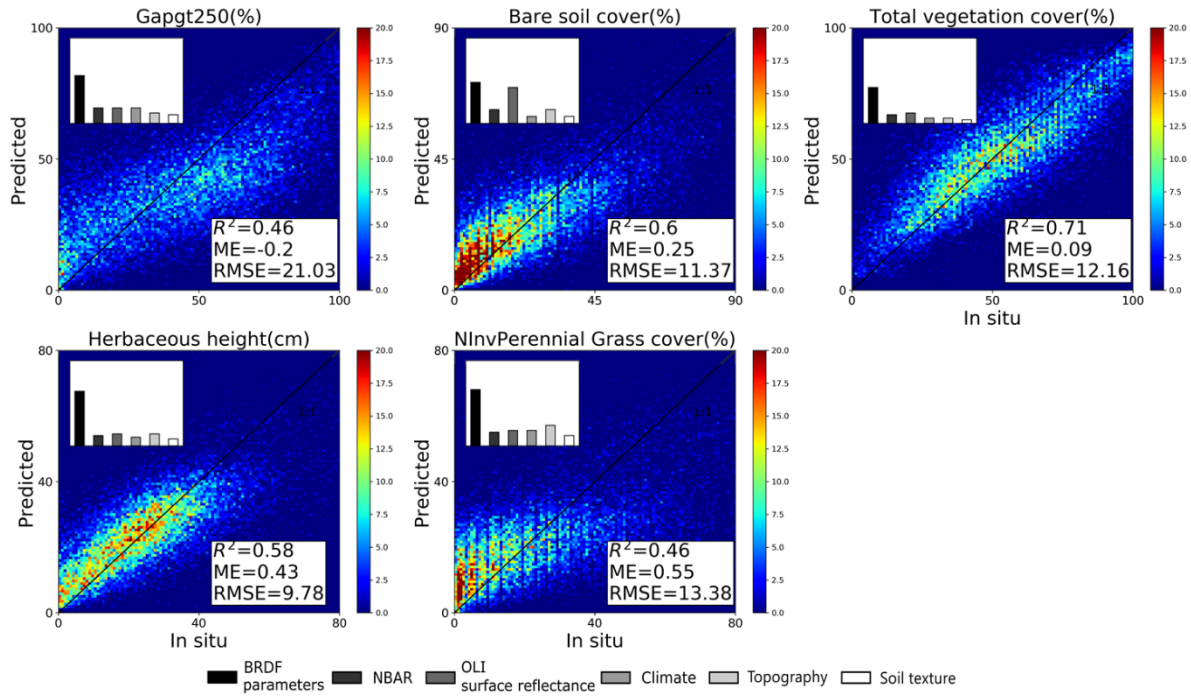
Figure 3 Correlations between model-predicted external values, calculated using the external k-fold cross-validation, and *in situ* values of five surface indicators and the relative contributions of remote sensing and ancillary variables to the regressions (inset). The diagonal represents the 1:1 line. The color bare shows the density of points.
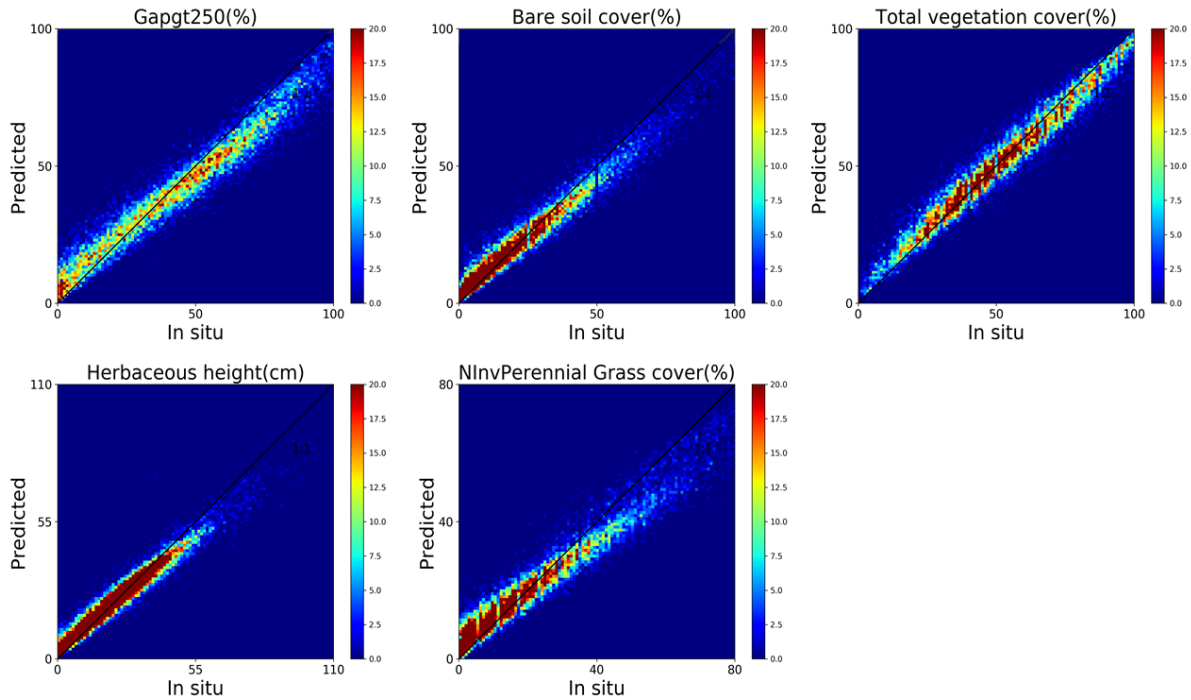
Figure 4 Correlations between ensemble mean predicted and *in situ* values used for internal error calculations.
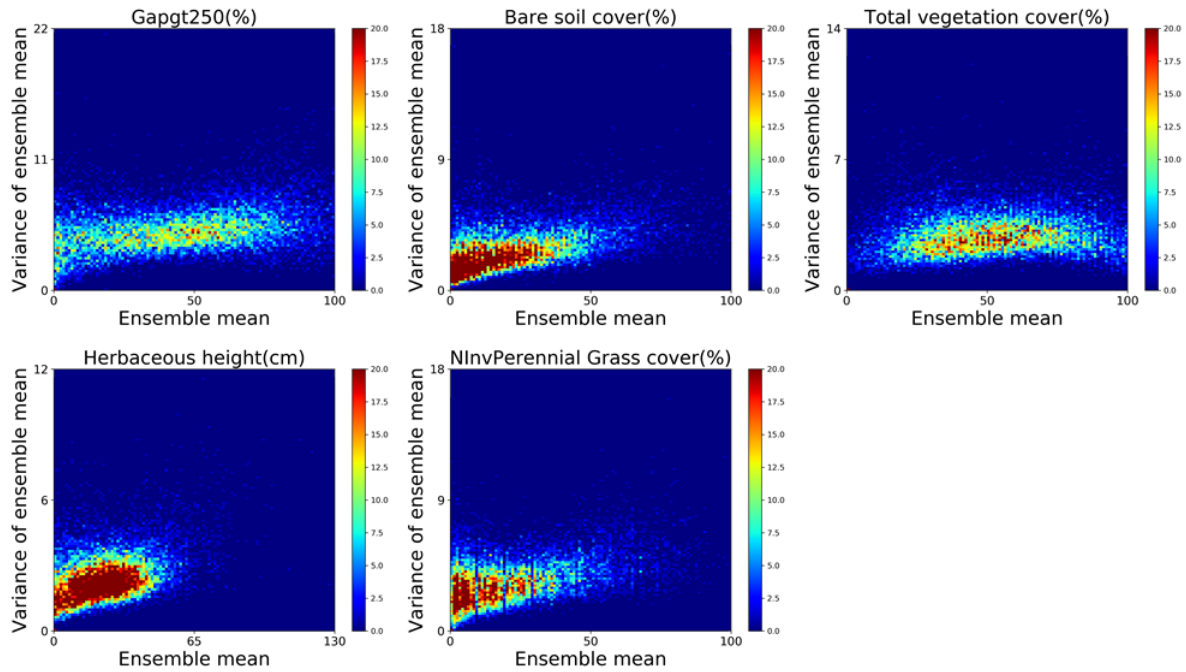
Figure 5 Correlations between ensemble variance (calculated as the difference between the 90th and 10th percentiles of the ensemble of 20 k-fold cross-validation runs) and the ensemble means.

Table 3 Error metrics for individual surface indicators.

Surface indicator	Coefficient of determination			Mean error			RMSE		
	Internal	OOB	External	Internal	OOB	External	Internal	OOB	External
Gap 25-50	0.88	0.23	0.22	0.06	0.04	0.14	1.97	5.08	5.01
Gap 51-100	0.89	0.27	0.26	0.05	0.01	0.11	2.51	6.38	6.37
Gap 101-200	0.89	0.32	0.32	0.08	0.2	0.23	2.89	7.24	7.28
Gap 201-250	0.92	0.48	0.51	0.24	0.46	0.56	5.92	15.34	14.91
Gap >250	0.92	0.44	0.46	-0.07	-0.52	-0.2	8.3	21.14	21.03
Bare soil cover	0.94	0.61	0.6	0.09	0.15	0.25	4.51	11.18	11.37
Total vegetation cover	0.95	0.70	0.71	0.02	0.09	0.09	4.82	12.22	12.16
Sagebrush cover	0.89	0.31	0.31	0.18	0.51	0.48	3.42	8.57	8.69
Sagebrush height	0.88	0.21	0.23	0.32	1.59	0.97	8.41	20.93	21.2
Herbaceous height	0.93	0.56	0.58	0.11	0.7	0.43	3.88	9.77	9.78

NInvPerennial Grass	0.92	0.46	0.46	0.19	0.66	0.55	5.29	13.25	13.38
NInv Shrub	0.89	0.25	0.27	0.17	0.51	0.4	4.18	10.65	10.55
NInvPerennial Forb	0.88	0.24	0.22	0.11	0.3	0.27	1.54	3.86	3.89
InvAnnual Grass	0.9	0.36	0.38	0.25	0.41	0.59	4.46	11.49	11.23

Our results indicate that there are some variances in indicator estimates during the k-fold cross-validation, though the magnitude of the variance is small compared to the range of the predictions, indicating some dependence in the predictions on the input data (Figure 5). For some indicators (e.g., Herbaceous height and NInvPerennial Grass cover), there appeared to be significant correlations between ensemble variance and mean. For other indicators (e.g., Gap ≥ 250 and Total vegetation cover), there was no clear correlation between ensemble variance and mean. This suggests that it is not necessary to take great care when conducting the cross-validation to sub-select points that span the range of indicator values.

4.2 Prediction map

The RF regression models were used to generate predicted distribution maps. The same indicators as shown in Figure 3 were selected to create the predicted distribution maps in eleven selected ecoregions across the Western U.S. (Figure 6). These maps show reasonable patterns of the indicators, showing the lower total vegetation cover, herbaceous height and non-invasive perennial grass cover in more arid regions such as Mojave Basin and Range and Sonoran Basin and Range, as well as a larger cover of Gap > 250 cm in drier regions.
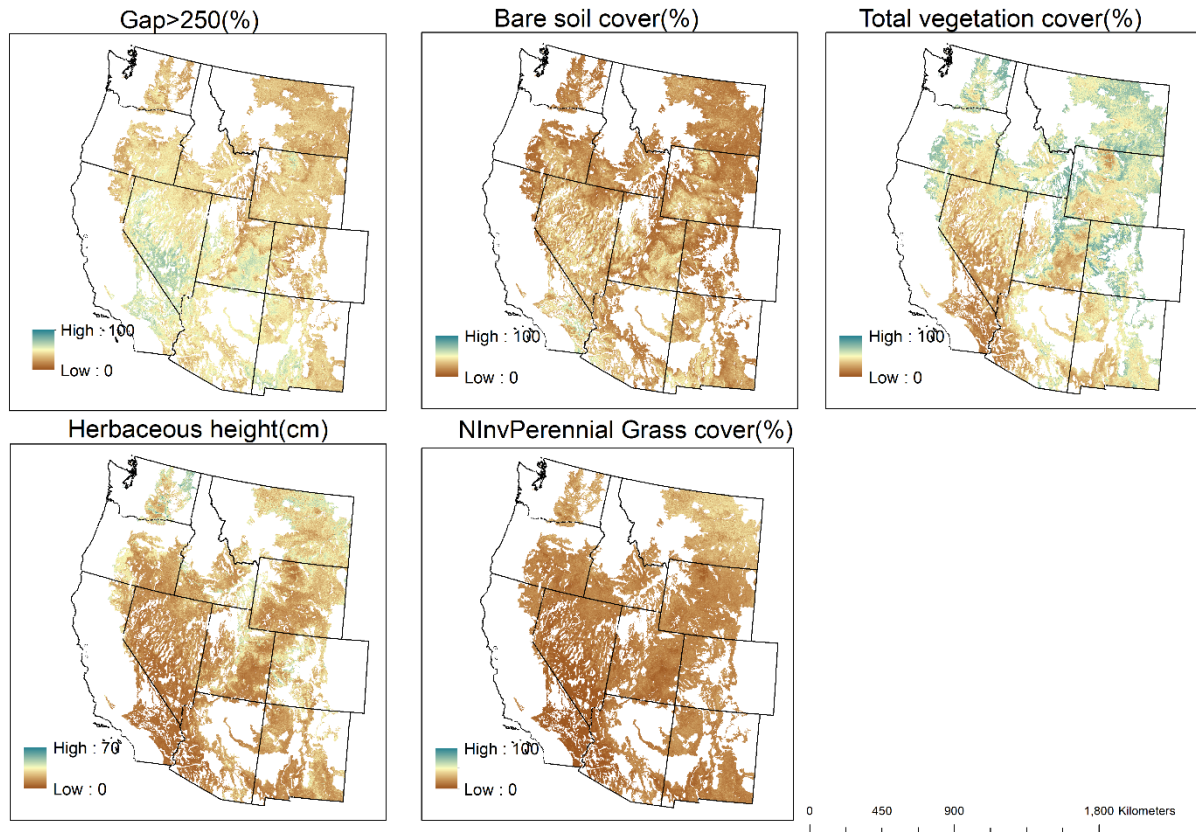
Figure 6 Ensemble mean distribution maps of surface indicators in eleven selected ecoregions of the Western U.S.

4.3 Error distribution maps

Error (ME and RMSE) distribution maps were produced based on the mean value of ME and RMSE of all AIM and LMF sites in each selected ecoregion using the external (cross-validation) errors. The same indicators as shown in Figure 3 were selected to create the error distribution maps in eleven selected ecoregions across the Western U.S. (Figure 7). Compared to the distribution of AIM and LMF sites (Figure 1), ME and RMSE are closer to zero in the areas where have more sites, for example, in the Wyoming Basin and Northern Basin and Range. Despite this, there is no clear geographical pattern for ME or RMSE for any of the variables. For Gap≥250, for instance, positively- and negatively-biased ecoregions abut one another. Likewise, there are no clear relationships between RMSE (Figure 7) and the mean value for individual ecoregions (Figure 6).
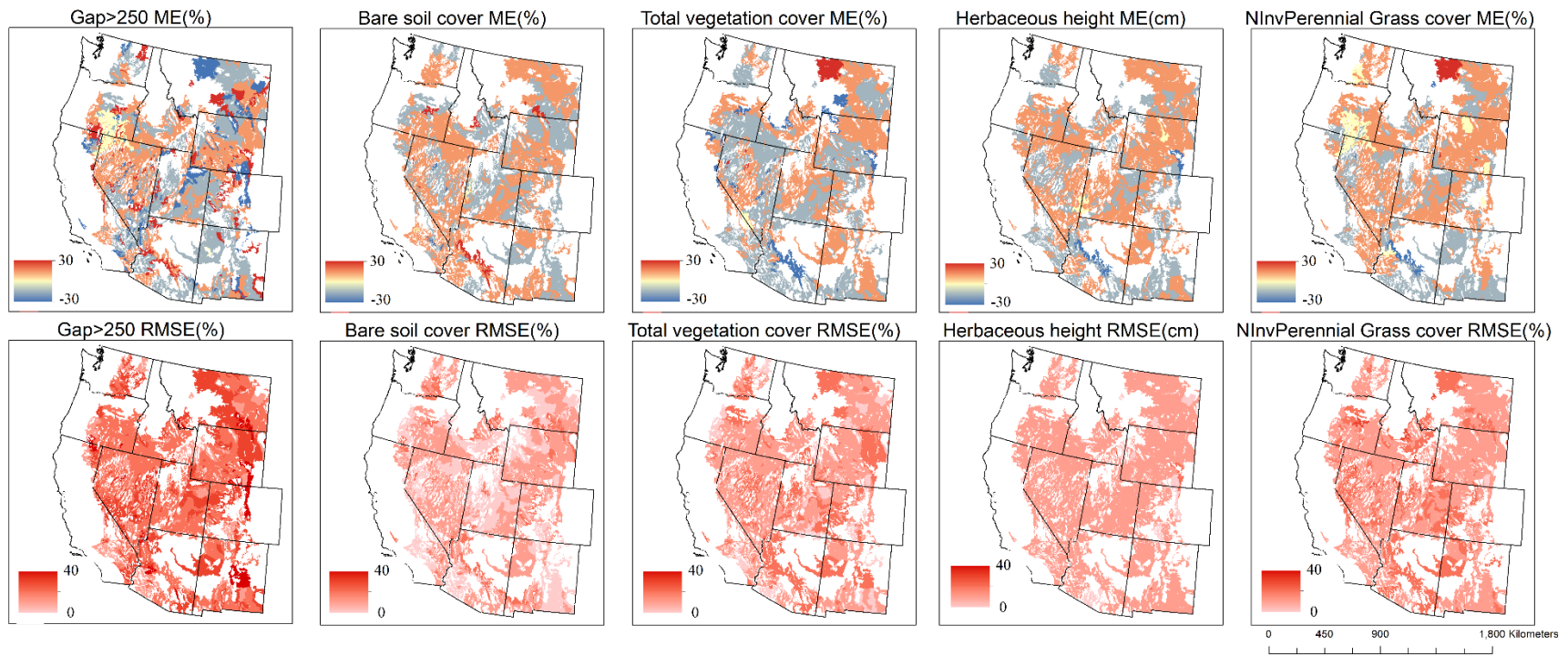
Figure 7 Distribution maps of mean error (ME) and root mean square error (RMSE) of five surface indicators.
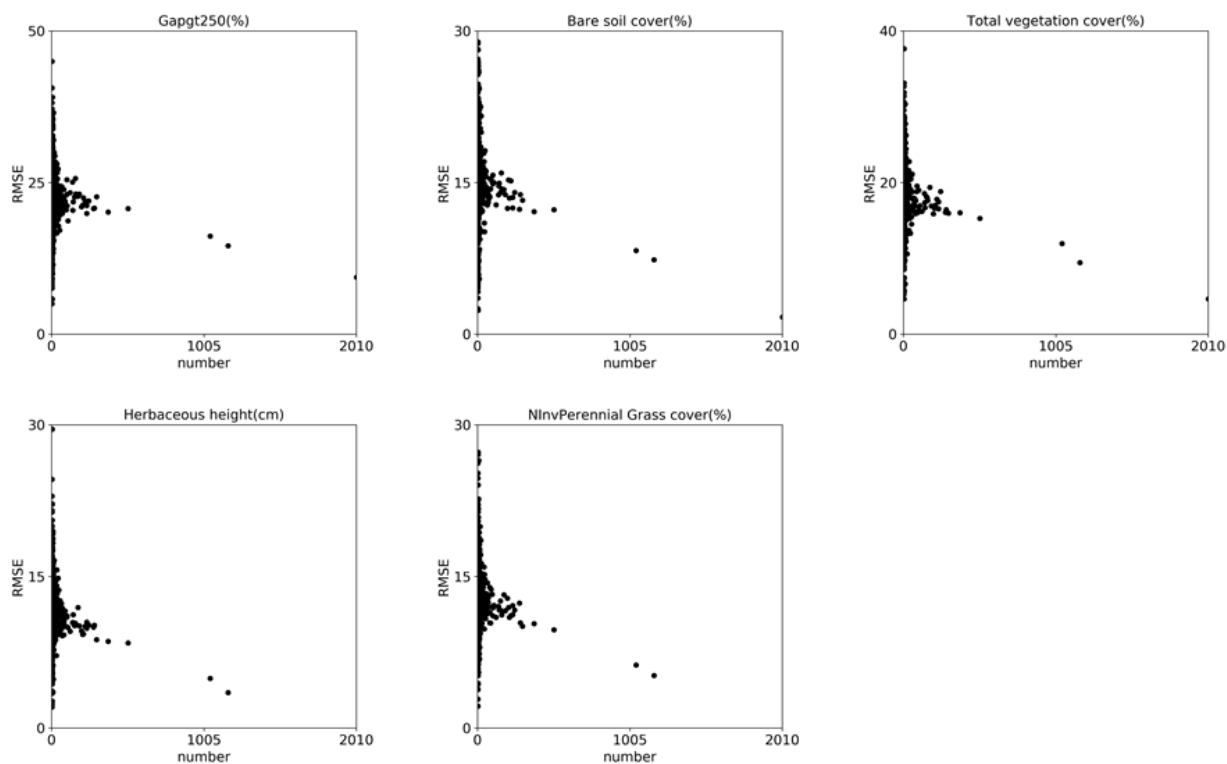
Figure 8 RMSE of predictions in ecoregion polygons plotted against the number of points in each polygon.

Analysis of individual ecoregions, in fact, indicates that ecoregions with a larger number of points tend to have lower error (Figure 8). However, this is a sufficient but not necessary condition. Ecoregions with more than about one hundred points tend to have RMSE below the median. However, there are ecoregions with many fewer points that have lower RMSE than ecoregions with many points.

4.4 Principle components of ancillary variables

The first five principal components (PCs) of the ancillary variables contain more than 80% information on ancillary data (Table 4).

Table 4 The result of principal component analysis for ancillary data.

Component	Eigenvalues	% of Variance	Cumulative %
1	2.39	26.56	26.56
2	1.64	18.31	44.88
3	1.33	14.80	59.68
4	1.00	11.18	70.87
5	0.94	10.48	81.36
6	0.87	9.74	91.10
7	0.58	6.46	97.57
8	0.21	2.35	99.93
9	0.01	0.06	100.00

The first principal component has a strong negative relationship with sand and has a strong positive relationship with clay and silt (Table 5). Compared to the distribution map of PC1 loading, the soil texture variables contribute more on the southern part of the Western U.S. where has much more drylands than northern part (Figure 9). The second principal component has a strong relationship with monthly mean solar radiation and elevation (Table 5). Compared to the distribution map of PC2 loading, elevation and monthly mean solar radiation variables contribute more on the Colorado Plateau than other low elevation areas (Figure 9). The third principal component has a strong negative relationship with monthly mean temperature (Table 5). Compared to the distribution map of PC3 loading, monthly mean temperature contributes more in the low elevation areas than the mount areas (Figure 9). Although aspect and slope have a strong positive relationship with principal component 4 and 5, the distribution maps of PC4 and PC5 loadings don't have obvious trends for these two variables.

Table 5 Component Matrix between the principal component and ancillary data.

	Principal component				
	1	2	3	4	5
Monthly mean temperature	-0.30	0.17	-0.73	-0.10	0.26
Monthly mean precipitation	0.45	-0.32	0.52	0.02	0.06

Monthly mean solar radiation	-0.17	0.90	-0.14	0.06	-0.18
Elevation	0.07	0.76	0.54	0.09	-0.13
Slope	0.12	0.30	0.24	-0.29	0.84
Aspect	0.04	-0.01	-0.06	0.94	0.32
Clay	0.69	0.05	-0.16	-0.08	0.05
Sand	-0.95	-0.12	0.26	0.01	0.05
Silt	0.81	0.13	-0.23	0.03	-0.09
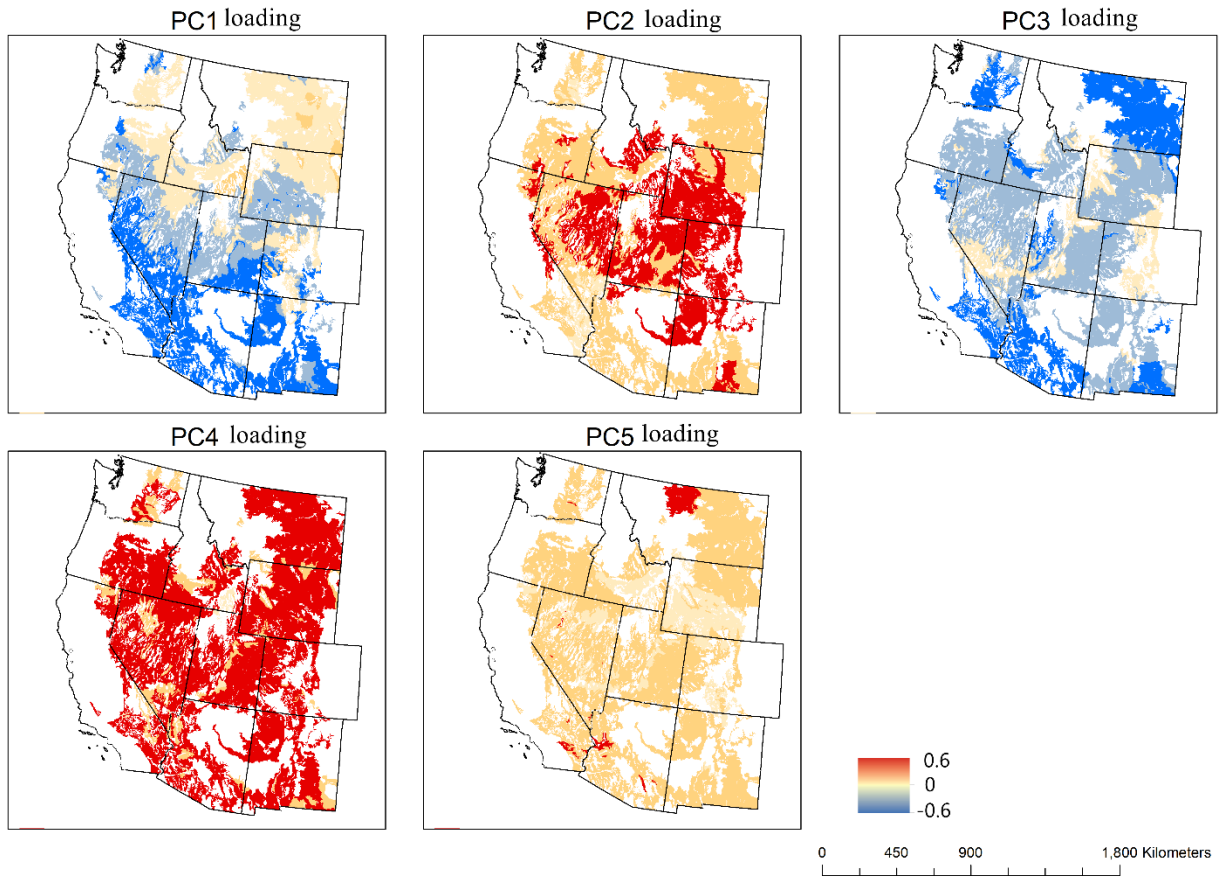
Figure 9 The distribution maps of the first five principal loadings of ancillary data.

5 Discussions

In general, our results indicate that there is potential for using RF to estimate AIM and LMF indicators based on optical remote sensing products combined with location-specific climate, topographic, and soil variables as predictors, though clearly some are more amenable to prediction than others. Based on the RF work so far, the correlations between model prediction and *in situ* measurement and the statistical evaluation of the regressions indicate that assimilating optical satellite remote sensing images and field data can provide good predictions of those indicators in arid and semiarid areas in the Western U.S. This is consistent with recent work by Jones et al. (2018).

5.1 Sample insufficiency and unevenly pattern of the sample

AIM and LMF projects that are on the BLM public lands are measured by different surveying and mapping teams, so there are high concentration AIM samples in specific areas that were targeted for monitoring. In addition, AIM and LMF samples are limited to BLM lands and are not evenly distributed within the study areas. For example, in the Sonoran Basin and Range ecoregion, which covers the part of California and Arizona, AIM and LMF samples are concentrated at Southern California, but there are fewer samples in Arizona (Figure 1). This uneven spatial distribution of samples has the potential to result in incorrect predictions of surface indicators in those areas without any samples (Figure 6). RF regression models can address the problem of sample insufficiency because it adopts the bagging approach, which can convert a small dataset to a large dataset by randomly sampling with the replacement from the original dataset (Breiman 2001). However, RF regression model cannot correct the uneven spatial distribution of input sampling sites. That said, our analysis indicates that a small sample number is not sufficient to produce a

high prediction error (Figure 8). Sample insufficiency is not, alone, a predictor of prediction error at the ecoregion level.

5.2 Contribution of independent variables

Our results clearly indicate that BRDF parameter variables have a strong influence on the RF regression models (Figure 3). This was true regardless of whether the variable quantified cover (i.e., Bare soil cover and Total vegetation cover) or structure (e.g. Herbaceous height and Gap>250). Although the BRDF parameters do not, directly, include information on surface brightness in different bands, we suspect that the differences in BRDF parameters, arising from differences in reflectance nonetheless contain considerable spectral information. Thus, the BRDF parameters are doing double duty, providing information about surface structure through the parameters themselves, and providing information about reflectance through the differences in parameters for different bands.

Although the MODIS pixels are considerably larger than the actual field measurements, which are better matched to the scale of OLI pixels, there is little indication that the finer-scale OLI reflectance contributed more than MODIS reflectance to the RF models. This result is somewhat counterintuitive. Clearly, over smaller scales with a dense network of points, the finer information provided by higher-resolution satellites would be important in differentiating between values. However, for this continental-scale analysis, there does not appear to be a significant advantage of this finer-scale information.

5.3 Appropriate estimators of RF prediction errors

One of the advantages of RF over other methods is its use of bagging, in which, for each iteration, a certain percentage of the data is randomly chosen to be left out of the tree-making process and is held back for testing. In the iterative RF approach where many trees are made, every point is eventually used to produce the final RF model and predictions. Thus, the OOB error for an RF model is based on estimates in which every point is, eventually, used in training. The use of OOB error as a metric of prediction quality has, therefore, been criticized as a form of model overfitting. Our results indicate that the OOB errors and the external error estimates produced through k-fold cross-validation in which there truly are independent samples are nearly identical. We conclude, therefore, that the use of OOB error as a metric of RF prediction quality is an acceptable metric, at least in the application here. Obviously, the use of internal error estimates (in which the final model is used to predict the value of each point which is then compared to the *in situ* value which was used in training) is inappropriate as a metric of error because is dramatically estimates error (in this case by a nearly constant factor of 2.5)

5.4 Spatial distributions of Error

An intuitive assumption about any model prediction is that larger sample sizes produce better estimates (lower error) and that, conversely, smaller sample sizes produce worse estimates (higher error). The first aspect of that assumption appears to be true in the context of this study. Ecoregions with a high number of samples are generally predicted better the median. However, there are many ecoregions with a small number of samples that are predicted as well as, or better than ecoregions with large sample sizes. Therefore, the concentration of samples is not, in and of itself, a predictor of accuracy. In fact, in the analysis presented here, there is little indication of what contributes to

prediction error at the ecoregion level. Considerable additional work will be required to address this issue and it is possible that a relatively simple answer does not exist.

5.5 Limitation of RF

Despite performing well in many cases, RF regression has considerable difficulty in cases where a variable may have a valid value for some points but not others. For example, the indicator of sagebrush height cannot have a value at a site where sagebrush does not exist and using a value of zero for sagebrush height is not equivalent indicating that sagebrush isn't present. In a case such as this, to model the sagebrush height, two variables must be used: a dependent variable (i.e., sagebrush height) with all of the present values of sagebrush height and an additive dependent variable (i.e., sagebrush missing) marking areas where sagebrush is present as 1 and areas where sagebrush is not present as 0. The additive dependent variable becomes as important as the original dependent variable during tree growth because some additional variables may be employed to build the regression of the additive dependent variable. Moreover, because of the low cardinality (i.e., 1 and 0) of the additive dependent variable, there is only one option to split the additive dependent, thus impacting the gradient of homogeneity.

In the context of predictions of AIM/LMF indicators, this is a critical factor to keep in mind. For variables such as sagebrush height, we observe the lowest coefficients of variation and highest errors among the variables tested (Table 3). Some of the error in these predictions may be due to this problem, and methodological improvements are needed for managing this "null values" problem in the context of predicting certain landscape indicators.

6 Conclusions

In this study, we employed a machine learning-based regression model (i.e., random forest) to assimilate satellite remote sensing images (i.e., MODIS BRDF parameters, NBAR, and Landsat 8 OLI surface reflectance) and *in situ* measurements (i.e., AIM and LMF data collection) from four hundred selected ecoregions of the Western U.S. The field data collection used consistent methods and was performed by different teams or offices in different states, so the data are reproducible. Within these data, the predicted distribution maps of nineteen surface indicators, which are related to vegetation composition, vegetation structure, and bare ground cover, were created. The correlations between the model predicted values and *in situ* values of all surface indicators are strongly positive. The MODIS BRDF parameters product tends to contribute more to the regression than other predictors.

These results exhibit the potential for predicting, using optical imagery and ancillary data, the distribution of important dryland indicators using RF. However, there are caveats. First, predictions are strongest in areas that have *in situ* data. Care must be taken when extrapolating out of these areas. Second, this approach tends to under-predict at high values and over-predict at low values. The errors at high values generally contribute low relative error and may be within acceptable ranges for many applications. However, the high relative error is likely at low values, and care must be taken in cases with low values. Nonetheless, within these limits, this study shows how these relationships can be extended to produce spatially continuous datasets coupled with quantitative estimates of the error. Therefore, assimilating satellite remote sensing images and field data using machine learning methods can provide usable predictions of the surface indicators in drylands. There are many potential uses for such prediction maps that extend beyond the

management mandate for which the original *in situ* data were commissioned. For instance, predicted distribution maps from our study could be employed as inputs for climate models (particularly bare soil cover, which is a common variable in global and regional models, e.g., Xue and Shukla 1993) to forecast the potential for dust emission in the Western U.S.

References

Asner, G.P. (1998). Biophysical and biochemical sources of variability in canopy reflectance. *Remote Sensing of Environment, 64*, 234-253

Bestelmeyer, B.T., Okin, G.S., Duniway, M.C., Archer, S.R., Sayre, N.F., Williamson, J.C., & Herrick, J.E. (2015). Desertification, land use, and the transformation of global drylands. *Frontiers in Ecology and the Environment, 13*, 28-36

Booth, D.T., & Cox, S.E. (2009). Dual-camera, high-resolution aerial assessment of pipeline revegetation. *Environmental Monitoring and Assessment, 158*, 23-33

Breiman, L. (1996). Bagging predictors. *Machine learning, 24*, 123-140

Breiman, L. (2001). Random forests. *Machine learning, 45*, 5-32

Breiman, L., Friedman, J., Stone, C.J., & Olshen, R.A. (1984). *Classification and regression trees*. CRC press

Chipman, H.A., George, E.I., & McCulloch, R.E. (2010). BART: Bayesian additive regression trees. *The Annals of Applied Statistics, 4*, 266-298

Dietterich, T.G. (2000). An experimental comparison of three methods for constructing ensembles of decision trees: Bagging, boosting, and randomization. *Machine learning, 40*, 139-157

Duniway, M.C., Karl, J.W., Schrader, S., Baquera, N., & Herrick, J.E. (2012). Rangeland and pasture monitoring: an approach to interpretation of high-resolution imagery focused on observer calibration for repeatability. *Environmental Monitoring and Assessment, 184*, 3789-3804

Elzinga, C.L., Salzer, D.W., & Willoughby, J.W. (1998). *Measuring & Monitering Plant Populations*. CreateSpace Independent Publishing Platform

Friedl, M.A., & Brodley, C.E. (1997). Decision tree classification of land cover from remotely

sensed data. *Remote Sensing of Environment, 61*, 399-409

Fujisada, H., Bailey, G.B., Kelly, G.G., Hara, S., & Abrams, M.J. (2005). ASTER DEM performance. *Ieee Transactions on Geoscience and Remote Sensing, 43*, 2707-2714

Hafez, A., Soliman, A., El-Metwally, K., & Ismail, I. (2017). Tilt and azimuth angles in solar energy applications–A review. *Renewable and Sustainable Energy Reviews, 77*, 147-168

Herrick, J.E., Lessard, V.C., Spaeth, K.E., Shaver, P.L., Dayton, R.S., Pyke, D.A., Jolley, L., & Goebel, J.J. (2010). National ecosystem assessments supported by scientific and local knowledge. *Frontiers in Ecology and the Environment, 8*, 403-408

Herrick, J.E., Van Zee, J.W., Havstad, K.M., Burkett, L.M., Whitford, W.G., Bestelmeyer, B.T., Melgoza, A., Pellant, M., Pyke, D.A., & Remmenga, M.D. (2017). Monitoring manual for grassland, shrubland and savanna ecosystems. Volume I: Core Methods. In: USDA ARS Las Cruces, New Mexico. The University of Arizona Press

Holthausen, R., Czaplewski, R.L., DeLorenzo, D., Hayward, G., Kessler, W.B., Manley, P., McKelvey, K.S., Powell, D.S., Ruggiero, L.F., & Schwartz, M.K. (2005). *Strategies for monitoring terrestrial animals and habitats*.

Huete, A., Didan, K., Miura, T., Rodriguez, E.P., Gao, X., & Ferreira, L.G. (2002). Overview of the radiometric and biophysical performance of the MODIS vegetation indices. *Remote Sensing of Environment, 83*, 195-213

James, G., Witten, D., Hastie, T., & Tibshirani, R. (2013). *An introduction to statistical learning*. Springer

Jones, M.O., Allred, B.W., Naugle, D.E., Maestas, J.D., Donnelly, P., Metz, L.J., Karl, J., Smith, R., Bestelmeyer, B., & Boyd, C. (2018). Innovation in rangeland monitoring: annual, 30 m, plant functional type percent cover maps for US rangelands, 1984–2017. *Ecosphere, 9*, e02430

Karl, J.W., Duniway, M.C., & Schrader, T.S. (2012). A Technique for Estimating Rangeland Canopy-Gap Size Distributions From High-Resolution Digital Imagery. *Rangeland Ecology & Management, 65*, 196-207

Karl, J.W., Taylor, J., & Bobo, M. (2014). A double-sampling approach to deriving training and validation data for remotely-sensed vegetation products. *International Journal of Remote Sensing, 35*, 1936-1955

Knippertz, P., & Stuut, J.-B.W. (2014). *Mineral dust : a key player in the earth system.* Springer

Kruckeberg, A.R. (2006). *Introduction to California soils and plants: serpentine, vernal pools, and other geobotanical wonders*. University of California Press Berkeley

Kuhn, M., & Johnson, K. (2013). *Applied predictive modeling*. Springer

Laliberte, A.S., Rango, A., Havstad, K.M., Paris, J.F., Beck, R.F., McNeely, R., & Gonzalez, A.L. (2004). Object-oriented image analysis for mapping shrub encroachment from 1937 to 2003 in southern New Mexico. *Remote Sensing of Environment, 93*, 198-210

Lary, D.J. (2010). *Artificial intelligence in geoscience and remote sensing*. INTECH Open Access Publisher

Lary, D.J., Alavi, A.H., Gandomi, A.H., & Walker, A.L. (2016). Machine learning in geosciences and remote sensing. *Geoscience Frontiers, 7*, 3-10

Leenaars, J.G., Wheeler, I., Wright, M.N., Batjes, N.H., Bauer-Marschallinger, B., Blagotić, A., Mantel, S., Heuvelink, G., Mendes de Jesus, J., & Guevara, M.A. (2017). SoilGrids250m: Global gridded soil information based on machine learning

Li, X.W., & Strahler, A.H. (1986). Geometric-Optical Bidirectional Reflectance Modeling of a Conifer Forest Canopy. *Ieee Transactions on Geoscience and Remote Sensing, 24*, 906-919

Liang, S., Li, X., & Wang, J. (2012). *Advanced remote sensing: terrestrial information extraction*

and applications. Academic Press

Liaw, A., & Wiener, M. (2002). Classification and regression by randomForest. *R news, 2*, 18-22

Loveland, T., Merchant, J., Brown, J., & Ohlen, D. (1991). Development of a land-cover characteristics database for the conterminous U. S. *Photogrammetric Engineering and Remote Sensing, 57*, 1453-1463

Ludwig, J.A., Bastin, G.N., Chewings, V.H., Eager, R.W., & Liedloff, A.C. (2007). Leakiness: a new index for monitoring the health of arid and semiarid landscapes using remotely sensed vegetation cover and elevation data. *Ecological Indicators, 7*, 442-454

Luscier, J.D., Thompson, W.L., Wilson, J.M., Gorham, B.E., & Dragut, L.D. (2006). Using digital photographs and object-based image analysis to estimate percent ground cover in vegetation plots. *Frontiers in Ecology and the Environment, 4*, 408-413

MacKinnon, W.C., Karl, J.W., Toevs, G.R., Taylor, J.J., Karl, S., Spurrier, C.S., & Herrick, J.E. (2011). *BLM core terrestrial indicators and methods*. US Department of the Interior, Bureau of Land Management, National Operations Center Denver

Maclaurin, G., Sengupta, M., Xie, Y., & Gilroy, N. (2016). Development of a MODIS-Derived Surface Albedo Data Set: An Improved Model Input for Processing the NSRDB. In: National Renewable Energy Lab (NREL)

Marsett, R.C., Qi, J., Heilman, P., Biedenbender, S.H., Watson, M.C., Amer, S., Weltz, M., Goodrich, D., & Marsett, R. (2006). Remote sensing for grassland management in the arid southwest. *Rangeland Ecology & Management, 59*, 530-540

McCord, S.E., Buenemann, M., Karl, J.W., Browning, D.M., & Hadley, B.C. (2017). Integrating Remotely Sensed Imagery and Existing Multiscale Field Data to Derive Rangeland Indicators: Application of Bayesian Additive Regression Trees. *Rangeland Ecology & Management, 70*,

644-655

McMahon, G., Gregonis, S.M., Waltman, S.W., Omernik, J.M., Thorson, T.D., Freeouf, J.A.,

Rorick, A.H., & Keys, J.E. (2001). Developing a spatial framework of common ecological

regions for the conterminous United States. *Environmental Management, 28*, 293-316

Miller, D.A., & White, R.A. (1998). A conterminous United States multilayer soil characteristics

dataset for regional climate and hydrology modeling. *Earth interactions, 2*, 1-26

Murphy, K.P. (2012). *Machine learning: a probabilistic perspective*. MIT press

Okin, G.S., Parsons, A.J., Wainwright, J., Herrick, J.E., Bestelmeyer, B.T., Peters, D.C., &

Fredrickson, E.L. (2009). Do Changes in Connectivity Explain Desertification? *Bioscience, 59*,

237-244

Pal, M. (2005). Random forest classifier for remote sensing classification. *International Journal*

of Remote Sensing, 26, 217-222

Pedregosa, F., Varoquaux, G., Gramfort, A., Michel, V., Thirion, B., Grisel, O., Blondel, M.,

Prettenhofer, P., Weiss, R., & Dubourg, V. (2011). Scikit-learn: Machine learning in Python.

Journal of Machine Learning Research, 12, 2825-2830

Ramcharan, A., Hengl, T., Nauman, T., Brungard, C., Waltman, S., Wills, S., & Thompson, J.

(2018). Soil property and class maps of the conterminous United States at 100-meter spatial

resolution. *Soil Science Society of America Journal, 82*, 186-201

Roberts, D.R., Bahn, V., Ciuti, S., Boyce, M.S., Elith, J., Guillera-Arroita, G., Hauenstein, S.,

Lahoz-Monfort, J.J., Schröder, B., & Thuiller, W. (2017). Cross-validation strategies for data

with temporal, spatial, hierarchical, or phylogenetic structure. *Ecography, 40*, 913-929

Rodriguez-Galiano, V.F., Ghimire, B., Rogan, J., Chica-Olmo, M., & Rigol-Sanchez, J.P. (2012).

An assessment of the effectiveness of a random forest classifier for land-cover classification.

Isprs Journal of Photogrammetry and Remote Sensing, 67, 93-104

Roujean, J.L., Leroy, M., & Deschamps, P.Y. (1992). A Bidirectional Reflectance Model of the Earths Surface for the Correction of Remote-Sensing Data. *Journal of Geophysical Research-Atmospheres, 97*, 20455-20468

Roy, D.P., Wulder, M., Loveland, T.R., Woodcock, C., Allen, R., Anderson, M., Helder, D., Irons, J., Johnson, D., & Kennedy, R. (2014). Landsat-8: Science and product vision for terrestrial global change research. *Remote Sensing of Environment, 145*, 154-172

Russell, S., & Norvig, P. (2011). Artificial Intelligence A Modern Approach 3rd Edition Pdf. *Hong Kong: Pearson Education Asia*

Schaaf, C.B., Gao, F., Strahler, A.H., Lucht, W., Li, X.W., Tsang, T., Strugnell, N.C., Zhang, X.Y., Jin, Y.F., Muller, J.P., Lewis, P., Barnsley, M., Hobson, P., Disney, M., Roberts, G., Dunderdale, M., Doll, C., d'Entremont, R.P., Hu, B.X., Liang, S.L., Privette, J.L., & Roy, D. (2002). First operational BRDF, albedo nadir reflectance products from MODIS. *Remote Sensing of Environment, 83*, 135-148

Segal, M.R. (2004). Machine learning benchmarks and random forest regression

Smith, J. (1977). Vegetation and microclimate of east-and west-facing slopes in the grasslands of Mt Wilhelm, Papua New Guinea. *The Journal of Ecology*, 39-53

Steinberg, D., & Colla, P. (2009). *CART: classification and regression trees*. Springer

Strahler, A.H., Muller, J., Lucht, W., Schaaf, C., Tsang, T., Gao, F., Li, X., Lewis, P., & Barnsley, M.J. (1999). MODIS BRDF/albedo product: algorithm theoretical basis document version 5.0. In: NASA

Sun, W., Liang, S., Xu, G., Fang, H., & Dickinson, R. (2008). Mapping plant functional types from MODIS data using multisource evidential reasoning. *Remote Sensing of Environment, 112*,

1010-1024

Svetnik, V., Liaw, A., Tong, C., Culberson, J.C., Sheridan, R.P., & Feuston, B.P. (2003). Random forest: a classification and regression tool for compound classification and QSAR modeling. *Journal of chemical information and computer sciences, 43*, 1947-1958

Westerling, A.L., Hidalgo, H.G., Cayan, D.R., & Swetnam, T.W. (2006). Warming and earlier spring increase western US forest wildfire activity. *Science, 313*, 940-943

Xue, Y., & Shukla, J. (1993). The influence of land surface properties on Sahel climate. Part 1: Desertification. *Journal of Climate, 6*, 2232-2245

Zhang, J., Zhu, W., Dong, Y., Jiang, N., & Pan, Y. (2013). A spectral similarity measure based on Changing-Weight Combination Method. *Acta Geodaetica et Cartographica Sinica, 42*, 418-424

Zhang, J., Zhu, W., Wang, L., & Jiang, N. (2012). Evaluation of similarity measure methods for hyperspectral remote sensing data. In, *Geoscience and Remote Sensing Symposium (IGARSS), 2012 IEEE International* (pp. 4138-4141): IEEE

Chapter 3 A coupled ecological model with an aeolian transport component to simulate the evolution of vegetation pattern impacted by wind erosion in drylands

Abstract: Drylands cover more than 40% of the land surface of the Earth and are characterized by patchy vegetation and that permits erosion of the surface. Vegetation-aeolian transport is an important feedback in drylands, particularly those undergoing shrub encroachment. Although one side of the feedback, the loss of grasses following the increase of aeolian transport, has been well studied, the other, the influence of aeolian transport on existing vegetation, has been never studied in detail. In this study, a new ecological-wind erosion model (ECO-WEMO) that contains an aeolian transport component was created to simulate how aeolian transport impacts vegetation pattern and causes the state change. Three modeling scenarios were investigated: 1) stable grass and shrub communities without aeolian transport, 2) shrub and grass communities with aeolian transport, and 3) shrub and grass communities with aeolian transport and drought. Our results confirm, in a modeling context, the important role that aeolian transport can play in state change in deserts. In the future, the model might be used to investigate specific scenarios of shrub encroachment to identify the role of aeolian transport in initiating and stabilizing shrub encroachment. Ongoing field experiments may also be used to improve the model parameterizations so that realistic, landscape-scale simulations can be done, to help predict the future of landscapes undergoing change.

1 Introduction

Aeolian transport refers to the processes of the transport of soil particles by wind. Aeolian transport and the associated dust emission have significant implications on Earth's atmospheric, hydrologic,

and biogeochemical cycles (Gautam et al. 2013; Ginoux 2003; Kok 2011; Laurent et al. 2008; Nousiainen et al. 2009; Okin 2005; Pye 2015). Vegetation cover and structure strongly modulate patterns of wind-driven transport in drylands; however, the interactions between vegetation and aeolian transport are complex and vary across the different spatial scales (Alvarez et al. 2011; Ravi et al. 2010; Shao et al. 2015). Thus, dynamics in the composition of the plant community and species dominance can results in the altering of soil erosion and the loss of soil resources in dust by blowing and flushing away soil particles, thus contributing to desertification (Okin et al. 2009b; Alvarez et al. 2011; Ravi et al. 2010). For example, many arid and semiarid rangelands have been undergoing shrub encroachment. This state change consists of an increase in shrub cover with a related reduction of grass cover, leading to an increase in the erodible gap size (Turnbull et al. 2012). An abrupt and apparently irreversible state change such as this needs two factors: one is a feedback, which can generate the alternative stable state; other is a driver, which can trigger a dynamics from the stable state to the other (Okin et al. 2009a). One positive feedback that has been suggested are the interactions between vegetation and aeolian transport, whereby the loss of grass cover is followed by the increasing aeolian transport, which, in turn, decreases grass cover and promotes shrub dominance (D'Odorico et al. 2012). One side of this aeolian-vegetation feedback, the influence of vegetation loss on aeolian transport, has been well studied (Li et al. 2007; Li et al. 2008; Okin et al. 2009a; Okin et al. 2009b). The other, the influence of aeolian transport on existing vegetation, has never been studied in detail. Moreover, although the wind has a strong impact on the pattern of vegetation and the geomorphology of the landscape (Li et al. 2009), the study of wind as the driver of the state change is less well established.

Models are potentially important tools for examining vegetation-aeolian transport interactions. A simplistic model of vegetation dynamics and erosion has been used to explain state change in drylands (Okin et al. 2009a). A model based on connectivity theory was created to capture vegetation dynamics as influenced by the transport of wind and water (Stewart et al. 2014). A coupled vegetation-sediment transport model has been developed to explain the impact of wind erosion on the evolution of nebkhas in drylands (Mayaud et al. 2017). A geomorphic model has been used to simulate sand dune formation as influenced by vegetation growth (Nield and Baas 2008). Although several models designed to simulate the interactions between vegetation and aeolian transport (D'Odorico et al. 2012), relatively few focuses on the influence of aeolian transport on existing vegetation, which leads to state change. Individual-based models that included complex biotic competition interactions are absent from all of these models.

In order to address the interacting roles of biotic competition and aeolian transport, a new integrated ecological model (ECO-WEMO) was implemented and tested in this study. This new model was created by coupling with an existing individual-based ecological model with an aeolian transport model. The individual-based, gap dynamics simulation model (ECOTONE) was developed to simulate vegetation dynamics at transition zones between communities dominated by herbaceous and woody species in arid and semiarid rangelands (Peters 2002). This model includes the competition between different plants by several biotic and abiotic factors and imitates seed dispersal, germination establishment, competition, mortality, and growth of each plant. This model has successfully simulated the interaction between *Larrea tridentata* and *Bouteloua eriopoda* at Jornada Basin (Rastetter et al. 2003). A more recent gap-controlled physically-based aeolian transport model, Okin's aeolian transport model (WEMO), was coupled into this model

(Okin 2008). WEMO model uses a size distribution of erodible gaps between plants, instead of lateral cover, to describe the distribution of shear stress at the surface. This model has two advantages compared with traditional models such as that of Raupach model (Raupach et al. 1993). First, it models partitions of shear stress for vegetated surface, using a continuous function to describe shear stress in the lee side of the plant, instead of assuming zero shear stress in plant wakes. Second, the primary input variables of this model are vegetation cover, erodible gap size, and plant height, which can be obtained using standard field methods (Herrick et al. 2017) or an orthophotography technique (Chapter 1). Based on the researches of Vest et al. (2013), Lancaster et al. (2010), Li et al. (2013), and Mayaud et al. (2017), WEMO model performed better than the traditional model at a landscape scale (1-100 m), particularly in cases with relatively high vegetation cover.

In this study, we present a new integrated ecological model (ECO-WEMO), which couples ECOTONE with WEMO, to examine the influence of aeolian transport on existing vegetation at a landscape scale. Model runs are used to elucidate the interacting roles of plant competitive advantage, aeolian transport, and drought.

2 Model Description

2.1 Site Description

The parameters of this model are inherited from ECOTONE model, which was parameterized and verified for the arid and semiarid rangelands at the Sevilleta National Wildlife Refuge (SEV) in New Mexico, U.S. (Peters 2002). The dominant or codominant plants of this area are *Prosopis glandulosa* (honey mesquite, shrub), *Sporobolus cryptandrus* (sand dropseed, grass), and

Bouteloua eriopoda (black grama, grass). The inputs of this model include soil texture, climate, disturbance, and wind. The soil is divided into nine layers, with its own depth, soil texture, water content at field capacity, water content at wilting point, evaporation coefficient, and transpiration coefficient. Soil texture data was parameterized from SEV based on field measurements. Climate data, including daily air temperature and daily ground precipitation, were based on the weather station at SEV from 1918 to 1997. Four types of disturbances including abandoned field, ant nest, small animal burrow, and rat mound are allowed in the model. Wind data is derived from three anemometers recording at 5-minute intervals at a height of 15 m at the headquarters of the Jornada Experimental Range (JER), New Mexico.

2.2 Model Integration

The coupled model consists of two models that cooperate with each other through a coupler. One model is the gap-based vegetation dynamics model (module A, C, and D adapted from ECOTONE, Figure 1) to simulate seed dispersal, germination establishment, competition, mortality, and growth of plants in each cell. This model by transfers biomass variables, including aboveground perennial biomass (PBIOML), belowground perennial biomass (PBIOMR), aboveground annual growth biomass (ABIOML), and belowground annual growth biomass (ABIOMR) and the other model is the aeolian transport model (module B adapted from WEMO, Figure 1). This model calculates and passes back horizontal flux and net surface height change based on the vegetation biomass and vegetation distribution in several cells. In this study, since only an 80-year historical weather data record is available, the weather data were recycled in the simulation. Although this model could be used to test the relationship between wind strength and vegetation change, the focus of this study is to simulate state change caused by aeolian transport and competition. Thus,

we assume that, after a spin-up with no wind, the distribution of wind speed of each year of the simulation is constant thereafter.
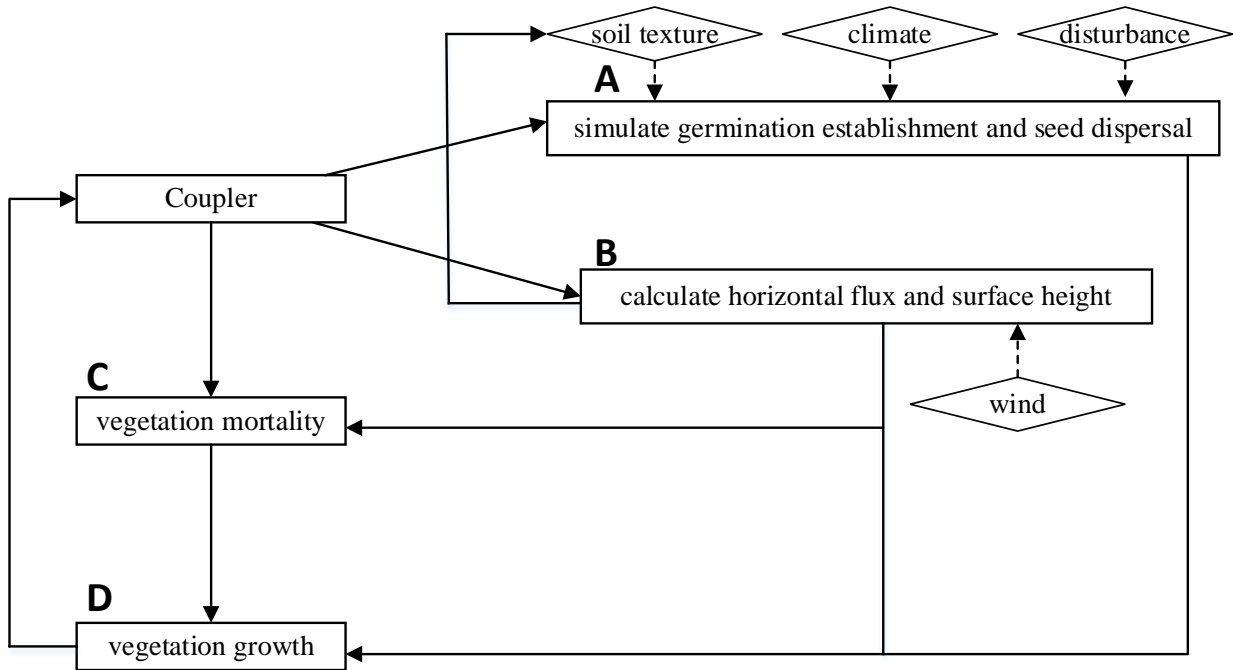

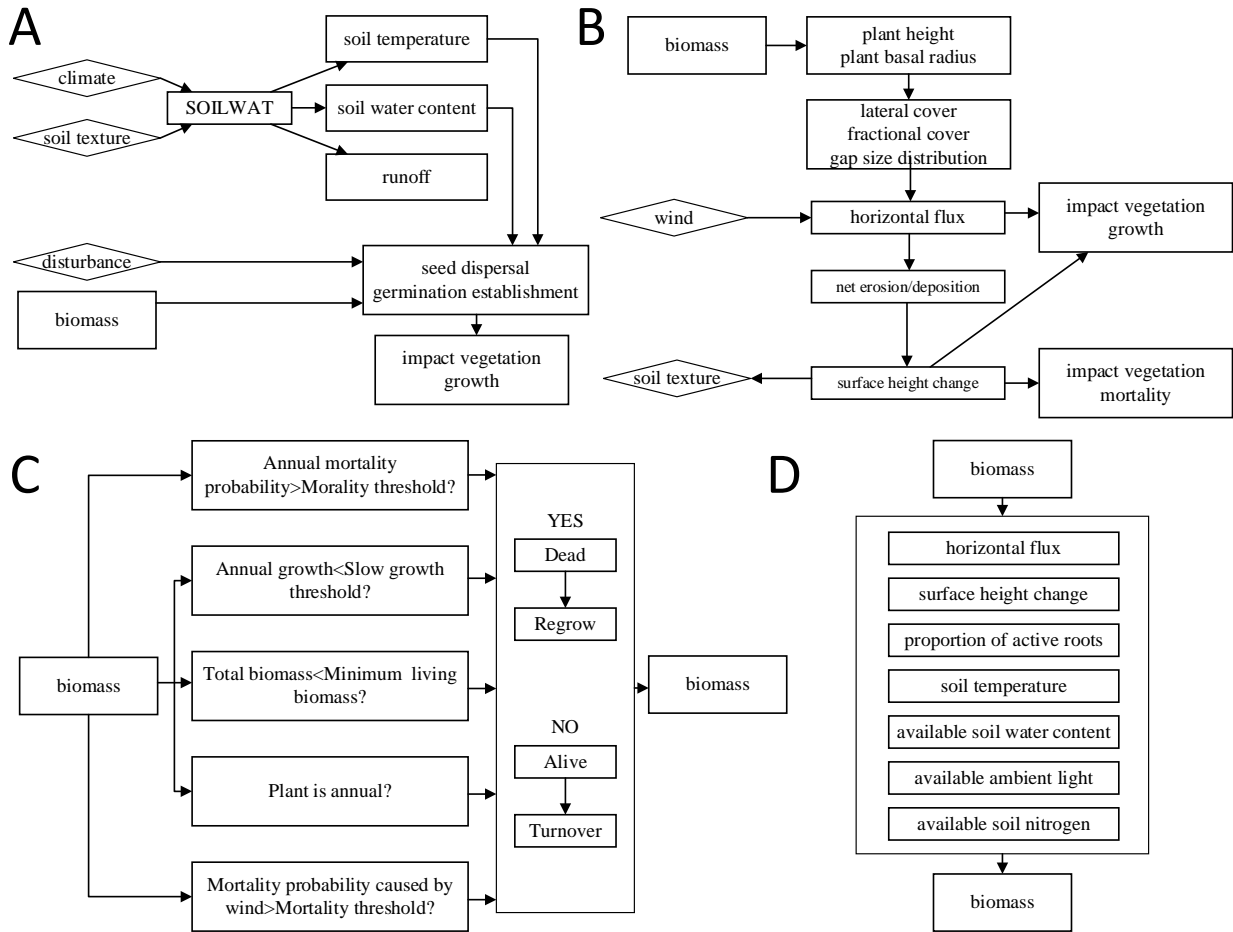Figure 1 General flow of the coupled model.

Figure 2 Flow diagrams of modules: A. module of seed dispersal and germination establishment, B. module of aeolian transport, C. module of vegetation mortality and competition, and D. module of vegetation growth.

Module A (Figure 2A) aims to simulate seed dispersal and germination establishment, which mainly impact vegetation growth. The SOILWAT model provides soil water content and soil temperature based on climate and soil texture; the details can be found in Parton et al. (1988). However, seed dispersal and germination establishment also rely on PBIOML and PBIOMR because each plant needs to have enough biomass to produce seeds. Based on the original ECOTONE model, although small disturbances cannot kill a mature plant, those do impact the germination and establishment. Four major disturbances (abandoned field, ant nests, small animal

burrows, and rat mounds) are included in this module and are randomly distributed in the model grid in each year.

Module B (Figure 2B) aims to simulate horizontal flux and net surface height change caused by aeolian transport. In order to couple this aeolian transport module, the aboveground biomass of plant is converted to plant height (h) and plant basal radius (r) to estimate the vertical structure of vegetation. Shrubs were considered as cylinders with $r/h=1/2$, whereas grasses were considered to be cones with $r/h=1/2$. The conversions from biomass to plant height and plant basal radius are thus given by:

$$r_{shrub} = \sqrt[3]{\frac{M}{2\pi\rho}},\tag{1}$$

$$r_{grass} = \sqrt[3]{\frac{M}{0.67\pi\rho}},\tag{2}$$

$$h = 2r,\tag{3}$$

where M represents the total aboveground perennial biomass (PBIOML) of a species that has the largest plant in one cell and ρ represents the bulk density of plant (200 g/m^3). Here, for the purposes of aeolian transport, we define an empty cell as a cell in which the basal radius of the largest plant does not exceed 5% of the area of the cell ($r \approx 12$ cm). The aeolian transport module also computes fractional cover (c) and non-gap length (w) of each cell:

$$c = \frac{(\pi r^2)}{s},\tag{4}$$

$$w = \frac{\pi r}{2},\tag{5}$$

where s represents the cell size (1 m $\times$ 1 m in this study).

Aeolian transport is affected by relatively large-scale features of the land surface (Shao et al. 2015). The vegetation modules (Module C and D) do not specify where the plants are in a cell, so plants are considered to be randomly located within a cell. This allows us to assume that, on the scale of several cells, the probability ($P_d(x)$) that any point within those cells is a distance (x) from the nearest upwind plant, can be defined by an exponential distribution (Okin 2008). In practice, we used a 5 x 5 moving window to calculate variables for each timestep (one year), needed to estimate $P_d(x)$ and horizontal flux (Q).

Mean values from moving windows are assigned to the center cell (i,j) where i ($i = 1 \dots I$) and j ($j = 1 \dots J$) such that I and J are numbers of cells in the direction parallel and perpendicular to the wind direction, respectively. The mean value of non-gap length and plant height ($\overline{W}_{i,j}$ and $\overline{H}_{i,j}$, repectively) were calculated including only values for non-empty cells, whereas cover ($\overline{C}_{i,j}$) was estimated using all cells in the window:

$$\overline{C}_{i,j} = \frac{\sum c_{i-n:i+n, j-n:j+n}}{(2n+1)^2}, \tag{6}$$

$$\overline{W}_{i,j} = \frac{\sum w_{i-n:i+n, j-n:j+n}}{N}, \tag{7}$$

$$\overline{H}_{i,j} = \frac{\sum h_{i-n:i+n, j-n:j+n}}{N}, \tag{8}$$

where n is the distance, in cells, that the moving window extends past cell (i,j), N is the number of non-empty cells. The mean gap length within the window is given by Okin (2008):

$$\overline{L}_{i,j} = \overline{W}_{i,j} \left(\frac{1-\overline{C}_{i,j}}{\overline{C}_{i,j}} \right). \tag{9}$$

In order to conserve overall mass in the simulations, periodic boundary conditions are applied in both directions (parallel and perpendicular to the wind, i and j, respectively).

There are two outputs of aeolian transport module: horizontal flux (Q) and net surface height change (D). The first step of calculating horizontal flux is to convert a wind speed at a certain height to a wind shear velocity at the surface. Using law of the wall (Lopez 1998), the surface shear velocity (u_*) in the absence of plants is given by:

$$u_* = K \times \frac{u}{\log(\frac{z_{height}}{z_o})},$$ (10)

where z_{height} is the height that wind speed was measured (1500 cm in this study), z_o is the roughness length, K is von Karman's constant (0.4), and u is the wind speed at the measured height. Li et al. (2013) determined that, for the purposes of WEMO, the best value of z_o in this context is 7.9 cm. In the WEMO model, each plant has associated with it a zone of reduced shear stress. The ratio of the surface shear velocity in this area to the surface shear velocity in the absence of plants ($\frac{u_{*S}}{u_*}$) is calculated as:

$$\frac{u_{*S}}{u_*} = \frac{u_{*S}}{u_*}_{x=0} + (1 - \frac{u_{*S}}{u_*}_{x=0}) \times (1 - \exp(-\frac{c}{x})),$$ (11)

where $\frac{u_{*S}}{u_*}_{x=0}$ is the ratio of at zone with zero surface shear stress, x is the gap length expressed in units of plant height, and c is the e-folding distance for the recovery of the shear stress in the unit of plant height. Based on the results of Li et al. (2013), the best-fit estimate for c is 5.6 and for $\frac{u_{*S}}{u_*}_{x=0}$ is 0.29. Horizontal flux (Q_x^{u*}) at a certain point (x) in the shear stress wake zone is calculated using the relationship of Gillette and Chen (2001):

$$Q_x^{u*} = A \times \frac{\rho}{g} \times u_{*S} \times (u_{*S}^2 - u_{*t}^2),$$ (12)

90

where A is a constant, which is 0.026 (Li et al, 2013), ρ is the density of air (0.00129 g/cm^3), g is the acceleration due to gravity (980 cm/s^2), and u_{*t} is the threshold wind shear velocity of the unvegetated soil, which is taken as 25 cm/s, a reasonable value for a fine sandy soil (Marticorena and Bergametti 1995). The probability that any point in the reduced shear stress weak zone at a certain distance from the nearest upwind plant $P_d(x, \bar{L}_{i,j}/\bar{H}_{i,j})$ is expressed as an exponential function based on the research by McGlynn and Okin (2006) with e-folding length given by the mean scaled gap size ($\bar{L}_{i,j}/\bar{H}_{i,j}$):

$$P_d(x, \bar{L}_{i,j}/\bar{H}_{i,j}) = \exp\left(-\frac{x}{\bar{L}_{i,j}/\bar{H}_{i,j}}\right)/(\bar{L}_{i,j}/\bar{H}_{i,j}), \tag{13}$$

Thus, in our simulations, to calculate the horizontal flux, $(Q_t^{u*})_{i,j}$, for the center cell (i, j) of a 5 × 5 window given a specific wind shear velocity (u_*), Q_x^{u*} is summed for all x weighted by the probability given the mean scaled gap size calculated for that window ($\bar{L}_{i,j}/\bar{H}_{i,j}$):

$$(Q_t^{u*})_{i,j} = (1 - \bar{C}_{i,j}) \sum_x P_d(x, \bar{L}_{i,j}/\bar{H}_{i,j}) Q_x^{u*}, \tag{14}$$

where $(1 - \bar{C}_{i,j})$ represents the erodible portion of the window, its bare soil area. To calculate the annual total horizontal flux $(Q_{i,j})$ for the cell centered on (i, j), an average of $(Q_t^{u*})_{i,j}$ is calculated, with each value weighted by the probability distribution of wind shear velocity, P_{u*}:

$$Q_{i,j} = \sum_{u*} P_{u*}(Q_t^{u*})_{i,j}, \tag{15}$$

In our model, P_{u*} is a constant distribution for every year after a model spin-up, and is derived from a three-year (2006-2008) record of wind speed measured at 5-minute intervals (Figure 3).

The net surface height change $D_{i,j}$ of each cell is defined by the difference of horizontal flux between a cell and its upwind neighbor:

$$D_{i,j} = (Q_{i,j} - Q_{i-1,j})/(\rho_{sand} \times S), \qquad (16)$$

where ρ_{sand} is 1.25 g/cm^3, a reasonable value for loose, wind erodible sandy soils (Brady and Weil 2008). D impacts both vegetation growth and mortality by root exposure or stem burial, as discussed in the following sections.
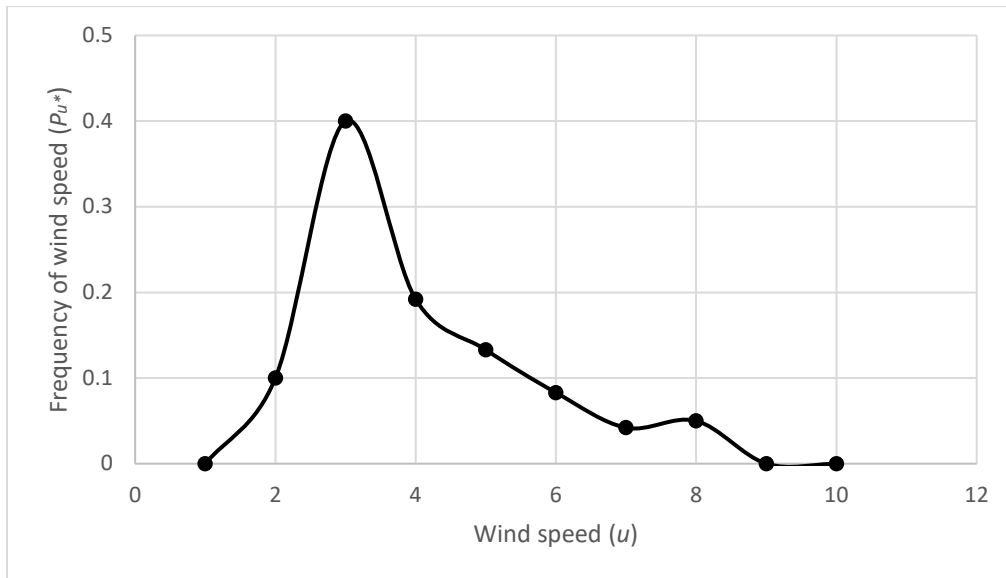

Figure 3 The probability distribution of the wind speed (u) measured at the headquarters of JER.

Module C simulates competition and mortality of plants in each cell. Plant mortality is mainly caused by four methods based on the original ECOTONE model (Peters 2002): annual mortality, slow growth, low biomass, and turnover of annual plants. Here, aeolian transport provides novel causes of plant mortality not in the original ECOTONE model through changes the surface height and plant abrasion. In the following, p_{mort}(plant) is defined as the probability of plant mortality for the different mortality methods, FUL_BIOMASS is the total of perennial and annual biomass, $(\cdot)_t$

is defined as the biomass at this time step, and $(\cdot)_{t-1}$ is defined as the biomass at the previous time step. Annual mortality is based on the study of Shugart (2000), where older perennial plant are less resistant to the short-term variations in environmental conditions. Each plant is assumed to have a probability of mortality related to age:

if $\text{plant}_{\text{age}} \leq \text{MAX} (\text{plant}_{\text{age}})/2$,

$$\text{then } p_{\text{mort}}(\text{plant})=0; \tag{17}$$

if $\text{plant}_{\text{age}} \geq \text{MAX} (\text{plant}_{\text{age}})$,

$$\text{then } p_{\text{mort}}(\text{plant})=1; \tag{18}$$

if $\text{plant}_{\text{age}} < \text{MAX} (\text{plant}_{\text{age}})$ and $\text{plant}_{\text{age}} > \text{MAX} (\text{plant}_{\text{age}})/2$,

$$\text{then } p_{\text{mort}}(\text{plant})= \frac{1}{MAX(\text{plant}_{age})/2} \times \text{plant}_{age} - 1. \tag{19}$$

Slow growth of a plant is assumed to lead to plant mortality because the plant is not only vulnerable to environmental conditions (drought) but also experiences short-term stresses (e.g., heavy rainfall, unusual freeze; Buffington and Herbel, 1965). For different species, the slow growth thresholds are different. The mortality of slow growth relies on the ratio of annual growth biomass to the previous perennial biomass such that:

if $\text{plant}_{(\text{ABIOMLt} + \text{ABIOMRt})} \leq \text{plant}_{(\text{PBIOMLt-1} + \text{PBIOMRt-1})} \times \text{threshold}_{\text{slow growth}}$,

$$\text{then } p_{\text{mort}}(\text{plant})=1; \tag{20}$$

if $\text{plant}_{(\text{ABIOMLt} + \text{ABIOMRt})} > \text{plant}_{(\text{PBIOMLt-1} + \text{PBIOMRt-1})} \times \text{threshold}_{\text{slow growth}}$,

$$\text{then } p_{\text{mort}}(\text{plant})=0. \tag{21}$$

The mortality due to low biomass is based on the study of Wright (1973). A plant needs to have enough perennial biomass of root and leaf to produce seeds and absorb sunlight, water, and nitrogen to survive. For different species, the minimum biomass thresholds are different with mortality dependent on the ratio of perennial biomass to the previous total biomass:

if $plant_{age} \geq 2$ and $plant_{(PBIOMLt+PBIOMRt)} \leq plant_{FUL\_BIOMASSt-1} \times threshold_{under\ minimum}$,

$$then\ p_{mort}(plant)=1; \tag{22}$$

if $plant_{age} \geq 2$ and $plant_{(PBIOMLt+PBIOMRt)} > plant_{FUL\_BIOMASSt-1} \times threshold_{under\ minimum}$,

$$then\ p_{mort}(plant)=0. \tag{23}$$

For annual plants, both aboveground and belowground biomass are converted to litter after one complete life cycle:

if $plant_{age} \geq 1$ and $MAX\ (plant_{age})=1$,

$$then\ p_{mort}(plant)=1; \tag{24}$$

if $plant_{age} \geq 1$ and $MAX\ (plant_{age}) \neq 1$,

$$then\ p_{mort}(plant)=0. \tag{25}$$

In this model, we added a new cause of plant mortality. Wind erosion/deposition causes net surface height change by adding and removing soil. Erosion may prevent plant roots from absorbing nitrogen and water from the soil, whereas deposition may prevent evapotranspiration and other energy exchange between plants and air. Based on the field data measured by Armbrust and Retta (2000), the mortality of a plant is an exponential function of the ratio of net surface height change and plant height. For different species, the net surface height change thresholds are different. The mortality of wind erosion due to net surface height change is given by:

if $plant_h \leq |D|$,

$$then \ p_{mort}(plant) = 1; \tag{26}$$

if $plant_h > |D|$,

$$then \ p_{mort}(plant) = e^{-threshold_D\left(\frac{D}{plant_h}\right)}. \tag{27}$$

Module D simulates the growth of plants in each cell. Plant growth depends on four abiotic factors including soil temperature, available soil water content, available ambient light, and available soil nitrogen and one biotic factor, which is the proportion of active roots. The details of plant growth could be found in Peters (2002). However, coupled with the aeolian transport module, root exposure/burial due to net surface height change impacts annual plant growth biomass (Cleugh et al. 1998) such that:

if $D < 0$ (root exposure),

$$then \ k_{ex} = |D|/(plant_h \times a) \ and \ plant_{ABIOMR} = plant_{ABIOMR} \times (1 - k_{ex}); \tag{28}$$

if $D \geq 0$ (root burial),

$$then \ k_{bu} = |D|/plant_h \ and \ plant_{ABIOML} = plant_{ABIOML} \times (1 - k_{bu}). \tag{29}$$

Aeolian transport also impacts vegetation through sandblasting (Okin et al. 2006). Based on the study of Armbrust and Retta (2000), the reduction of crop yield caused by the effect of sandblasting on the crop can be described by an exponential function such that:

if $Q > 0$,

$$\text{then plant}_{(\text{ABIOMR}+\ \text{ABIOML})} = \text{plant}_{(\text{ABIOMR}+\ \text{ABIOML})} \times \exp\left(-\frac{Q}{k_b}\right), \tag{30}$$

where k_b is a coefficient related to horizontal dust flux and ranged from 5-10.

In this study, we defined that the cell size to be 1 m $\times$ 1 m with a model timestep of 1 year. The total size of the model grid in this study is 30 m $\times$ 100 m (row and column) with the wind direction is aligned with the long dimension (Figure 4). At the beginning of a run, vegetation is randomly distributed in the model grid and one cell is allowed to have multiple plants which then compete according to the rules of the model. The model is written and implemented in the Fortran programming language (Intel Fortran 19.0).
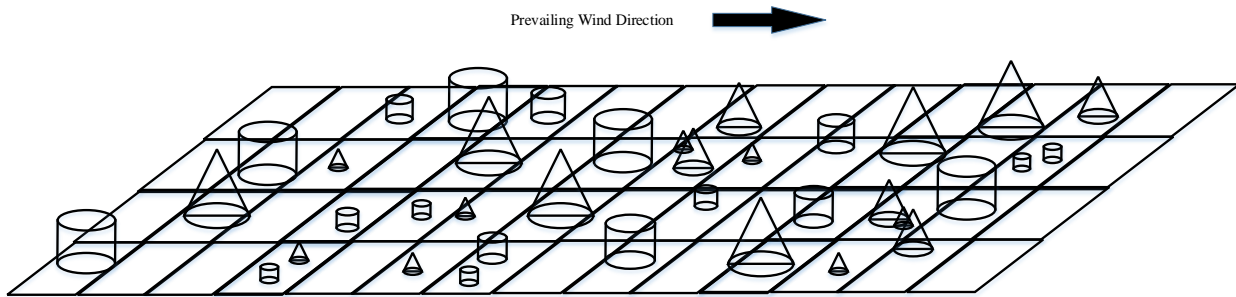
Figure 4 Schematic diagram of the model grid (cylinder represents shrub and cone represents grass; different size represents different biomass).

3 Experimental simulations

3.1 Model setup

In the following experiments, ECO-WEMO was used to simulate vegetation dynamics in runs with and without aeolian transport (Module B on or off). In all model simulations, a 10-year spin-up without any aeolian transport is allowed so that reasonable vegetation communities are in place before the effects of aeolian processes are included. This is, in part, due to the fact that ECOTONE

initiates models with zero biomass for all plants, which would lead extraordinarily and unrealistic high rates of aeolian transport, with the associated effects, at the beginning of the model runs.

For the experiments that did not simulate artificial drought, the climate data is based on historical weather data from SEV. For the experiments that include artificial drought, the climate data was manipulated based on the historical weather data such that drought begins in the 30th year of model simulation, once grass and shrub biomass are relatively stable. All combinations of droughts of 20%, 50%, and 80% precipitation reduction lasting 5, 10, 15, and 20 years were investigated. Two biophysical variables were changed to represent the competitive advantage of a species in the model simulations: intrinsic growth rate and full-grown aboveground and belowground biomass of a plant. In the case where shrubs have a competitive advantage, the shrub intrinsic growth rate was set to 0.67 with the full-grown aboveground and belowground biomass set to 108 g/m^2 and 216 g/m^2. The grass intrinsic growth rate was set to 0.5 with the full-grown aboveground and belowground biomass set to 54 g/m^2 and 108 g/m^2. In the case where grasses have a competitive advantage the grass intrinsic growth rate was set to 0.67 with full-grown aboveground and belowground biomass were set to 108 g/m^2 and 216 g/m^2. The shrub intrinsic growth rate was set to 0.5 with full-grown aboveground and belowground biomass were set to 108 g/m^2 and 216 g/m^2.

## 4 Results

4.1 Influence of wind

Model runs with and without wind were used to test the performance of the ECO-WEMO model (with wind) compared to ECOTONE alone (without wind). In the absence of wind, there is little difference between the model cases in which grass and shrub are in competitive advantage

compared to one another although the shrub-advantage case does exhibit slightly higher shrub biomass, particularly during dry periods (Figure 5). The first 10-years of the with-wind runs are identical to those of the without-wind runs because there was no wind allowed during this spin-up period. After the inclusion of wind, however, the shrub-advantage and grass-advantage cases are considerably different. The effect of wind in the shrub-advantage case is to, immediately after the end of the spin-up period, lead to a dramatic decrease in grass biomass and long-term dominance of shrubs in the simulations. Conversely, in the grass-advantage runs, shrub biomass decreases after the spin-up period, remaining lower than the grass biomass in the shrub-advantage runs. This behavior is due to the wind leading to the mortality of the plants which are smaller (grasses in the shrub-advantage case and shrubs in the grass-advantage case). The larger gaps in the shrub-advantage case lead to approximately twice the predicted horizontal flux as in the grass-advantage case, but are, in both cases between $2 - 6$ g cm^{-1} d^{-1}, consistent with field data measured by Gillette and Pitchford (2004) at the Jornada Experimental Range, which is where the wind data are from.
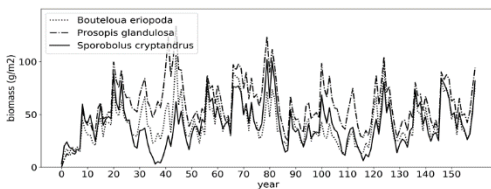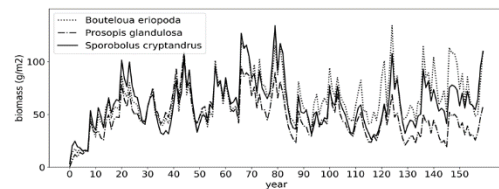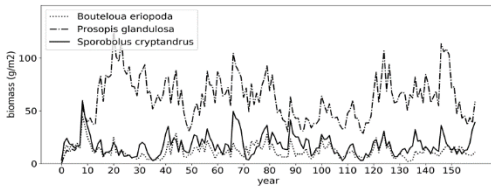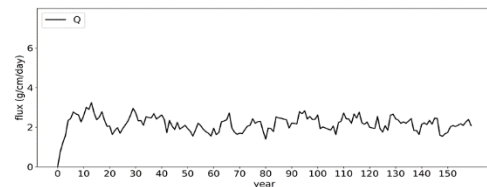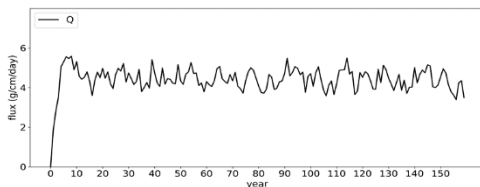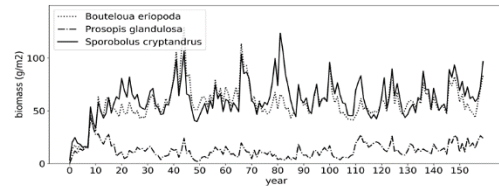
Figure 5 The annual mean biomass changes of shrub and grass included and excluded wind and the annual mean daily horizontal flux change of shrub-dominated and grass-dominated communities included wind.

4.2 Net surface height and vegetation patterns

Consistent with the temporal patterns, at the end of 100 years, patterns of dominant vegetation and biomass are largely similar between the shrub-advantage and grass-advantage cases in the absence of wind. In the shrub-advantage case, the range of biomass (i.e., the number of high-biomass and low-biomass cells) is greater than in the grass-advantage case, reflecting the larger size of individual shrubs compared to grasses (Figure 6). Thus, even though the average biomass in the two cases (without wind) is about the same (Figure 5), the distribution of this biomass is different depending on which functional type is in competitive advantage. In the shrub-advantage case, shrubs dominated about 50% of the cells, whereas in the grass-advantage case, grasses dominated about 60% of the cells (Figure 6).

In the presence of wind, there are considerable differences between the shrub-advantage and grass-advantage cases (Figure 6). Many more of the cells are filled with shrubs in the shrub-advantage case, with considerably higher variability in vegetation biomass, compared to the grass-advantage case. With wind, in the shrub-advantage case, shrubs dominated about 70% of the cells, whereas in the grass-advantage case, grasses dominated about 80% of the cells (Figure 6). The shrub-advantage case also contains more empty cells than the grass-advantage case. These empty cells contribute to larger gap size in the shrub-advantage case and therefore contribute to the higher overall predicted horizontal flux. Consistent with this the larger number of bare or low-cover cells in the shrub-advantage case, the net change in surface height in this case has a considerably higher range. Indeed, the predicted final topography at the end of 100 years has a total relief of several

meters, consistent with (but larger than) observed relief in shrub-dominated wind-erodible communities (e.g., Rango et al. 2000).
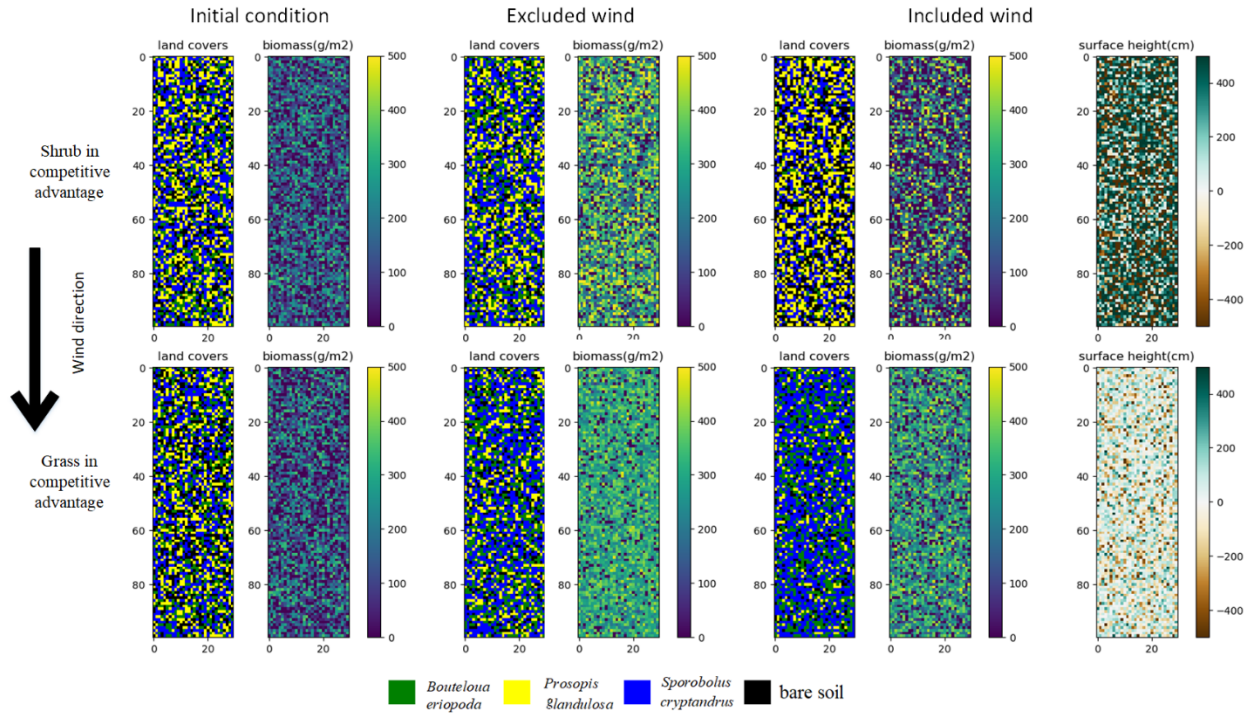
Figure 6 The spatial distribution maps of biomass and land cover with and without wind and the spatial distribution maps of net surface height change between the initial condition and final condition (initial condition was at the beginning of the spin-up period final condition was after 100 years).

4.3 Impact of drought

Two sets of drought experiments were run. In the first, the climate record used for the initial runs (Figure 5 and Figure 6) were modified, starting at year 30 of the simulations, by reducing precipitation for a certain time by a certain amount (5 and 10 years, reduced 20% and 50%). Deeper and longer droughts resulted in the mortality of so much vegetation that the model crashed. Therefore, the second set of drought runs was implemented, starting with higher precipitation (five

times that used to produce Figure 5 and Figure 6), but reducing the precipitation by larger amounts and for longer times.

In the first set of drought runs (Figure 7), using the 'normal' precipitation record, for the shrub-advantage runs without wind, drought leads to temporary mortality of grasses and overall shrub biomass dominance. The shorter droughts, whether 20% or 50% do not appear to show much difference. But shrub dominance is persistent for the 10-year, 20% drought case. Due to additional mortality of shrubs in the 10-year, 50% drought case, by the end of 80 years, shrub dominance has largely passed, but this is due to the reduced overall biomass of the shrubs, rather than the continued low biomass of grasses. For the grass-advantage drought runs without wind, there does not appear to be a significant influence on shrubs, and the communities remain mixed. In the drought cases with wind using the 'normal' precipitation record, the drought did not significantly impact the dominant species: shrubs remained dominant in shrub-advantage cases and grasses remained dominant in grass-advantage cases. However, overall biomass of shrubs (in the shrub-dominant case) and grasses (in the grass-dominant) case were lower than they were at the end of the runs without drought, and also lower than the runs without wind, indicating the combined effect of droughts and winds on community composition.

In experiments done with above-normal precipitation (Figure 8), even before the droughts at year 30, there is a considerable difference between runs with and without wind. Principally, grass biomass is about half the value of the no-wind case, even in the case where grasses have a

competitive advantage over shrubs. In the shrub-advantage case, the wind does not appear to have this effect on shrub biomass.

For the drought experiments starting with above normal precipitation, in the absence of wind, droughts did not impact the overall species dominance; shrubs remained dominant after drought in shrub-advantage cases and grasses remained dominant after drought in grass-dominant cases (Figure 7). With wind, in the shrub-advantage case, drought had little impact on the final grass or shrub biomass, except in the case of the most profound droughts, e.g. 80% for more than 15 years, when extreme drought led to the overall reduced biomass of shrubs. In the grass-advantage case, the most extreme droughts, on the other hand, led to a reversal of dominance of grasses and shrubs with, for example, shrub biomass being greater than grass biomass for a 15-year 50% drought.

Figure 7 The impact of drought with and without wind, in cases where shrubs have competitive advantage (left) and where grasses have competitive advantage (right). All runs had a 10-year period without wind for spin up. The droughts started in year 30 of the runs. Drought is represented by the percent reduction of precipitation from normal during the drought.

Grass in competitive advantage

Grass in competitive advantage

Shrub in competitive advantage

Shrub in competitive advantage
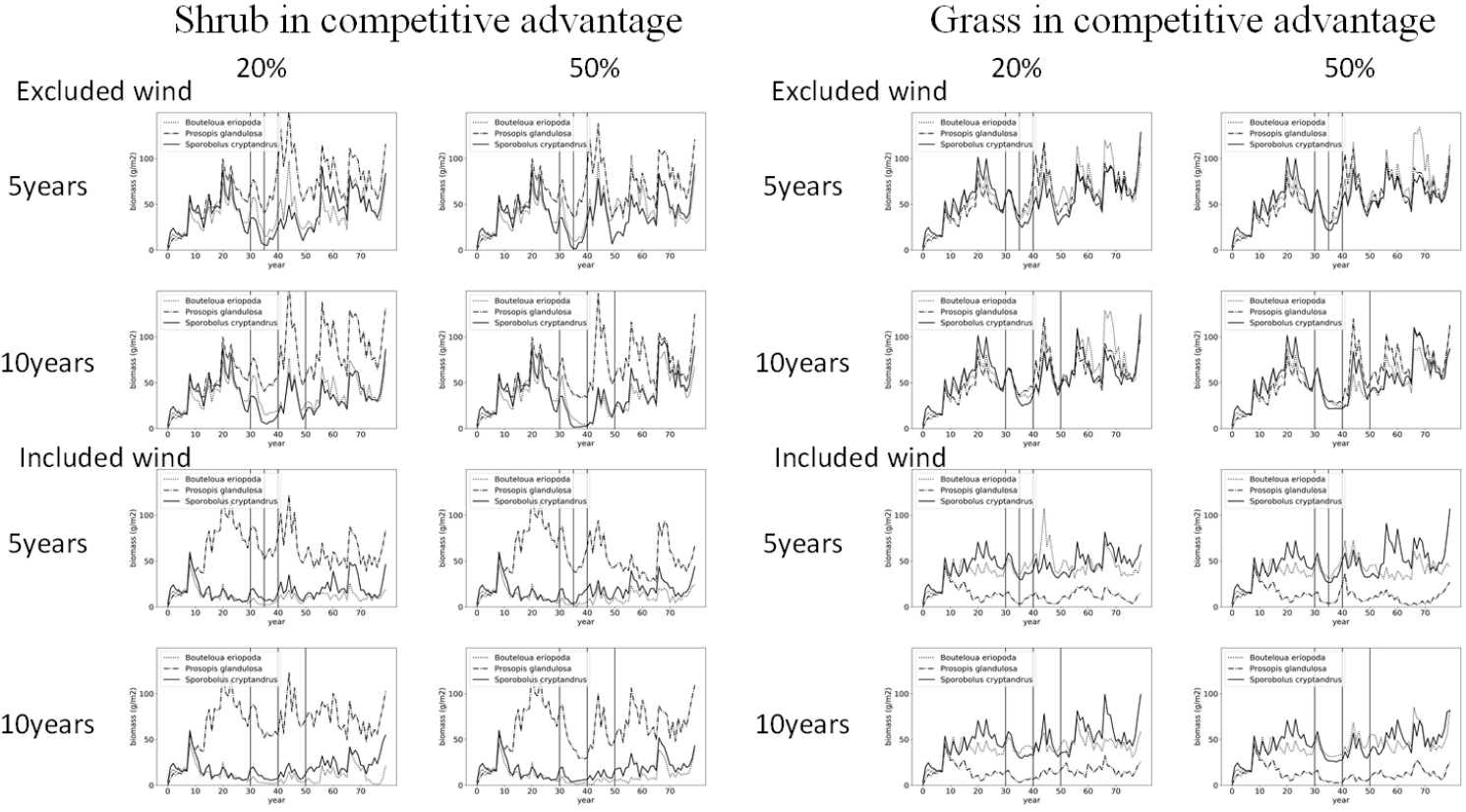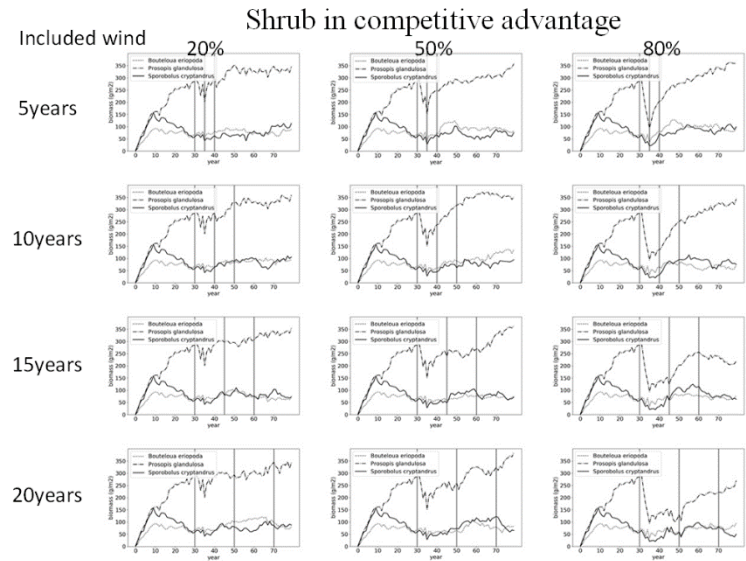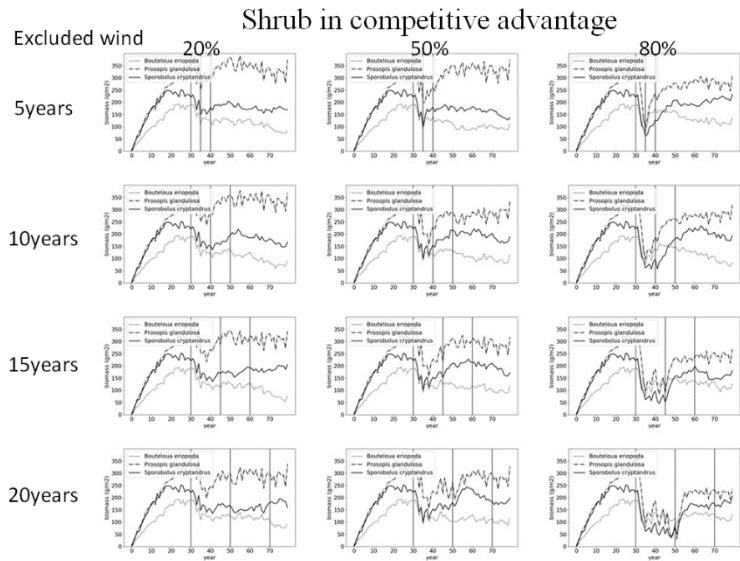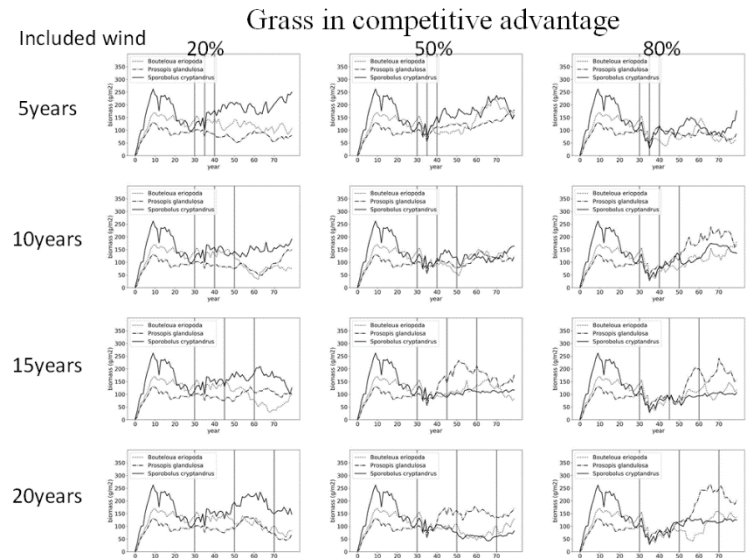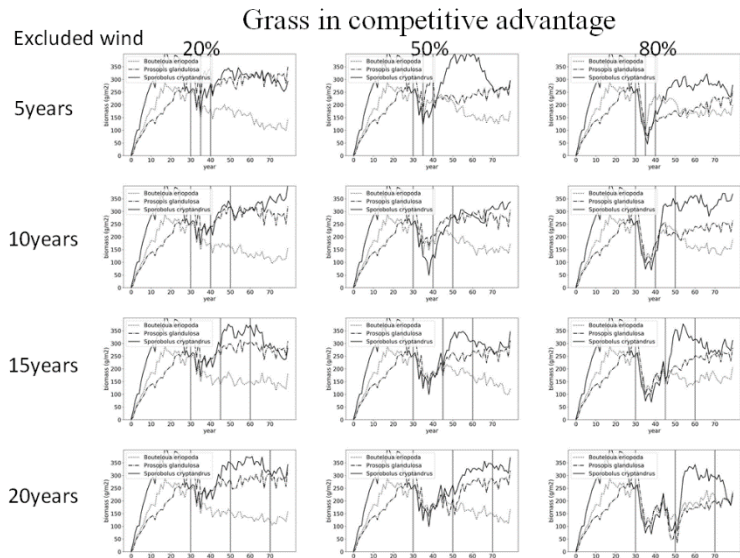
Figure 8 Starting with above-normal precipitation, the impact of drought with (right) and without wind (left), in cases where shrubs have competitive advantage (lower) and where grasses have competitive advantage (upper). All runs had a 10-year period without wind for spin up. The droughts started in year 30 of the runs. Drought is represented by the percent reduction of precipitation from above-normal during the drought.

5 Discussion and conclusions

There have been several major attempts to simulate the coupling between aeolian processes and vegetation growth. For example, Nield and Baas's (2008) model is a cellular automata model of geomorphic change that uses vegetation to alter the movement of slabs of soil by wind. The aerodynamic effect of vegetation is parameterized by an empirical function that is not rooted in drag partition theory. This model uses highly simplistic vegetation growth models that are tuned, for different plant functional types, which do not compete, to reproduced specific types of linked aeolian-vegetation landscapes. Stewart et al.'s (2014) model focuses on the role of vegetation patterning in resource movement and is aimed at investigating the role of connectivity in dryland functions. Vegetation growth in this model uses a simplistic limiting-resource approach and does not explicitly consider competition between plants or plant functional types. This model also does not explicitly calculate sediment movement or calculate changes in soil height. Mayaud et al.'s (2017) model is probably the closest to the model presented here. It is a coupled geomorphic-vegetation cellular automaton model, which implements the Okin's (2008) aeolian transport model logic to accomplish transport and predict changes in soil height. The purpose of Mayaud et al's. model is to "predict transitions from vegetated, geomorphically inactive landscapes to more active unvegetated landscapes in globally significant dryland ecogeomorphic systems". This model is

ecologically naïve and does not explicitly consider competition between plants or other important plant processes.

The model developed here differs from previous efforts in its coupling of a sophisticated ecological model, that considers the competitive dynamics of individual plants of various functional types, with a physically-based model of shear stress partitioning. So, although previous models exhibit good performance in simulating interactions between vegetation and transport in the developing plant and geomorphic patterns, simulating the dynamics of ecological state change, and the role that aeolian transport potentially plays in it, vegetation growth and competition were outside of their scope. The model of Okin et al. (2009a) also showed the impact of erosion on state change, but as a highly simplistic model that treated vegetation growth of generalized functional types using a simple logistic approach and in which erosion was handled implicitly, it was not of any utility in predicting the behavior of whole landscapes.

Nonetheless, one of the benefits of the Okin et al. (2009a) model was that could properly reproduce the expected dynamics whereby the system was unistable in the absence of a feedback and became bistable in the presence of a feedback. This is an important component of modern dryland ecological theory, going back to the seminal work of Noy-Meir (1975) which led to the development of ideas about multiple stable states and non-equilibrium ecological dynamics. The model developed here elaborates, using physically and ecologically realistic approaches, on the emergence of bistability in drylands. For example, in the absence of aeolian transport (i.e., in the absence of a feedback), the model runs converge on similar grass/shrub ratios, whether grasses or shrubs are advantaged (Figure 5). Inclusion of a feedback induces bistability, which can clearly be

106

seen where profound drought leads to the inversion of species dominance in the grass-advantaged case (Figure 7).

The encroachment of shrubs into grasslands has long been a topic of interest among dryland ecologists. The causes for the rapidity and seeming irreversibility of the changes that have been observed worldwide has been subject of intense research and debate. One of the areas of uncertainty within these debates has been whether grasses or shrubs were more fit and whether changes (such as climate change or increased atmospheric CO_2 concentrations) changed the environment to favor the fitness of shrubs. In cases where shrubs are more fit, causes for the existence of grasslands is suspect, with some mechanisms required to prevent the growth of shrubs. Fredrickson et al. (2006), for example, have argued that predation pressures prevented the expansion of shrub patches into grasslands. Fire, too, is often cited as a way that grasslands could be maintained even when shrubs were more fit, because fires in grasslands could kill shrub seedlings thus preventing establishment (e.g. Archer et al., 1995). Our model, perhaps, sheds some light on the shrub-advantaged case, showing that aeolian transport acts to exacerbate the advantage of shrubs by increasing the mortality of grasses (Figure 5).

A bigger mystery in the discussion of shrub encroachment has been how shrubs can invade if grasses have fundamental biological advantages. Okin et al. (2009a) proposed a solution to this by suggesting that erosion- or transport-related feedbacks may lead to grass mortality, making space for shrubs, even when grasses are advantaged. The emergence of bistability in the presence of aeolian transport-related feedbacks in our model elaborates on this idea and provides insight into the spatial dynamics that play into this phenomenon. By explicitly combining a model of

considerable biological complexity with ongoing research into the role of connectivity in determining landscape dynamics in drylands through use of a physically-based transport model, the present work contributes to our understanding of the complex landscape-scale dynamics that determine the fate of the world's drylands.

References

Alvarez, L.J., Epstein, H.E., Li, J., & Okin, G.S. (2011). Spatial patterns of grasses and shrubs in an arid grassland environment. *Ecosphere, 2*, 589

Armbrust, D., & Retta, A. (2000). Wind and sandblast damage to growing vegetation. *Annals of Arid Zone, 39*, 273-284

Brady, N.C., & Weil, R.R. (2008). *The nature and properties of soils*. Pearson Prentice Hall Upper Saddle River

Buffington, L.C., & Herbel, C.H. (1965). Vegetational changes on a semidesert grassland range from 1858 to 1963. *Ecological Monographs, 35*, 139-164

Cleugh, H., Miller, J., & Böhm, M. (1998). Direct mechanical effects of wind on crops. *Agroforestry Systems, 41*, 85-112

D'Odorico, P., Okin, G.S., & Bestelmeyer, B.T. (2012). A synthetic review of feedbacks and drivers of shrub encroachment in arid grasslands. *Ecohydrology, 5*, 520-530

Gautam, R., Hsu, N.C., Lau, W.K.M., & Yasunari, T.J. (2013). Satellite observations of desert dust-induced Himalayan snow darkening. *Geophysical Research Letters, 40*, 988-993

Gillette, D.A., & Chen, W. (2001). Particle production and aeolian transport from a "supply-limited" source area in the Chihuahuan desert, New Mexico, United States. *Journal of Geophysical Research: Atmospheres, 106*, 5267-5278

Gillette, D.A., & Pitchford, A.M. (2004). Sand flux in the northern Chihuahuan Desert, New Mexico, USA, and the influence of mesquite-dominated landscapes. *Journal of Geophysical Research: Earth Surface, 109*

Ginoux, P. (2003). Effects of nonsphericity on mineral dust modeling. *Journal of Geophysical Research-Atmospheres, 108*, 7840

Herrick, J.E., Van Zee, J.W., Havstad, K.M., Burkett, L.M., Whitford, W.G., Bestelmeyer, B.T., Melgoza, A., Pellant, M., Pyke, D.A., & Remmenga, M.D. (2017). Monitoring manual for grassland, shrubland and savanna ecosystems. Volume I: Core Methods. In: USDA ARS Las Cruces, New Mexico. The University of Arizona Press

Kok, J.F. (2011). A scaling theory for the size distribution of emitted dust aerosols suggests climate models underestimate the size of the global dust cycle. *Proceedings of the National Academy of Sciences of the United States of America, 108*, 1016-1021

Lancaster, N., Nickling, W.G., & Gillies, J.A. (2010). Sand transport by wind on complex surfaces: Field studies in the McMurdo Dry Valleys, Antarctica. *Journal of Geophysical Research: Earth Surface, 115*

Laurent, B., Marticorena, B., Bergametti, G., Leon, J.F., & Mahowald, N.M. (2008). Modeling mineral dust emissions from the Sahara desert using new surface properties and soil database. *Journal of Geophysical Research-Atmospheres, 113*, 9465

Li, J., Okin, G.S., Alvarez, L., & Epstein, H. (2007). Quantitative effects of vegetation cover on wind erosion and soil nutrient loss in a desert grassland of southern New Mexico, USA. *Biogeochemistry, 85*, 317-332

Li, J., Okin, G.S., Alvarez, L., & Epstein, H. (2008). Effects of wind erosion on the spatial heterogeneity of soil nutrients in two desert grassland communities. *Biogeochemistry, 88*, 73-88

Li, J.R., Okin, G.S., & Epstein, H.E. (2009). Effects of enhanced wind erosion on surface soil texture and characteristics of windblown sediments. *Journal of Geophysical Research-Biogeosciences, 114*, 455

Li, J.R., Okin, G.S., Herrick, J.E., Belnap, J., Miller, M.E., Vest, K., & Draut, A.E. (2013). Evaluation of a new model of aeolian transport in the presence of vegetation. *Journal of*

Geophysical Research-Earth Surface, 118, 288-306

Lopez, M.V. (1998). Wind erosion in agricultural soils: an example of limited supply of particles available for erosion. *Catena, 33*, 17-28

Marticorena, B., & Bergametti, G. (1995). Modeling the atmospheric dust cycle: 1. Design of a soil-derived dust emission scheme. *Journal of Geophysical Research: Atmospheres, 100*, 16415-16430

Mayaud, J.R., Bailey, R.M., & Wiggs, G.F. (2017). A coupled vegetation/sediment transport model for dryland environments. *Journal of Geophysical Research: Earth Surface, 122*, 875-900

McGlynn, I.O., & Okin, G.S. (2006). Characterization of shrub distribution using high spatial resolution remote sensing: Ecosystem implications for a former Chihuahuan Desert grassland. *Remote Sensing of Environment, 101*, 554-566

Nield, J.M., & Baas, A.C. (2008). Investigating parabolic and nebkha dune formation using a cellular automaton modelling approach. *Earth Surface Processes and Landforms, 33*, 724-740

Nousiainen, T., Zubko, E., Niemi, J.V., Kupiainen, K., Lehtinen, M., Muinonen, K., & Videen, G. (2009). Single-scattering modeling of thin, birefringent mineral-dust flakes using the discrete-dipole approximation. *Journal of Geophysical Research-Atmospheres, 114*, 9567

Okin, G.S. (2005). Dependence of wind erosion and dust emission on surface heterogeneity: Stochastic modeling. *Journal of Geophysical Research-Atmospheres, 110*, 110

Okin, G.S. (2008). A new model of wind erosion in the presence of vegetation. *Journal of Geophysical Research-Earth Surface, 113*, 954

Okin, G.S., D'Odorico, P., & Archer, S.R. (2009a). Impact of feedbacks on Chihuahuan desert grasslands: transience and metastability. *Journal of Geophysical Research: Biogeosciences, 114*

Okin, G.S., Gillette, D.A., & Herrick, J.E. (2006). Multi-scale controls on and consequences of

aeolian processes in landscape change in arid and semi-arid environments. *Journal of Arid Environments, 65*, 253-275

Okin, G.S., Parsons, A.J., Wainwright, J., Herrick, J.E., Bestelmeyer, B.T., Peters, D.C., & Fredrickson, E.L. (2009b). Do Changes in Connectivity Explain Desertification? *Bioscience, 59*, 237-244

Parton, W.J., Stewart, J.W., & Cole, C.V. (1988). Dynamics of C, N, P and S in grassland soils: a model. *Biogeochemistry, 5*, 109-131

Peters, D. (2002). Plant species dominance at a grassland-shrubland ecotone: an individual-based gap dynamics model of herbaceous and woody species. *Ecological Modelling, 152*, 5-32

Pye, K. (2015). *Aeolian dust and dust deposits*. Elsevier

Rastetter, E.B., Aber, J.D., Peters, D.P., Ojima, D.S., & Burke, I.C. (2003). Using mechanistic models to scale ecological processes across space and time. *Bioscience, 53*, 68-76

Raupach, M.R., Gillette, D.A., & Leys, J.F. (1993). The Effect of Roughness Elements on Wind Erosion Threshold. *Journal of Geophysical Research-Atmospheres, 98*, 3023-3029

Ravi, S., Breshears, D.D., Huxman, T.E., & D'Odorico, P. (2010). Land degradation in drylands: Interactions among hydrologic-aeolian erosion and vegetation dynamics. *Geomorphology, 116*, 236-245

Shao, Y.P., Nickling, W., Bergametti, G., Butler, H., Chappell, A., Findlater, P., Gillies, J., Ishizuka, M., Klose, M., Kok, J.F., Leys, J., Lu, H., Marticorena, B., McTainsh, G., McKenna-Neuman, C., Okin, G.S., Strong, C., & Webb, N. (2015). A tribute to Michael R. Raupach for contributions to aeolian fluid dynamics. *Aeolian Research, 19*, 37-54

Shugart, H.H. (2000). Importance of structure in the longer-term dynamics of landscapes. *Journal of Geophysical Research-Atmospheres, 105*, 20065-20075

Stewart, J., Parsons, A.J., Wainwright, J., Okin, G.S., Bestelmeyer, B.T., Fredrickson, E.L., & Schlesinger, W.H. (2014). Modeling emergent patterns of dynamic desert ecosystems. *Ecological Monographs, 84*, 373-410

Turnbull, L., Wilcox, B.P., Belnap, J., Ravi, S., D'odorico, P., Childers, D., Gwenzi, W., Okin, G., Wainwright, J., & Caylor, K. (2012). Understanding the role of ecohydrological feedbacks in ecosystem state change in drylands. *Ecohydrology, 5*, 174-183

Vest, K.R., Elmore, A.J., Kaste, J.M., Okin, G.S., & Li, J.R. (2013). Estimating total horizontal aeolian flux within shrub-invaded groundwater-dependent meadows using empirical and mechanistic models. *Journal of Geophysical Research-Earth Surface, 118*, 1132-1146

Wright, R.G. (1973). demographic study of a semi-desert grassland

Chapter 4 Developing a continental-scale dust emission model based on land surface indicators derived from satellite remote sensing images

Abstract: Dust plays a crucial role in climate and ecosystems and strongly impact the atmosphere, biosphere, hydrosphere, and cryosphere. Although much effort has been made to detect and estimate dust emission from remote sensing and the use of models, both methods still have difficulties with either spatial resolution and lack of extensive information about the erodible land surface. A new approach was developed to estimate dust emission across the Intermontane West. This model contains two parts: 1. a machine learning-based data assimilation method to predict land surface indicators at a continental scale, and 2. a process-based wind erosion model, which uses these indicators to estimate dust emission potential. Compared to the dust optical depth (DOD) derived from Moderate Resolution Imaging Spectroradiometer (MODIS) Deep Blue product, the predicted dust emission has a good annual agreement over 14 years from 2003-2016 in six major North American dust source regions.

1 Introduction

Dust emission in drylands is significant for the Earth system (Ravi et al. 2011; Shao et al. 2011). Dust impacts the fertility of soils via deflation of nutrient components (Goudie and Middleton 2006) and is considered as triggers of serious epidemics (e.g. meningitis) through the transport of pathogens (Thomson et al. 2006). Large dust events (e.g. dust storms) negatively affect human respiratory systems through inhaled dust particles into lungs (De Deckker et al. 2008) and also harmfully impact air and road transportation by decreasing visibility (Tegen et al. 2002). Dust aerosols influence atmospheric radiation balance directly (Miller et al. 2006) and indirectly by

changing the optical properties and the lifetime of clouds (Liou and Ou 1989; Twomey et al. 1984). During transport into the atmosphere, dust reacts with other components and thus modifies the chemical composition of atmospheric components (Bauer et al. 2004). Dust deposition impacts the biosphere by acting as a major large-scale transporter of iron and phosphorus to the terrestrial and marine ecosystems (Knippertz and Stuut 2014). Dust deposited on snow reduces surface albedo and changes surface energy balance, with considerable impacts on snowmelt and mountain hydrology (Painter et al. 2012).

Because dust emission plays such a key role in the Earth system, much research (Gautam et al. 2013; Ginoux 2003; Kok 2011; Laurent et al. 2008; Nousiainen et al. 2009; Okin 2005; Pye 2015) has been done on estimating dust emission at a continental scale (>1000 km). In general, there are two major approaches for estimating dust emission (Knippertz and Stuut 2014). One is to develop a physical model based on mechanisms of dust emission. The other is to use satellite- or ground-based remote sensing data to estimate dust in the air. The latter approach, especially when spaceborne instruments are used, can be an effective way to estimate atmospheric dust content and distribution. For instance, an algorithm using Moderate Resolution Imaging Spectroradiometer (MODIS) Deep Blue product (Hsu et al. 2004; Hsu et al. 2006) has been designed to identify global dust resources and their emission rates by Ginoux et al. (2012). Alternatively, Aerosol Robotic Network (AERONET) measurements have been used to identify global aerosol resources by Chin (2009). Although dust content estimates based on remotely sensed data can provide an atmospheric dust content and distribution at a continental scale, they do not directly estimate emission (Knippertz and Stuut 2014) and the estimates of dust content (or related parameters) have intrinsic spatial and temporal resolutions that may or may not be useful. For example, MODIS Deep Blue

provides daily global coverage, the highest temporal resolution among all satellite dust products (Hsu et al. 2004); but the spatial resolution is only 0.1 degree and the uncertainty of non-major dust sources is relatively high (Sayer et al. 2013; Sayer et al. 2014). AERONET also provides a daily dust product (Holben et al. 1998), but the AERONET stations are irregularly distributed, and therefore the spatial characteristics of AERONET are suboptimal, especially in large, sparsely populated desert areas.

There have been a number of efforts to model dust emissions. For example, in order to estimate dust flux from the surface in the U.S., a physical dust emission model was created initially by Gillette and Passi (1988). A soil-derived dust emission scheme was developed to characterize dust sources by Marticorena and Bergametti (1995). A new parameterization for dust emission was created by Zender et al. (2003) and was later incorporated into a global model by Mahowald et al. (2005) and an Earth system model (ESM) by Albani et al. (2014). Although the mechanism of dust production by sandblasting is well recognized (Bagnold 1941; Kok et al. 2012; Shao 2000; Shao and Raupach 1993) and was applied in some of these models, many of the existing models continue to have two major drawbacks. First, the effects of vegetation on dust emission are treated implicitly (Webb et al. 2014). Second is that they are lack of extensive information about the erodible land surface in their study areas (Newton et al. 2009), which leads those dust emission models to underestimate dust emission, especially in dust sources (Ginoux et al. 2010).

To solve those two problems, a new approach using Okin's wind erosion model (WEMO model; Okin, 2008) and predictions from a machine learning-based data assimilation algorithm (Chapter

116

2) was developed to estimate dust emission. Random forest (RF) predictions utilizing remotely-sensed data of surface indicators, such as bare soil cover, vegetation cover, the fractions of gap length, and herbaceous plant height were ingested into a continental-scale version of WEMO model estimate vertical dust flux in the Western U.S. Confirmation of the validity of this approach was provided using coarse-scale satellite estimates of dust optical depth (DOD) from the MODIS Deep Blue product in large regions that were identified by Ginoux et al. (2012) as major North American dust source areas.

2 Data and Methodology

2.1 Study area

The study area encompasses eleven states in the Western U.S. excluding the region east of the Rocky Mountains and west of the Sierra Nevada, often referred to as the Intermontane West. Generally, the Intermontane West has an arid and semiarid climate, although this is not true everywhere. Nonetheless, deserts, semiarid and arid areas, and mountains make up most of the land cover in the region. The main types of vegetation are grass and shrub with a small fraction of the forest (Loveland et al. 1991). The windy season in the region is from March to May of each year (Westerling et al. 2003).

The major dust sources in North America are concentered in two broad regions: 1) the high plains on the east side of the Rocky Mountains, which are not included in this study, and 2) the Intermontane West, including the Sonoran Desert, the Chihuahuan Desert, the Sevier Desert, the Little Colorado River, the Mojave Desert, the San Joaquin Valley, northwest Arizona, the Lower Yellowstone Valley, the Wyoming Basin, and the Southern High Plains (Figure 1). Those dust

sources can be divided into three groups base on their attributions: hydrologic dust sources, natural but non-hydrologic dust sources, and anthropogenic but non-hydrologic dust sources (Ginoux et al. 2012). Hydrologic dust sources are associated to ephemeral water bodies or other hydrologic features, natural but non-hydrologic dust sources are in locations where intensive land use covers less than 30% of the land surface, and anthropogenic but non-hydrologic dust sources are in locations where intensive land use covers more than 30% of the land surface (Ginoux et al. 2012). The Sonoran Desert is recognized as a natural dust source, even though the dust emission on the east side of the Sonoran Desert (located at the Gulf of California) can be anthropogenic (Moreno-Rodríguez et al. 2015). The Mojave Desert is one of the largest dust sources in the Western U.S. and it is known as a natural dust source though, although there are anthropogenic sources within it (Reynolds et al. 2007). The Lower Yellowstone Valley and San Joaquin Valley are the major anthropogenic dust sources in the Intermontane West due to agricultural activities (Nordstrom and Hotta 2004). The Sevier Desert is comprised of several ephemeral lakes and alluvial fans as an eastern extension of the Basin and Range province (Neff et al. 2008), so it is recognized as a hydrologic dust source. The Southern High Plains, Wyoming Basin, Chihuahuan Desert, and Little Colorado River area are known as anthropogenic dust sources because of agriculture and grazing (Rivera et al. 2010). The dust emission from northwest Arizona is recognized as a hydrological dust source (Munson et al. 2011).
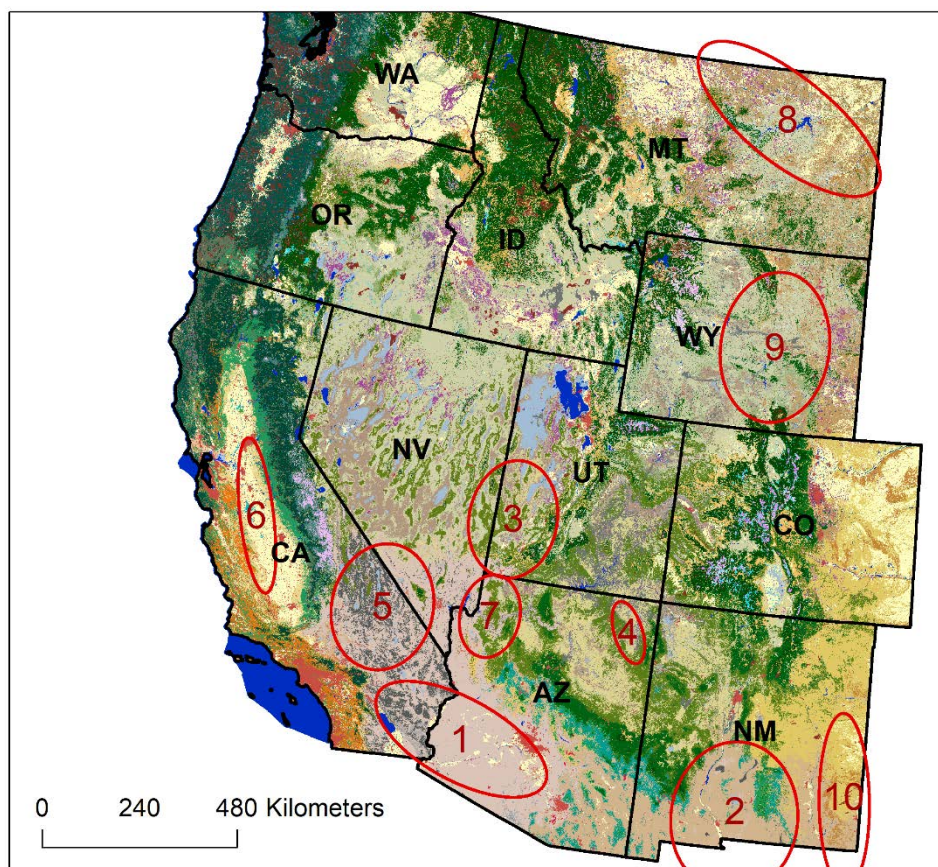
Figure 1 The major dust sources in the Western U.S. (1. Sonoran Desert, 2. Chihuahuan Desert, 3. Sevier Desert, 4. Little Colorado River, 5. Mojave Desert, 6. San Joaquin Valley, 7. northwest Arizona, 8. Lower Yellowstone Valley, 9. Wyoming Basin, and 10. Southern High Plains).

2.2 Data

Description of the data and algorithms used to calculate the land surface indicators can be found in Chapter 2. Here, we used the indicators of bare soil cover, vegetation cover, gap fractions, and herbaceous plant height (MacKinnon et al. 2011). WEMO also requires information on wind speed and soil texture. For validation, we used the atmospheric DOD from MODIS Deep Blue (MYD04) in March from 2003 to 2016, which were the only months during dust emission was estimated.

Wind speed was measured by fourteen airports or weather stations at 5-minute intervals in the height of 10 m near to the major dust sources in the Western U.S. The data can be found in Automated Surface Observing System (https://mesonet.agron.iastate.edu/ASOS/). In order to make a non-tempo-spatial wind speed, we calculated the monthly mean wind speed of each station in March 2009 and averaged the monthly mean wind speed of each station. This wind speed was interpolated by Weibull distribution to produce a distribution of wind speed. Soil texture was derived from soil property maps created by data assimilation of remote sensing products and *in situ* observation (Ramcharan et al. 2018). These maps have a 100 m spatial resolution and have been validated by Gridded Soil Survey Geographic (gSSURGO) Database (Ramcharan et al. 2018). This data can be found at Pennsylvania State University's website (https://scholarsphere.psu.edu/collections/jw827b80n).
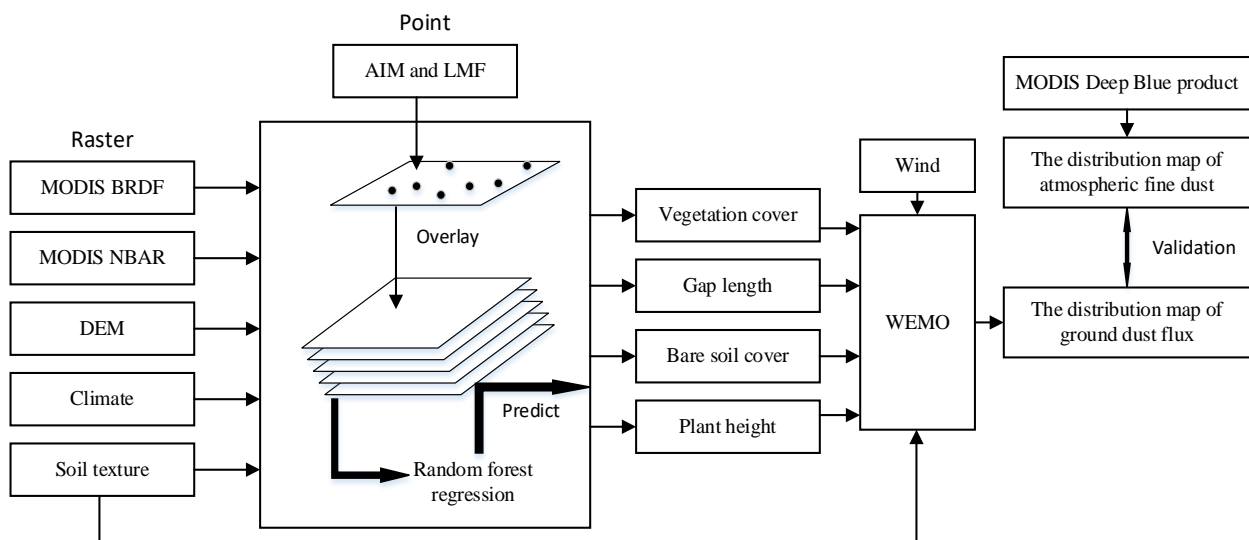

Figure 2 General data processing and model running workflow.

2.3 Random forest regression

Details of the RF regression used to produce surface indicators can be found in Chapter 2. The indices used here include bare soil cover, total vegetation cover, gap fractions, and herbaceous plant height. The spatial resolution of the predicted distribution maps is 500 m. Gap fractions consisted of the cover of a gap with length 1) between 25 to 50 cm, 2) between 50 to 100 cm, 3) between 100 to 200 cm, 4) between 200 to 250 cm, and 5) greater than 250 cm. In order to build the distribution of erodible gaps required for WEMO, we defined the median gap size as the weighted average gap length using intermediate values for each group (37.5 cm, 75 cm, 150 cm, 225 cm, and 500 cm, respectively).

2.4 WEMO model

WEMO uses a size distribution of erodible gaps between plants, instead of lateral cover, to describe the distribution of shear stress at the surface. A major advantage of this model is that the primary input variables can be obtained by standard field methods (Herrick et al. 2017) or orthophotography techniques (Chapter 1). Based on the researches of Vest et al. (2013), Lancaster et al. (2010), Li et al. (2013), and Mayaud et al. (2017), the WEMO model performed better than more traditional shear stress partitioning approaches (e.g., Raupach et al., 1995).

The first step of calculating horizontal flux in WEMO is to convert a wind speed at a certain height to a wind shear velocity at the surface. Based on the law of wall (Lopez 1998), the expression of shear velocity u_* at a certain height (1000 cm in this study) is given by:

$$u_* = K \times \frac{u}{\log\left(\frac{z}{z_o}\right)},$$ (1)

where K refers to von Karman coefficient (0.4), and u is the wind speed at the measured height z.

Li et al. (2013) determined that, for the purposes of WEMO, the best value of the roughness length

(z_o) in this context is 7.9 cm. In WEMO, the ratio of the surface shear velocity in the wake of plants

to the surface shear velocity in the absence of plants ($\frac{u_{*S}}{u_*}$), is calculated as:

$$\frac{u_{*S}}{u_*} = \frac{u_{*S}}{u_*}\bigg|_{x=0} + \left(1 - \frac{u_{*S}}{u_*}\bigg|_{x=0}\right) \times \left(1 - \exp\left(-\frac{c}{x}\right)\right),$$ (2)

where $\frac{u_{*S}}{u_*}\bigg|_{x=0}$ is the ratio immediately downwind of a plant and c is the e-folding distance for the

recovery of the shear stress in the unit of plant height. Based on the data of Li et al. (2013), the

best-fit value of c is 5.6 and the best-fit value of $\frac{u_{*S}}{u_*}\bigg|_{x=0}$ is 0.29. x is the gap length expressed in

units of plant height. Horizontal flux ($Q_x^{u_*}$) at a gap length (x) in the shear stress wake zone is

calculated as Gillette and Chen (2001):

$$Q_x^{u_*} = A \times \frac{\rho}{g} \times u_{*S} \times (u_{*S}^2 - u_{*t}^2),$$ (3)

where A is a best-fit constant (0.026), ρ is the density of air (0.00129 g/cm^3), g is the acceleration

due to gravity (980 cm/s^2), and u_{*t} is the threshold of wind shear velocity of the unvegetated soil

(Gillette et al. 1980; Li et al. 2013), such that:

if clay content $\geq$ 20%:

$$u_{*t} = 400 + 2.4 \times \text{rock content};$$ (4)

if clay content<20%:

$$u_{*t}=165.7-139\times \text{ (sand content + clay content)}/100+2.4\times\text{rock content.} \tag{5}$$

The probability (P_d) that any point in the reduced shear stress zone is at a certain distance from the nearest upwind plant, in units of plant height, is estimated as an exponential function (Okin and McGlynn, 2001) with decay constant equal to the estimated median weighted average gap size divided by estimated plant height. The horizontal flux Q_t^{u*} of the whole shear stress wake zone at a specific wind shear velocity (u_*), is the sum of Q_x^{u*} for all gap lengths (x) weighted by P_d such that:

$$Q_t^{u*} = (1 - C)\sum_x P_d(x) \times Q_x^{u_*}, \tag{6}$$

where C is the estimated vegetation cover from RF. To calculate the total horizontal flux (Q), Q_t^{u*} is summed for all wind shear velocities (u_*) weighted by the probability distribution of wind shear velocity (P_{u*}) such that:

$$Q = \sum_{u*} P_{u*} \times Q_t^{u*}. \tag{7}$$

P_{u*} is the Weibull distribution based on the monthly mean wind speed at a certain location. The vertical flux (F) is derived from the horizontal flux (Q), and therefore has the same spatial resolution:

$$F = k \times Q, \tag{8}$$

where k is the sandblasting efficiency (Kok et al. 2012), which is given by (Marticorena and Bergametti 1995):

if clay content ≥20%:

$$k=\exp(0.134\times\text{clay content}-6); \tag{9}$$

if clay content <20%:

$$k=0.005. \tag{10}$$

2.5 Model validation

In order to confirm the validity of our approach for estimating dust flux, three sub-products of MODIS Deep Blue Version 6 product (MYD04) were used: Deep Blue Aerosol Optical Depth Best Estimate at 550 nm, Deep Blue Angstrom Exponent at either 412/470 nm or 470/650 nm (depends on light land surface or dark land surface), and Deep Blue Spectral Single Scattering Albedo at 412, 470, and 650 nm. Together, these data were used to derive dust optical depth (Hsu et al. 2004). MODIS MYD04 data are daily and have a 0.1 degree (approximately 10 km) spatial resolution.

MODIS quantifies atmospheric aerosol content by estimating the vertical integrated aerosol extinction of atmosphere. The Deep Blue algorithm is designed to retrieve the aerosol optical depth (AOD) and the Angstrom Exponent (α) over land, which can be used to estimate dust optical depth (Hsu et al. 2004). The algorithm of Ginoux et al. (2012) has three conditions: 1. dust particles are coarser than biomass burning particles, so the value of α must be between 0 to 1 for dust (Osborne et al. 2008); 2. sea salt particles, which are also in the coarse mode, are brighter than dust particles, so the single scattering albedo at 412 nm must be less than 0.95 for dust (Rudich et al. 2002), and; 3. sulfate aerosols are non-absorbing aerosol and therefore the difference of single scattering albedo between 670 nm and 412 nm must be greater than 0 for dust (Ginoux et al. 2012). We

applied these three conditions on the Deep Blue Aerosol Optical Depth Best Estimate at 550 nm

determine mask DOD from AOD

For our validation, we extracted a 3×3 set of DOD pixels in the center of six major dust sources for each day during March of each year. A single value for each year was produced by summarizing the 9 daily pixels over March of each year. The values of dust emission estimate were produced by summarizing all estimates of dust emission within 400 (e.g., 20×20) 500-m pixels from the center of the Deep Blue 3×3 pixel area. In addition, we made the vertical dust flux distribution and DOD maps in the Western U.S. for each year. Although the DOD maps and dust emission maps cannot be directly compared with each other, a comparison does shed some light on similarities of general geographic distributions.

Python 3.6 with GDAL 2.4 package (https://gdal.org/) was used to process all raster and vector datasets. Python 3.6 with Scikit-learn 0.2 package (Pedregosa et al. 2011) was used to create the RF regression models and output the distribution maps. WEMO model was programmed in Python 3.6 based on the original WEMO code written in IDL.

3 Results

Predicted emissions in the Intermontane West do correlate well with most of the large dust emission areas identified by Ginoux et al. (2012), with large areas of predicted emission in the Sonoran Desert (1), Southern High Plains (10), Sevier Desert (3), Little Colorado River area (4), Mojave Desert (5), and northwestern Arizona (7) showing predicted dust emission (Figure 1).

When compared to MODIS, outside the San Joaquin Valley, in the southwestern states (California, Arizona, New Mexico, Nevada, and Utah) there is generally good spatial concordance between the areas of higher model dust emission and the areas of higher MODIS-derived DOD, particularly in the Mojave Desert, the southern Great Basin, the southern Colorado Plateau (including the Little Colorado River area), and the Sonoran Desert (Figure 3). MODIS DOD indicates considerable dust in the San Joaquin Valley that is not predicted by the model. The areas of highest predicted emission in Wyoming's Red Desert (part of the Wyoming Basin) are not captured by MODIS DOD. The areas of highest MODIS DOD in eastern Montana and southern Washington are associated with agricultural sources, with the Washington sources not identified by Ginoux et al. (2012) as a major source for North America. In New Mexico, there are extensive areas in the south-central portion of the state areas, comprising the Chihuahuan Desert, where dust emission is predicted, but where dust DOD does not appear elevated, at least in March 2009, although the Chihuahuan Desert is identified by Ginoux et al. (2012) as an important North American dust source. The southwestern portion of New Mexico, comprising part of the Southern High Plains shows both predicted emission and elevated DOD, though this is an important anthropogenic dust source, with considerable agriculture taking place throughout the Southern High Plains.
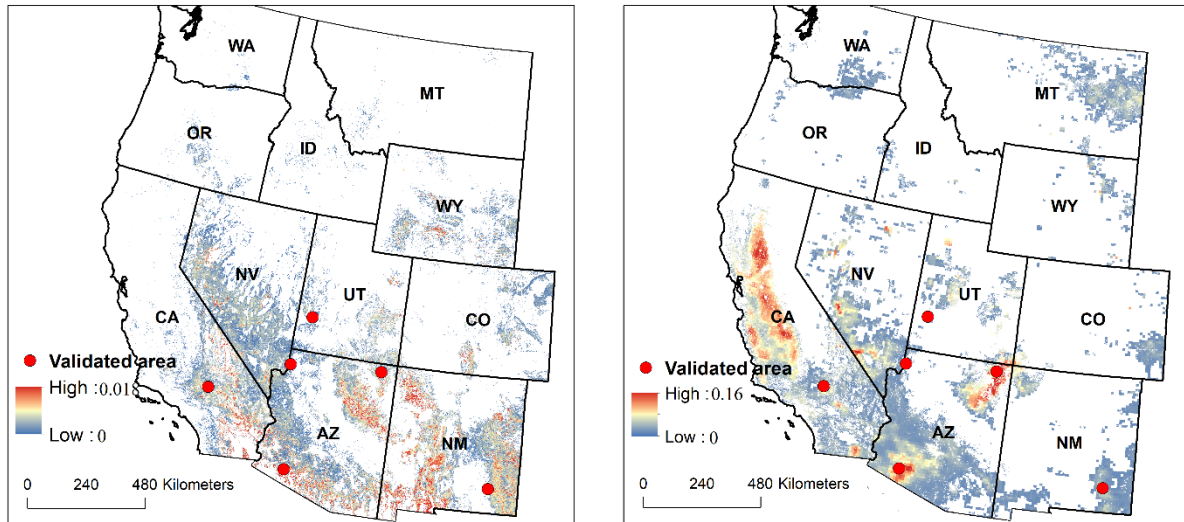
Figure 3 Left: Mean vertical flux (dust emission) estimates for March 2009. Right: Average MODIS-derived DOD in March 2009. Red dots represent the locations within six validation areas where detailed analyses were done.

When considering the temporal variability in dust emissions, we predicted mean March emissions for each year and compared these with mean MODIS DOD for the same periods. Five of the areas (the Mojave Desert, the Sevier Desert, the Sonoran Desert, northwestern Arizona, and the Southern High Plains) showed significant ($R^2_{crit} = 0.264$ for $\alpha = 0.05$ with d.f. = 13; Sokal and Rohlf, 1980) positive linear correlations (Figure 4). The Little Colorado River area indicted a positive, but not quite significant (at $\alpha = 0.05$) relationship. The y-intercept (dust flux, g cm^{-2}) was positive for all of the linear relations, indicating that elevated dust flux was required to produce DOD > 0. The intercept for the Mojave and Sonoran Deserts were the highest, with northwestern Arizona and the Sevier desert exhibiting the lowest. The significant slopes for were generally from $1 - 3$ g cm^{-2}.
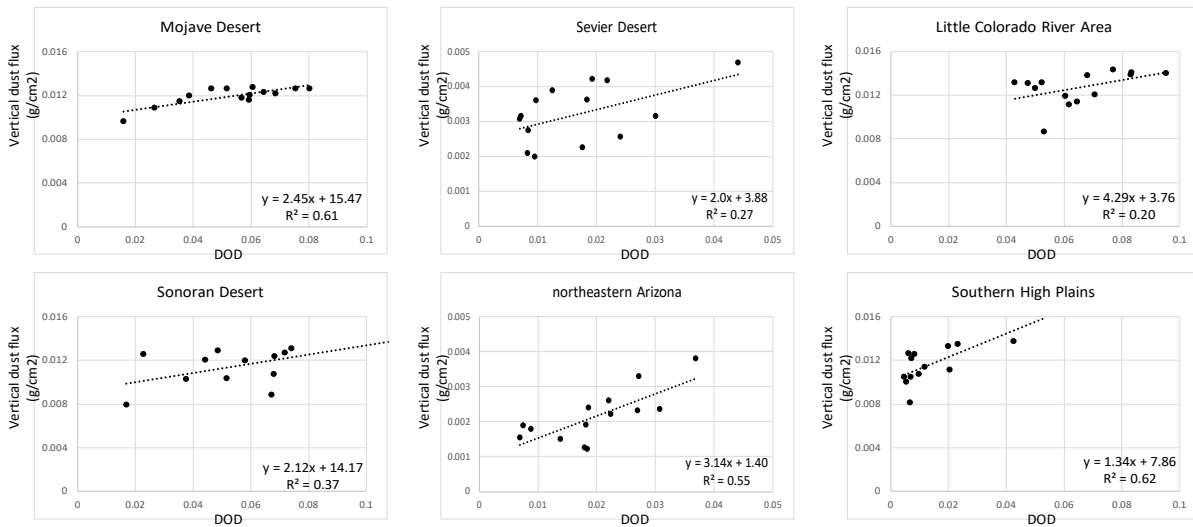
127

Figure 4 Estimated monthly mean vertical dust flux plotted against monthly mean DOD derived from MODIS Deep Blue product for six major dust resources.

4 Discussions

4.1 MODIS Deep Blue Version 6

MODIS Deep Blue and its AOD retrieval algorithm were originally created in the Collection 5 of MODIS product (Sayer et al. 2014). In Version 5, the AOD retrieval algorithm included negative Angstrom exponent values and thus could identify coarse dust particle (>5 μm) in the atmosphere. However, we used the new version of MODIS Deep Blue (Version 6). The Version 6 algorithm excludes the possibility of negative Angstrom exponent values (Sayer et al. 2013) and, therefore, the DOD derived from the Version 6 MODIS Deep Blue product cannot provide direct information on the distribution of coarse dust in the atmosphere. The Version 6 DOD is less sensitive to certain types of dust, explaining, perhaps why certain areas such as the Wyoming Basin and Chihuahuan Desert did not exhibit elevated dust in this study, even when they were identified by Ginoux et al. (2012) as significant North American dust sources using Version 5 (Figure 3). The modeling

approach used here, however, does suggest that these areas may be important sources of atmospheric dust, even if they are not observed in MODIS DOD.

4.2 Spatial and Temporal Correlation between Predicted Dust Emission and MODIS DOD

The two main non-meteorological controls on dust emission are the threshold shear velocity of the soil and the modulating effect of vegetation. In the absence of disturbance, the former is not expected to change over decadal timescales because the processes that control the cohesion of the soil and its texture are fundamentally slow pedogenic processes. Disturbance can, of course, rapidly change the surface threshold making disturbed soils that were well protected from aeolian transport highly susceptible to it. These dynamics are not captured in our model, because the equations used for surface threshold are those for disturbed soils (Gillette, 1980). When we used the thresholds for undisturbed soils, our analysis indicated very little potential dust emission. The fact that considerable dust emission is observed throughout the Intermountain West is a testament to the large-scale and long-lasting disturbance of the soil surface, which has been discussed in the context of pre-European fluxes by Neff et al. (2008), among others. Soil moisture can also directly increases the threshold shear velocity (Chepil 1956). In the context of the work presented here, however, soil moisture is not likely an important driver of the temporal dynamics of dust emission because 1) March is not a generally wet month in the region, as it falls between the winter wet period driven by synoptic storms and the summer Monsoon and 2) drying of the top 2 mm, which is the portion of the soil that is susceptible to aeolian processes, can occur on timeframes from minutes to hours (Ravi et al, 2004) meaning that wetting is not likely a major contributor to monthly dust emission.

Thus, the broad spatial patterns of dust emission are indicative of large-scale patterns in soils (i.e., threshold shear velocity) and vegetation composition. This is particularly true in the present implementation of the model because the same wind is used across the region, rather than using spatially-varying winds. In general, our model captures these major patterns in the Intermontane West, with some exceptions, like the Wyoming Basin and the Chihuahuan Desert, which did not show broad spatial agreement in our analysis. However, we note that these areas were identified by Ginoux et al. (2012) as major sources, so the discrepancy could be within the MODIS DOD itself, rather than with our potential model. The broad spatial agreement between our predicted emissions and Ginoux's dust source areas does suggest, in addition, that the use of the disturbed threshold shear velocity from Gillette (1980) provides a reasonable starting place for modeling of dust emissions at this scale. Given the historical and present use of large portions of the Intermontane West for large-scale disturbances such as oil and gas exploration and grazing, the assumption of disturbed soil is, perhaps, also justifiable. At present, further, there is no direct way to remotely identify surface disturbance, meaning that choice of threshold (disturbed or undisturbed) must be guided by *post hoc* analyses such as these.

Temporal variability in predicted dust emissions, when observed at a point over several years, such as done here, is related to the manner in which the model is capturing temporal variability in vegetation cover. This is particularly true in the present implementation of the model, which uses the same wind for every year of the record. Thus, we take the generally significant linear relationships between predicted flux and DOD as an indication that the model is correctly capturing the temporal variability of the vegetation in the study area. Further work is needed to

identify which variables (cover, height, gap size) exert the greatest effect on the variability in predicted dust emission. Nonetheless, the agreement between predicted monthly flux and monthly DOD does suggest that the use of remote sensing-derived surface data does potentially contribute considerably to the ability of our model to predict dust emissions.

The positive y-intercepts of the regressions of predicted dust flux against DOD perhaps indicate something important about this type of comparison. It takes relatively large amounts of dust, relatively high in the atmosphere to influence DOD, particularly over land using a multispectral instrument such as MODIS. Thus, one would not expect that small amounts of dust would register as elevated DOD. This is in agreement with the positive y-intercepts observed in our regressions, which are often greater than the full range of predicted dust emission observed at a site.

5 Conclusions

This study constitutes the first continental-scale implementation of a dust emission scheme based on a physically-based model of the influence of vegetation structure on dust emission. Though the spatial concordance of predicted dust emission may be due to the variability in soil variables, the strong relationship between predicted dust emissions for known dust emission areas, and observed DOD suggests that this approach has potential utility in understanding past and present spatial and temporal patterns of dust emission. Considerable further work is required to understand the sensitivity of the predicted dust emission to the remotely-derived vegetation structure variable, but this study serves as the first test of this approach. Nonetheless, the application of the specific remotely-derived vegetation indicators used here is largely restricted to the Intermontane West,

which is where the field data were collected that supported development of the machine learning-based predictions. Considerable further work, including potentially collecting additional field data, may be necessary to extend this approach regionally or globally.

References

Bagnold, R.A. (1941). *The Physics of Blown Sand and Desert Dunes*. Methuen & Company : William Morrow

Bauer, S.E., Balkanski, Y., Schulz, M., Hauglustaine, D.A., & Dentener, F. (2004). Global modeling of heterogeneous chemistry on mineral aerosol surfaces: Influence on tropospheric ozone chemistry and comparison to observations. *Journal of Geophysical Research-Atmospheres, 109*, 7983

Chepil, W.S. (1956). Influence of moisture on erodibility of soil by wind. *Soil Science Society of America Journal, 20*, 288-292

Chin, M., Diehl, T., Dubovik, O., Eck, T., Holben, B., Sinyuk, A., & Streets, D. (2009). Light absorption by pollution, dust, and biomass burning aerosols: a global model study and evaluation with AERONET measurements. In, *Annales Geophysicae* (pp. 3439-3464): Copernicus GmbH

De Deckker, P., Abed, R.M.M., de Beer, D., Hinrichs, K.U., O'Loingsigh, T., Schefuss, E., Stuut, J.B.W., Tapper, N.J., & van der Kaars, S. (2008). Geochemical and microbiological fingerprinting of airborne dust that fell in Canberra, Australia, in October 2002. *Geochemistry Geophysics Geosystems, 9*, 345

Gautam, R., Hsu, N.C., Lau, W.K.M., & Yasunari, T.J. (2013). Satellite observations of desert dust-induced Himalayan snow darkening. *Geophysical Research Letters, 40*, 988-993

Gillette, D.A., Adams, J., Endo, A., Smith, D., & Kihl, R. (1980). Threshold velocities for input of soil particles into the air by desert soils. *Journal of Geophysical Research: Oceans, 85*, 5621-5630

Gillette, D.A., & Chen, W. (2001). Particle production and aeolian transport from a "supply-limited" source area in the Chihuahuan desert, New Mexico, United States. *Journal of*

Geophysical Research: Atmospheres, 106, 5267-5278

Gillette, D.A., & Passi, R. (1988). Modeling dust emission caused by wind erosion. *Journal of Geophysical Research: Atmospheres, 93*, 14233-14242

Ginoux, P. (2003). Effects of nonsphericity on mineral dust modeling. *Journal of Geophysical Research-Atmospheres, 108*, 7840

Ginoux, P., Garbuzov, D., & Hsu, N.C. (2010). Identification of anthropogenic and natural dust sources using Moderate Resolution Imaging Spectroradiometer (MODIS) Deep Blue level 2 data. *Journal of Geophysical Research: Atmospheres, 115*

Ginoux, P., Prospero, J.M., Gill, T.E., Hsu, N.C., & Zhao, M. (2012). Global-Scale Attribution of Anthropogenic and Natural Dust Sources and Their Emission Rates Based on Modis Deep Blue Aerosol Products. *Reviews of Geophysics, 50*

Goudie, A., & Middleton, N.J. (2006). *Desert Dust in the Global System*. Springer Berlin Heidelberg

Herrick, J.E., Van Zee, J.W., Havstad, K.M., Burkett, L.M., Whitford, W.G., Bestelmeyer, B.T., Melgoza, A., Pellant, M., Pyke, D.A., & Remmenga, M.D. (2017). Monitoring manual for grassland, shrubland and savanna ecosystems. Volume I: Core Methods. In: USDA ARS Las Cruces, New Mexico. The University of Arizona Press

Holben, B.N., Eck, T.F., Slutsker, I., Tanre, D., Buis, J., Setzer, A., Vermote, E., Reagan, J.A., Kaufman, Y., & Nakajima, T. (1998). AERONET—A federated instrument network and data archive for aerosol characterization. *Remote Sensing of Environment, 66*, 1-16

Hsu, N.C., Tsay, S.-C., King, M.D., & Herman, J.R. (2004). Aerosol properties over bright-reflecting source regions. *Ieee Transactions on Geoscience and Remote Sensing, 42*, 557-569

Hsu, N.C., Tsay, S.-C., King, M.D., & Herman, J.R. (2006). Deep blue retrievals of Asian aerosol

properties during ACE-Asia. *Ieee Transactions on Geoscience and Remote Sensing, 44*, 3180-3195

Knippertz, P., & Stuut, J.-B.W. (2014). *Mineral dust : a key player in the earth system.* Springer

Kok, J.F. (2011). A scaling theory for the size distribution of emitted dust aerosols suggests climate models underestimate the size of the global dust cycle. *Proceedings of the National Academy of Sciences of the United States of America, 108*, 1016-1021

Kok, J.F., Parteli, E.J.R., Michaels, T.I., & Karam, D.B. (2012). The physics of wind-blown sand and dust. *Reports on Progress in Physics, 75*, 10

Lancaster, N., Nickling, W.G., & Gillies, J.A. (2010). Sand transport by wind on complex surfaces: Field studies in the McMurdo Dry Valleys, Antarctica. *Journal of Geophysical Research: Earth Surface, 115*

Laurent, B., Marticorena, B., Bergametti, G., Leon, J.F., & Mahowald, N.M. (2008). Modeling mineral dust emissions from the Sahara desert using new surface properties and soil database. *Journal of Geophysical Research-Atmospheres, 113*, 9465

Li, J.R., Okin, G.S., Herrick, J.E., Belnap, J., Miller, M.E., Vest, K., & Draut, A.E. (2013). Evaluation of a new model of aeolian transport in the presence of vegetation. *Journal of Geophysical Research-Earth Surface, 118*, 288-306

Liou, K.N., & Ou, S.C. (1989). The Role of Cloud Microphysical Processes in Climate - an Assessment from a One-Dimensional Perspective. *Journal of Geophysical Research-Atmospheres, 94*, 8599-8607

Lopez, M.V. (1998). Wind erosion in agricultural soils: an example of limited supply of particles available for erosion. *Catena, 33*, 17-28

Loveland, T., Merchant, J., Brown, J., & Ohlen, D. (1991). Development of a land-cover

characteristics database for the conterminous U. S. *Photogrammetric Engineering and Remote Sensing, 57*, 1453-1463

MacKinnon, W.C., Karl, J.W., Toevs, G.R., Taylor, J.J., Karl, S., Spurrier, C.S., & Herrick, J.E. (2011). *BLM core terrestrial indicators and methods*. US Department of the Interior, Bureau of Land Management, National Operations Center Denver

Marticorena, B., & Bergametti, G. (1995). Modeling the atmospheric dust cycle: 1. Design of a soil-derived dust emission scheme. *Journal of Geophysical Research: Atmospheres, 100*, 16415-16430

Mayaud, J.R., Bailey, R.M., & Wiggs, G.F. (2017). A coupled vegetation/sediment transport model for dryland environments. *Journal of Geophysical Research: Earth Surface, 122*, 875-900

Miller, R.L., Cakmur, R.V., Perlwitz, J., Geogdzhayev, I.V., Ginoux, P., Koch, D., Kohfeld, K.E., Prigent, C., Ruedy, R., Schmidt, G.A., & Tegen, I. (2006). Mineral dust aerosols in the NASA goddard institute for Space Sciences ModelE atmospheric general circulation model. *Journal of Geophysical Research-Atmospheres, 111*, 9456

Moreno-Rodríguez, V., Del Rio-Salas, R., Adams, D.K., Ochoa-Landin, L., Zepeda, J., Gómez-Alvarez, A., Palafox-Reyes, J., & Meza-Figueroa, D. (2015). Historical trends and sources of TSP in a Sonoran desert city: Can the North America Monsoon enhance dust emissions? *Atmospheric Environment, 110*, 111-121

Munson, S.M., Belnap, J., & Okin, G.S. (2011). Responses of wind erosion to climate-induced vegetation changes on the Colorado Plateau. *Proceedings of the National Academy of Sciences, 108*, 3854-3859

Neff, J., Ballantyne, A., Farmer, G., Mahowald, N., Conroy, J., Landry, C., Overpeck, J., Painter, T., Lawrence, C., & Reynolds, R. (2008). Increasing eolian dust deposition in the western United

States linked to human activity. *Nature Geoscience, 1*, 189

Newton, A.C., Hill, R.A., Echeverría, C., Golicher, D., Rey Benayas, J.M., Cayuela, L., & Hinsley, S.A. (2009). Remote sensing and the future of landscape ecology. *Progress in Physical Geography, 33*, 528-546

Nordstrom, K.F., & Hotta, S. (2004). Wind erosion from cropland in the USA: a review of problems, solutions and prospects. *Geoderma, 121*, 157-167

Nousiainen, T., Zubko, E., Niemi, J.V., Kupiainen, K., Lehtinen, M., Muinonen, K., & Videen, G. (2009). Single-scattering modeling of thin, birefringent mineral-dust flakes using the discrete-dipole approximation. *Journal of Geophysical Research-Atmospheres, 114*, 9567

Okin, G.S. (2005). Dependence of wind erosion and dust emission on surface heterogeneity: Stochastic modeling. *Journal of Geophysical Research-Atmospheres, 110*, 110

Okin, G.S. (2008). A new model of wind erosion in the presence of vegetation. *Journal of Geophysical Research-Earth Surface, 113*, 954

Osborne, S., Johnson, B., Haywood, J., Baran, A., Harrison, M., & McConnell, C. (2008). Physical and optical properties of mineral dust aerosol during the Dust and Biomass-burning Experiment. *Journal of Geophysical Research: Atmospheres, 113*

Painter, T.H., Bryant, A.C., & Skiles, S.M. (2012). Radiative forcing by light absorbing impurities in snow from MODIS surface reflectance data. *Geophysical Research Letters, 39*, 456

Pedregosa, F., Varoquaux, G., Gramfort, A., Michel, V., Thirion, B., Grisel, O., Blondel, M., Prettenhofer, P., Weiss, R., & Dubourg, V. (2011). Scikit-learn: Machine learning in Python. *Journal of Machine Learning Research, 12*, 2825-2830

Powell, M.D. (1993). Wind measurement and archival under the Automated Surface Observing System (ASOS): User concerns and opportunity for improvement. *Bulletin of the American*

Meteorological Society, 74, 615-624

Pye, K. (2015). *Aeolian dust and dust deposits*. Elsevier

Ramcharan, A., Hengl, T., Nauman, T., Brungard, C., Waltman, S., Wills, S., & Thompson, J. (2018). Soil property and class maps of the conterminous United States at 100-meter spatial resolution. *Soil Science Society of America Journal, 82*, 186-201

Ravi, S., D'Odorico, P., Breshears, D.D., Field, J.P., Goudie, A.S., Huxman, T.E., Li, J.R., Okin, G.S., Swap, R.J., Thomas, A.D., Van Pelt, S., Whicker, J.J., & Zobeck, T.M. (2011). Aeolian Processes and the Biosphere. *Reviews of Geophysics, 49*

Reynolds, R.L., Yount, J.C., Reheis, M., Goldstein, H., Chavez, P., Fulton, R., Whitney, J., Fuller, C., & Forester, R.M. (2007). Dust emission from wet and dry playas in the Mojave Desert, USA. *Earth Surface Processes and Landforms, 32*, 1811-1827

Rivera, N.I.R., Gill, T.E., Bleiweiss, M.P., & Hand, J.L. (2010). Source characteristics of hazardous Chihuahuan Desert dust outbreaks. *Atmospheric Environment, 44*, 2457-2468

Rudich, Y., Khersonsky, O., & Rosenfeld, D. (2002). Treating clouds with a grain of salt. *Geophysical Research Letters, 29*, 17-11-17-14

Sayer, A., Hsu, N., Bettenhausen, C., & Jeong, M.J. (2013). Validation and uncertainty estimates for MODIS Collection 6 "Deep Blue" aerosol data. *Journal of Geophysical Research: Atmospheres, 118*, 7864-7872

Sayer, A., Munchak, L., Hsu, N., Levy, R., Bettenhausen, C., & Jeong, M.J. (2014). MODIS Collection 6 aerosol products: Comparison between Aqua's e-Deep Blue, Dark Target, and "merged" data sets, and usage recommendations. *Journal of Geophysical Research: Atmospheres, 119*, 13,965-913,989

Shao, Y. (2000). *Physics and Modelling of Wind Erosion*. Springer Netherlands

Shao, Y., & Raupach, M.R. (1993). Effect of Saltation Bombardment on the Entrainment of Dust by Wind. *Journal of Geophysical Research-Atmospheres, 98*, 12719-12726

Shao, Y.P., Wyrwoll, K.H., Chappell, A., Huang, J.P., Lin, Z.H., McTainsh, G.H., Mikami, M., Tanaka, T.Y., Wang, X.L., & Yoon, S. (2011). Dust cycle: An emerging core theme in Earth system science. *Aeolian Research, 2*, 181-204

Tegen, I., Harrison, S.P., Kohfeld, K., Prentice, I.C., Coe, M., & Heimann, M. (2002). Impact of vegetation and preferential source areas on global dust aerosol: Results from a model study. *Journal of Geophysical Research-Atmospheres, 107*, 9567

Thomson, M.C., Molesworth, A.M., Djingarey, M.H., Yameogo, K.R., Belanger, F., & Cuevas, L.E. (2006). Potential of environmental models to predict meningitis epidemics in Africa. *Tropical Medicine & International Health, 11*, 781-788

Twomey, S.A., Piepgrass, M., & Wolfe, T.L. (1984). An Assessment of the Impact of Pollution on Global Cloud Albedo. *Tellus Series B-Chemical and Physical Meteorology, 36*, 356-366

Vest, K.R., Elmore, A.J., Kaste, J.M., Okin, G.S., & Li, J.R. (2013). Estimating total horizontal aeolian flux within shrub-invaded groundwater-dependent meadows using empirical and mechanistic models. *Journal of Geophysical Research-Earth Surface, 118*, 1132-1146

Webb, N.P., Okin, G.S., & Brown, S. (2014). The effect of roughness elements on wind erosion: The importance of surface shear stress distribution. *Journal of Geophysical Research-Atmospheres, 119*, 6066-6084

Westerling, A.L., Gershunov, A., Brown, T.J., Cayan, D.R., & Dettinger, M.D. (2003). Climate and wildfire in the western United States. *Bulletin of the American Meteorological Society, 84*, 595-604